

POLITECNICO DI TORINO

Department of Mechanical and Aerospace Engineering

Master Degree Course in Aerospace Engineering

Master's Degree Thesis



Thermochemical Models for Hypersonic Regime

Numerical simulation of plasma formation for high-speed
and high temperature reacting flows

Supervisor
prof. Domenic D'Ambrosio

Candidate
Carlo Brunelli s275587

Academic Year 2020-2021

Summary

In the last decades, human's ability to penetrate further into space and accomplish more complex missions has improved dramatically. In parallel, increasingly sophisticated and faster weapons, such as hypersonic missiles, have been developed. For these reasons, also the need to study the phenomena that occur while travelling at very high speeds has arisen in both the civil and military sectors. Hypersonic flows are significantly more challenging to simulate than conventional subsonic or supersonic flows, due to additional complex physical processes such as shocks, chemical reactions and plasma formation. Consequently, it is not possible to adopt the same numerical models and methods commonly used to predict the property and behaviour of low-speed flow, because they are incomplete and can not manage properly all the complexities that occur in hypersonic flow. First of all, a MATLAB code has been developed. It contains thermochemical atmospheres models of the Earth, Mars and Jupiter. Each model takes into account different chemical species and reactions. Therefore, the re-entry or landing of a capsule or any other spacecraft can be simulated in different scenarios. The software can calculate the equilibrium composition of a mixture and the thermochemical relaxation downstream a normal shock wave. The results obtained have been compared with data available in literature and the code has been validated. In second instance, the thermochemistry has been studied and implemented in a commercial code, specifically, STAR-CCM+ by Siemens. One-dimensional CFD simulations have been carried out in order to study equilibrium conditions. Every analysis has been carried out by adopting a suitable physical model, numeric discretization scheme and fine enough grids to avoid numerical instabilities and to guarantee accurate results. The results of CFD analysis and MATLAB code are in line with each other, only slight differences have been detected. The results produced by the MATLAB code have been compared with those found in the literature. The chemical and energy transient calculations have been validated.

Contents

List of Tables	VI
List of Figures	VII
1 Introduction	1
1.1 Overview	1
1.2 Hypersonic Flow Regime	2
1.2.1 Hypersonic Flow Characteristics	2
1.2.2 Shock: shape and features	3
1.2.3 A time-dependent approach	6
2 Physical Model	7
2.1 Intro	7
2.1.1 High-Temperature Gas	7
2.2 Classification of Gases	8
2.2.1 Calorically Perfect Gas	8
2.2.2 Thermally Perfect Gas	8
2.2.3 Chemically Reacting Mixture of Perfect Gases	9
2.2.4 Real Gas	9
2.3 Species Mixture Models	10
2.4 Equilibrium, non-equilibrium and frozen flow	11
2.5 Equilibrium	13
2.5.1 Compute equilibrium composition	13
2.6 Internal Energy	16
2.6.1 Heat of Reaction and Formation	19
2.7 Non-Equilibrium	20
2.7.1 Vibrational Non-equilibrium	20
2.7.2 Chemical Non-Equilibrium	21
2.8 Governing Equation	22
2.8.1 Non reacting gas	22
2.8.2 Reacting Non-Equilibrium Gas	23
2.8.3 Mass balance	23

2.8.4	Momentum	25
2.8.5	Energy	26
2.9	Boundary conditions	26
2.9.1	Velocity	26
2.9.2	Temperature	27
2.9.3	Concentrations	27
3	MATLAB Code	28
3.1	Introduction	28
3.2	Code Main Files	28
3.2.1	Thermochemical Model	29
3.3	Compute Equilibrium Condition	30
3.4	Thermochemical Relax	31
3.5	Code Validation	32
3.5.1	Mach 1.5, test case 1	32
3.5.2	Thermodynamic Properties Ratio, test case 2	35
3.5.3	Influence of pressure, test case 3	35
3.5.4	Relaxation and equilibrium, test case 4	36
3.5.5	Validation through CEARUN, test case 5	38
4	One-dimensional Analysis	40
4.1	CFD set up	40
4.1.1	Mesh	40
4.1.2	Physical model	41
4.1.3	Chemical Species and Reactions	42
4.1.4	Boundary, Initials conditions	42
4.2	Test cases and results	42
4.2.1	The procedure	42
4.2.2	<i>O2</i> dissociation	43
4.2.3	<i>N2</i> dissociation	46
4.2.4	<i>NO</i> dissociation	47
4.2.5	<i>O</i> ionization	48
4.2.6	Complete model: 30 reactions and 10 species	50
4.3	Comments and considerations	51
4.4	Gibbs Free Energy	52
4.5	Park and Gibbs Free Energy comparison	52
4.5.1	Low Temperature	58
4.5.2	<i>NO</i> ionization	58
5	Two Temperatures Model	59
5.1	Introduction	59
5.2	Two Temperature model and time relaxation	59
5.3	Test Cases	61

5.3.1	N2 Bath	62
5.3.2	5 species air model	62
5.4	STAR-CCM+ two temperature model	62
5.4.1	N ₂ Bath STAR-CCM+ results	63
5.4.2	N ₂ Bath STAR-CCM+ time step influence	64
5.5	Multiple vibration temperatures model	67
5.5.1	N ₂ Bath results	68
5.5.2	5 species air multiple vibration temperatures results	69
5.6	Single vibration temperature model	69
5.6.1	How to compute a single vibrational temperature	69
5.6.2	5 species air \hat{T}^v post-processing	71
5.6.3	Approximations in the thermochemical model	72
5.7	Conclusion and considerations	73
6	Non-Equilibrium in STAR-CCM+	75
6.1	Introduction	75
6.2	STAR-CCM+ Models	75
6.2.1	Specific Heat	75
6.2.2	Reaction Coefficient	76
6.2.3	Mode Relaxation Time	76
6.3	N2 Bath Inviscid	77
6.3.1	STAR-CCM+ models comparison	78
6.3.2	STAR-CCM+ and MATLAB code relaxation comparison	79
6.4	RAM-C II	80
6.4.1	Mach and electron density	81
6.4.2	Electron number density	82
6.4.3	Mass Fraction along stagnation line	83
6.5	HEG Cylinder	84
6.5.1	Ideal Gas	85
6.5.2	Thermal Non-Equilibrium	86
6.6	Comments and considerations	88
7	Conclusion and Further Development	91
A	Thermodynamic Properties	93
A.1	Chemical reactions data	93
A.2	Thermodynamic data	95
B	Gibbs Free Energy	97
B.1	Gibbs Free Energy and Concentrations Equilibrium Constant	97

C Solver Settings	101
C.1 Finite Volume Discretization	101
C.1.1 MUSCL 3rd-order scheme	102
C.1.2 Diffusive Flux	104
C.2 Discretization: AUSM+	104
C.3 Courant-Friedrichs-Lewy (CFL) number	104
C.4 Algebraic Multigrid Method	105
C.4.1 AMG solver	107
C.4.2 Acceleration methods	108
Bibliography	109

List of Tables

2.1	Formation matrix 5 species model	10
3.1	Test Case 2 $u_1 = 36\,000\text{m/s}$, $h = 170\,000\text{ft}$	35
3.2	Comparison between the results of equilibrium post-shock 7 or 10 species model in Test Case 2	35
3.3	Equilibrium Post Shock - 10 species model	36
3.4	Chemical Equilibrium CEARUN vs MATLAB code	38
3.5	Chemical species in CEARUN vs MATLAB code	39
4.1	Mass fractions of the species in the mixture at the equilibrium. $T_{eq} = 3374\text{ K}$ $p_{eq} = 62016\text{ Pa}$, atmospheric freestream composition $y(O_2) = 0.23$, $y(N_2) = 0.77$	50
5.1	N_2 bath initial conditions	62
5.2	5 species air model bath initial conditions	62
5.3	Vibrational temperatures maximum values comparison, N_2 bath	69
6.1	N_2 bath initial conditions STAR-CCM+	77
6.2	RAM-C freestream conditions	80
6.3	HEG freestream conditions	85
A.1	Coefficients NASA polynomials	96

List of Figures

1.1	Schematic of the flowfield over a blunt body moving at supersonic or hypersonic speeds, [2]	4
1.2	Shock features	5
1.3	$\beta - \theta - M$ diagram	5
2.1	Variation of γ as a function of temperature [2]	8
2.2	Temperature Effects on Air [2]	12
2.3	$K_{cO_2,diss}(T)$	15
2.4	Modes of molecular energy [2]	16
2.5	Schematic of energy levels for the different molecular energy modes [2]	18
3.1	Establishing independent processes	30
3.2	Influence of pressure on the normal shock temperature in equilibrium air, [2]	36
3.3	Temperature relaxation-10 species model	37
3.4	e^- mass frac relaxation-10 species model	37
4.1	Geometry and Mesh 1D analysis	41
4.2	Equilibrium Constant of O_2 dissociation comparison	44
4.3	Equilibrium Temperature O_2 dissociation	45
4.4	Equilibrium Constant of N_2 dissociation comparison	47
4.5	Equilibrium Temperature N_2 dissociation	47
4.6	NO dissociation equilibrium constant and temperature	48
4.7	O ionization equilibrium constant and temperature	49
4.8	K_c NO dissociation, difference between 1000 and 10000 iterations	51
4.24	NO^+ ionization detailed comparison between Park and Gibbs method	57
5.1	5×5 mesh	63
5.2	N_2 bath results, STAR-CCM+ simulation, $\Delta t = 10^{-11}s$	64
5.3	N_2 bath results, STAR-CCM+ simulation, $\Delta t = 10^{-10}s$	65
5.4	N_2 bath results, STAR-CCM+ simulation, $\Delta t = 10^{-9}s$	65
5.5	N_2 bath results, STAR-CCM+ simulation, $\Delta t = 10^{-8}s$	66
5.6	N_2 bath results, STAR-CCM+ simulation, $\Delta t = 10^{-5}s$	67
5.7	N_2 results and comparison with [14]	68
5.8	5 species air relaxation results, multiple vibration temperatures	70
5.9	Compute \hat{T}^v as post-process	71

5.10	5 species air relaxation results, \hat{T}^v as post-process	72
5.11	Compute \hat{T}^v and use it to compute T_r	72
5.12	5 species air relaxation results, Single vibration temperature model	73
6.1	Comparison of Landau-Teller and Millikan-White-Park relaxation time correlation	78
6.2	Comparison of STAR-CCM+ and the MATLAB code relaxation of N2 Bath, temperatures	79
6.3	Comparison of STAR-CCM+ and the MATLAB code relaxation of N2 Bath, mass fraction	80
6.4	Mesh detail close to the nose	81
6.5	Mach number, RAM-C case, comparison with numeric results [14]	81
6.6	Electron density, RAM-C case, comparison with numeric results [14]	82
6.7	Electron number density, RAM-C	83
6.8	RAM-C species concentrations. Comparison with numerical [14]	84
6.9	Pressure distribution, ideal gas, HEG case. Comparison with numerical and experimental results [14]	85
6.10	Heat Flux, ideal gas, HEG case. Comparison with numerical and experimental results [14]	86
6.11	Rotational-temperature, Thermal Non-Equilibrium gas, comparison with Maier et al. results, HEG case	87
6.12	Vibrational temperature, Thermal Non-Equilibrium gas, comparison with Maier et al. results, HEG case	87
6.13	Heat Flux, HEG case. Comparison with numerical and experimental results [14]	88
6.14	Mass fraction of the chemical species, Thermal Non-Equilibrium gas, HEG case	90
A.1	CHEMKIN file, information about reactions	94
C.1	Example of a 2D finite volume discretization	101
C.2	NVD diagram	103
C.3	Carbuncle phenomenon on different solver, [23]	105
C.4	Cycle strategies available in STAR CCM+	107

Symbols

Thermodynamic

c_p	Specific heat capacity for a constant pressure [$J kg^{-1}$]
c_v	Specific heat capacity for a constant volume [$J kg^{-1}$]
Da	Damkohler number
E	Internal Energy [$J Mol^{-1}$]
e	Internal Energy [$J kg^{-1}$]
G	Gibbs free energy [$J Mol^{-1}$]
γ	Heat capacity ratio
\mathcal{M}	Molecular mass of the gas [$kg Mol^{-1}$]
H	Enthalpy [$J Mol^{-1}$]
h	Enthalpy [$J kg^{-1}$]
K_c	Concentrations equilibrium constant
K_p	Pressure equilibrium constant
\mathcal{N}	Number of particles
N	Number of moles [Mol]
N_A	Avogadro constant [$6.022 \cdot 10^{26} Mol^{-1}$]
N_{spe}	Number of chemical species
ν_{is}	Stoichiometric number for species is , $\nu_{is} > 0$ for products and $\nu_{is} < 0$ for reactants

$\Delta\nu_{is}$	Stoichiometric number variation
m	Mass [kg]
p	Pressure [Pa]
Q	Heat [$J kg^{-1}$]
q	Mol mass Ratio [$Mol kg^{-1}$]
R	Specific gas constant of a gas or a mixture of gases [$J kg^{-1} K^{-1}$]
\mathcal{R}	Universal gas constant [$8314 J Mol^{-1} K^{-1}$]
ρ	Density [$kg m^{-3}$]
S	Entropy [$J Mol^{-1} K^{-1}$]
s	Entropy [$J kg^{-1} K^{-1}$]
T	Temperature (translational-rotational)[K]
T_v	Vibrational Temperature (translational-rotational)[K]
τ_c	Chemical reactions characteristic time [s]
τ_f	Fluid characteristic time [s]
v	Volume per unit of mass [$m^3 kg^{-1}$]
v	Vibrational level
\mathcal{V}	Volume [m^3]
x_{is}	Molar fraction of $is - th$ species
y_{is}	Mass fraction of $is - th$ species

Energy

ε'	Absolute Internal energy [$J Mol^{-1}$]
ε	Sensible energy [$J Mol^{-1}$]
ε'_0	zero-point energy [$J Mol^{-1}$]
ε'_t	Translational energy [$J Mol^{-1}$]

ε'_r	Rotational energy [$J Mol^{-1}$]
ε'_v	Vibrational energy [$J Mol^{-1}$]
ε'_e	Electronic energy [$J Mol^{-1}$]
L	Degrees of freedom
θ	Characteristic temperature of vibration [K]
k_B	Boltzmann constant [$1.38 \cdot 10^{-23} J K^{-1}$]
h	Plank constant [$6.62 \cdot 10^{-34} J s$]
ΔH_f^0	Heat of formation at $0K$ [$J kg^{-1}$]
τ_i^{V-T}	Relaxation time [s]
$[X]$	Molar concentration of species X [$Mol m^{-3}$]
k_b	Bacward reaction rate [$Mol m^{-3} s^{-1}$]
k_f	Forward reaction rate [$Mol m^{-3} s^{-1}$]
ϵ_a	Energy activation [$J Mol^{-1}$]

Dynamic and Viscosity

\mathbf{v}	Velocity [$m s^{-1}$]
$\dot{\mathbf{q}}$	Heat flux [W]
Ω_i^{ch}	Local rate of change of $i - th$ species due to ch reaction [$kg m^{-3} s^{-1}$]
\mathbf{w}	Diffusive velocity [$m s^{-1}$]
k	Thermal conductivity coefficient [$W m^{-1} K^{-1}$]
J_{mi}	Species mass diffusive flux [$kg m^{-3} s^{-1}$]
\mathcal{D}_{im}	Multi-component diffusion coefficient
\mathcal{D}_{ij}	Diffusion coefficient of $i - th$ species into $j - th$
μ	Dynamic viscosity [$Pa s$]

Subscripts

<i>eq</i>	Equilibrium
<i>ie</i>	Index element
<i>ele</i> or <i>e</i>	element
<i>is</i>	Index species
<i>spe</i> or <i>s</i>	species
<i>ir</i>	Index reaction
<i>rea</i> or <i>r</i>	reaction
∞	Freestream Conditions
<i>neq</i>	Non equilibrium

Chapter 1

Introduction

1.1 Overview

Hypersonic flow is generally characterised by a free stream flow with a Mach number greater than 5. The hypersonic regime can be more appropriately defined as the flow field where several physical phenomena, that are negligible at lower speeds, must be taken into account. There are some characteristic events that occur in a flow field with a high Mach number, including thin shock layers, viscous interactions and hot chemically reacting gases. The temperature, pressure and density of the flow suddenly increase across the shock wave which surrounds a body at supersonic speed. In addition, also the gas properties are profoundly different in hypersonic regime because they reach extremely high temperatures, especially behind shock waves. As a consequence of high temperatures, chemical reactions such as dissociations and ionizations occur. Furthermore, this leads to the formation of new chemical species. As the upstream speed reaches higher values, these phenomena gain more and more importance and the shock wave draws near to the surface of the body. Hypersonic flows are significantly more challenging to simulate than conventional subsonic or supersonic flows due to these additional complex physical processes. Consequently, it is not possible to adopt the same numerical models and methods commonly used to predict property and behaviour of low-speed flow, because they are incomplete and can not manage properly all the complexities that occur in hypersonic flow.

The presence of charged particles and consequently the formation of plasma is a subject of particular interest. In the civil sector, during the re-entry of a capsule into the atmosphere, the presence of plasma, created by the heat from the compression of the atmosphere by the craft, causes a total lack of radio communications capability. This phenomenon is the communications blackout. It is caused by an envelope of ionized air around the craft that interferes with radio signals. The need to study plasma is found also in the defence sector. During the flight of a hypersonic missile, charged particles are formed. These can be detected by special radars that can track

the missiles.

The primary aim, when a body is travelling at hypersonic speed in the atmosphere, is to study the changes in gas composition and its properties. A MATLAB code with a proper thermochemistry model has been developed. Afterwards, several CFD analysis using the commercial code STAR-CCM+ have been carried out. The results of these two methods are compared to verify the precision of both methods. In this way, a simple but reliable MATLAB calculation code is available for the study of thermo-chemical equilibrium and relaxation.

1.2 Hypersonic Flow Regime

This section presents the main characteristics and development of a hypersonic stream encountering a body. It is the link between two different points of view. The first aspect is the physics of the gas and its local behaviour which is described by the governing equations in 2.8. The equations have been implemented and solved in a self-developed code in MATLAB. The second point is the macroscopic flow field surrounding for example a re-entry vehicle.

1.2.1 Hypersonic Flow Characteristics

The flow regime is strongly influenced by the Mach number of the flow:

- $M < 1$: subsonic flow
- $0.8 \leq M \leq 1.2$ transonic
- $M > 1$ supersonic

As a general rule, for $M > 5$ the regime is called hypersonic because it has certain unique characteristics.

The region between shock and the body is called the shock layer. For the same flow deflection angle, the shock angle decreases as the speed increases. The thickness of the shock layer decreases with an increase in Mach number, so the shock wave is closer to the body. Therefore, hypersonic flows have a thin shock layer.

One of the main properties of the curved shock waves is that each streamline passing through the shock has a different entropy increase which is higher in the stronger portion of a shock than in the weaker portion. Therefore, a layer of the entropy variation is formed downstream of the shock is called *entropy layer*.

Analysis of hypersonic flow becomes more challenging, in fact, according to Croco's theorem the entropy layer leads to vorticity:

$$T\nabla s = \frac{\partial \mathbf{v}}{\partial t} - \nabla h_0 - \mathbf{v} \times (\nabla \times \mathbf{v}) \quad (1.2.1)$$

where s is entropy, \mathbf{v} the velocity, h_0 the enthalpy that remains constant through the shock and $\mathbf{w} = \nabla \times \mathbf{v}$ is the fluid vorticity. The shock detachment distance decreases with an increase in Mach number for blunt bodies, so the entropy layer exhibits a strong gradient of entropy which leads to higher vorticity at higher values of Mach numbers. The entropy layer creates vorticity that interacts with the boundary layer and this makes simulating hypersonic flow even more complex.

The formation of the boundary layer occurs in the proximity of the wall due to the no-slip property of the viscous fluid. The formation of boundary layer at hypersonic speeds involves a significant loss of kinetic energy and it is necessarily converted into thermal energy. Thus, there is an increase in the flow temperature in the proximity of the wall. This phenomenon is viscous dissipation and it also increases boundary layer thickness due to a growth in viscosity coefficient with temperature. From boundary layer theory where pressure is considered to be constant across the boundary layer, $\frac{\partial p}{\partial y} = 0$. The density necessarily decreases due to the increment of temperature and so the boundary layer thickens to ensure the passage of the same fluid flow rate.

1.2.2 Shock: shape and features

The aerodynamic characteristics of an aircraft are strictly associated with its flight speed range and mission requirements. For a supersonic transport vehicle, e. g. SR-71 Blackbird, the leading edge is sharpened due to reducing the wave drag caused by the shock that occurs at supersonic speed. On the opposite side, a re-entry capsule has a blunt shape by reason of maximising the drag using the atmosphere to brake and this shape is also useful to minimise the thermal heat flux.

The flowfield surrounding a re-entry vehicle is quite complex, as it presents both subsonic and supersonic regions.

A strong detached bow shock takes place in front of a blunt body when the freestream is supersonic, as shown in 1.1. A shock wave is essentially a viscous layer of small thickness but in computational fluid dynamics it can be considered as a flow discontinuity even in an inviscid flow field. Thus, there is a motion field with constant thermodynamic properties upstream of this discontinuity. Downstream there is a complex field, the study of which is the subject of this research. It is also a zone of accentuated vorticity due to the gradients of velocity in the normal direction. The first logical step is to perform an analysis of the characteristic of the flow over a blunt body as to obtain data concerning pressure and temperature distributions over the body surface. The bow shock wave properties are influenced by the freestream thermodynamic conditions as well as the shape of the body. In particular, the shape and the detachment distance δ are unknown but for a blunt body with an elementary form (sphere-cone and circular cylinder-wedge bodies) they can be approximately determined using the Billig correlations which are based

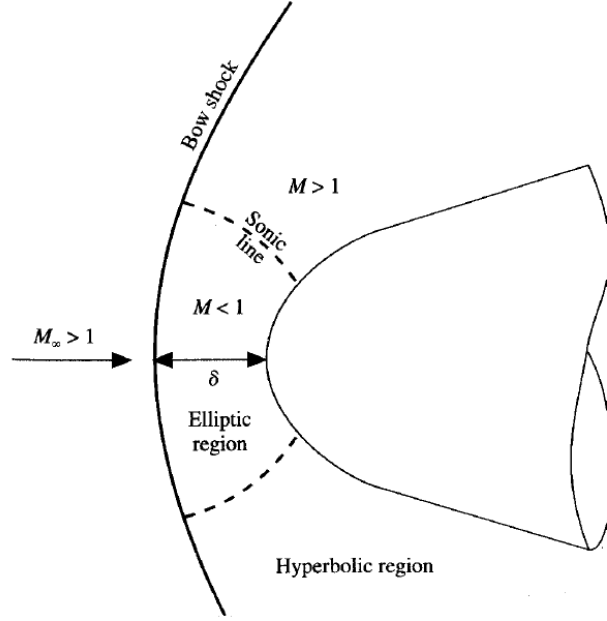


Figure 1.1: Schematic of the flowfield over a blunt body moving at supersonic or hypersonic speeds, [2]

on experimental data:

$$x = R + \delta - R_c \cot^2 \beta \left[\left(1 + \frac{y^2 \tan^2 \beta}{R_c^2} \right)^{1/2} - 1 \right] \quad (1.2.2)$$

$$\frac{\delta}{R} = \begin{cases} 0.143 \exp [3.24/M_\infty^2] & \text{sphere-cone} \\ 0.386 \exp [4.67/M_\infty^2] & \text{cylinder-wedge} \end{cases} \quad (1.2.3)$$

Where R is the radius of the nose, R_c is the radius of curvature of the shock wave at the vertex of the hyperbola and δ is the shock detachment distance, as shown in 1.2. x and y are the coordinates, and β is the angle of the shock at an infinite distance away from the nose. The value of β is influenced by the upstream speed and blunt body geometry. If the body is a cone of angle θ_c , β is the angle for an attached shock wave on a sharp cone of angle θ_c . If the body is axisymmetric and the body is a cylinder aligned with the flow then β is a Mach wave.

The shock in the proximity of the symmetry axis of the body is strong and it can be modeled as a normal shock wave. As the shock weakens and it bends moving away from the axis. This behaviour can also be studied on the 1.3 $\beta - \theta - M$. Here on the x-axis, δ is the deflection of the streamline and on the y-axis β represents the deflection of the shock wave. Each line is drawn for a different Mach number. In the diagram for $\theta = 0^\circ$ two different solution are possible:

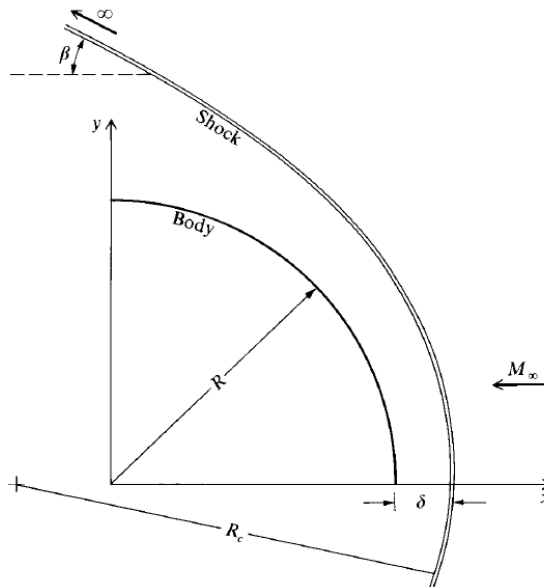


Figure 1.2: Shock features

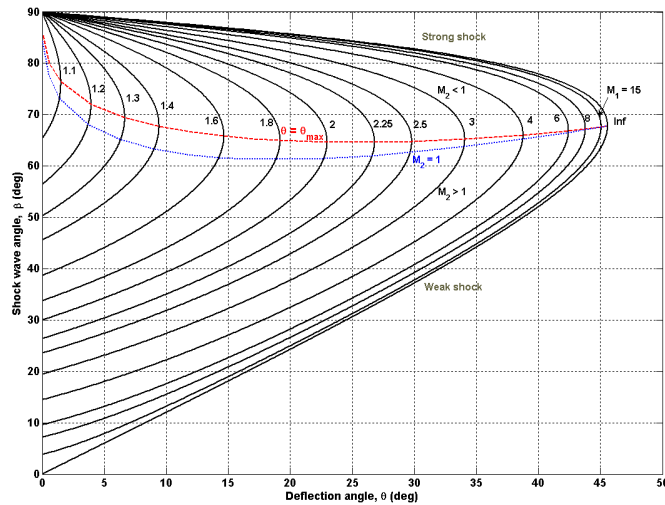


Figure 1.3: $\beta - \theta - M$ diagram

- normal shock. It is known, e.g. from the Rankine-Hugoniot relations, that after a normal shock the flow is subsonic, the speed is drastically reduced and it is highly compressed. Therefore, the flow in the region close to the nose behind the shock is locally subsonic, and it is governed by elliptic partial differential equations. The differential equation to compute the post-shock

conditions in differential forms are:

$$\begin{cases} d(\rho u) = 0 \\ d(p + \rho u^2) = 0 \\ d(h + \frac{u^2}{2}) = 0 \end{cases} \quad (1.2.4)$$

- vanishing shock. The shock is so weak that there are no measurable variations in the fluid property. The flow far from the nose is supersonic, and it is governed by hyperbolic partial differential equations.

The imaginary line between the subsonic and supersonic regions is called the sonic line.

1.2.3 A time-dependent approach

The change in the mathematical nature of the equations from elliptic in the subsonic region to hyperbolic in the supersonic region was the cause of difficulties in finding a method of resolution. Different techniques were developed for just the subsonic portion, and others (e. g. method of characteristics) were developed for the supersonic region. The main difficulty was finding a way to solve the mixed subsonic-supersonic flowfield. Fortunately, a breakthrough occurred in the blunt-body problem thanks to Moretti and Abbett [20]. They developed a numerical finite-difference solution to the supersonic blunt-body problem taking advantage of the power of Computational Fluid Dynamics (CFD). In particular, they developed and implemented the concept of a *time-dependent* approach to the steady-state, causing also the equations of the subsonic region to be hyperbolic.

Chapter 2

Physical Model

2.1 Intro

The ambition of the present section is to provide the fundamental laws that describe flow fields, with a focus on the peculiar thermochemical aspects of the hypersonic regime. Notably, the effects of high temperatures on gas properties are discussed, with an emphasis on the difference between supersonic and subsonic streams. In addition, different physical and chemical models are presented to get to choose the most suitable for each specific case in the analysis. The discussion starts with the introduction of issues concerning high temperature gases. Then, the chemical point of view is presented and models and methods for computing gas composition are discussed. Lastly, the purely fluid-dynamic governing equations are presented and how they change when high temperature conditions are taken into account.

2.1.1 High-Temperature Gas

It is important to study the effect of high temperature in flows. The high temperature is usually reached when the free stream flow is hypersonic, for example for capsules that re-entering from orbit or interplanetary missions. In fact, in presence a of very high speed linked to a very high temperature some of the hypothesis that are the foundations of the supersonic aerodynamics fall. First of all, γ and the specific heats are not constant anymore. Indeed, molecules begin to dissociate and even ionize, the gas become chemically reacting. Concerning atmospheric air when it reaches the temperature of 800K, the vibrational motion of the molecules is important and it absorbs a portion of energy, so the model of classic thermodynamics is no longer suitable.

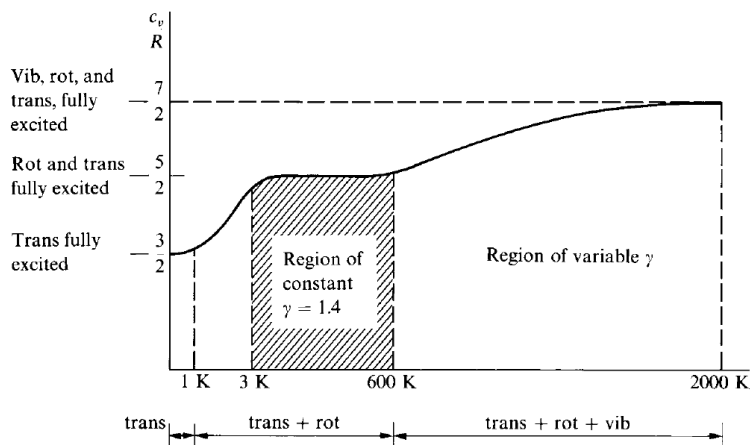


Figure 2.1: Variation of γ as a function of temperature [2]

2.2 Classification of Gases

It is possible to identify four different categories of gas as reported in [2]. It is necessary to remember the difference between a perfect and real gas, in the former intermolecular forces can be neglected while they must be taken into account in the latter.

2.2.1 Calorically Perfect Gas

A calorically perfect gas is one with constant specific heats c_p and c_v , as a consequence also $\gamma = \frac{c_p}{c_v}$ is constant. The perfect-gas equation can be used

$$pv = RT \quad (2.2.1)$$

where R is constant it depends on the gas.

$$R = \frac{\mathcal{R}}{\mathcal{M}}$$

where \mathcal{R} is the universal gas constant and \mathcal{M} is the molecular mass of the gas.

2.2.2 Thermally Perfect Gas

A thermally perfect gas is one where c_p and c_v are functions of the temperature only.

$$c_p = c_p(T)$$

$$c_v = c_v(T)$$

In this model h and e are still function of the temperature only.

$$dh = c_p(T)dT$$

$$de = c_v(T)dT$$

The perfect-gas equation can be used $pv = RT$ where R is constant and it depends on the gas.

2.2.3 Chemically Reacting Mixture of Perfect Gases

In this model, the gas intermolecular forces are neglected and the gas is considered as a mixture of thermally perfect gases. This is the proper way for modelling gas in a supersonic regime. At high speed, behind a shock wave, due to the high temperature chemical reactions happen and there is the formation of new chemical species. The molecules dissociate and ionize. Consequently, air changes its composition, it is no longer composed by N_2 and O_2 only, but other species such as O , N , NO (in a 5 model species) are now present. Each individual species follows the perfect-gas equation:

$$p_{is}v = R_{is}T$$

$$R_{is} = \frac{\mathcal{R}}{\mathcal{M}_{is}}$$

where \mathcal{R} is the universal gas constant and \mathcal{M}_{is} is the molecular mass of the is -th species.

2.2.4 Real Gas

A real gas is one where intermolecular forces can not be neglected. A gas behaves like a real gas when the temperature is low and the pressure is very high. Under these conditions, a gas is rarely chemically reacting. The specific heats c_p and c_v are not constant anymore, they are determined by the thermodynamic state of the system (uniquely identified by two variables of state):

$$c_p = c_p(T, p)$$

$$c_v = c_v(T, p)$$

The perfect-gas equation can not be used, it must be correct so that one can take into account the intermolecular forces.

2.3 Species Mixture Models

It is necessary to define a species mixture model to describe the composition of the gas after the bow shock. As previously introduced, new species form due to the high temperatures. It is possible to define different models that consider different species and for each case under analysis, the most suitable must be chosen. Among all air models Ar , CO_2 , H_2O are not included because they are present in negligible quantities.

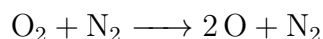
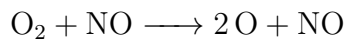
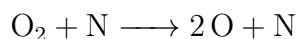
- 5 species model: N_2 , O_2 , NO , N , O

Ele/Spe	N_2	O_2	NO	N	O
N	2	0	1	1	0
0.36, 0.54, 0.66 O	0	2	1	0	1

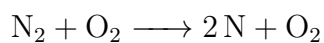
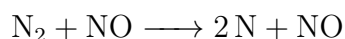
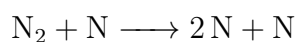
Table 2.1: Formation matrix 5 species model

In this model 17 different reactions are taken into account:

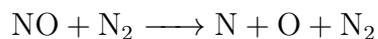
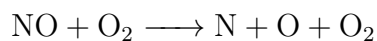
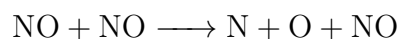
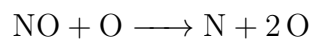
Dissociation of oxygen



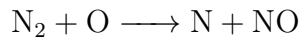
Dissociation of nitrogen



Dissociation of nitric oxide



Exchange



- 7 species model: N_2 , O_2 , NO , N , O , NO^+ , e^- . More information such as reactions, value of equilibrium constant and Arrhenius coefficient about this model can be found at appendix A.
- 11 species model: N_2 , O_2 , NO , N , O , NO^+ , e^- , N_2^+ , O_2^+ , N^+ , O^+ . More information such as reactions, value of equilibrium constant and Arrhenius coefficient about this model can be found at appendix A.
- 11+ species model: more sophisticated models can be adopted. For example in the case the thermal protection shield of the re-entry capsule is ablative. It means that it is slowly consumed by the hot gas and so molecules of new elements, such as carbon, are now present in the flow and they can react creating new species.
- non-Earth species model: specific models can be adopted for simulating the atmospheric entrance of a capsule in an extraterrestrial planet like Mars and Jupiter. The atmosphere composition and thermochemical properties (like temperatures and density) are different from those on Earth.

The air at sea level is essentially a calorically perfect gas. A gas can not be modelled as calorically perfect when the temperature reaches approximately $800K$. The degrees of freedom of the molecules increase, they are not only rotational and translational anymore. The vibrational and electronic degrees of freedom are activated due to the high energy, and are negligible at low temperatures. Above $2500K$ chemical reactions begin and the air becomes a chemically reacting mixture of perfect gases. In particular, at $2500K$ O_2 begins to dissociate while N_2 starts at $4000K$. Finally, beyond $9000K$ ionization occurs and the initial air with atmospheric composition becomes plasma. At this level there are free electrons (e^-) and ions (NO^+ , O^+ , N^+ , O_2^+ , N_2^+). However, plasma is mainly formed by O^+ , N^+ , O , N and electrons.

2.4 Equilibrium, non-equilibrium and frozen flow

From the chemical point of view, a flow can be categorized into three different states: equilibrium, non-equilibrium and frozen. A specific parameter can be introduced to better comprehend the difference between these states. It is the Damkohler number defined as:

$$Da = \frac{\tau_f}{\tau_c} \quad (2.4.1)$$

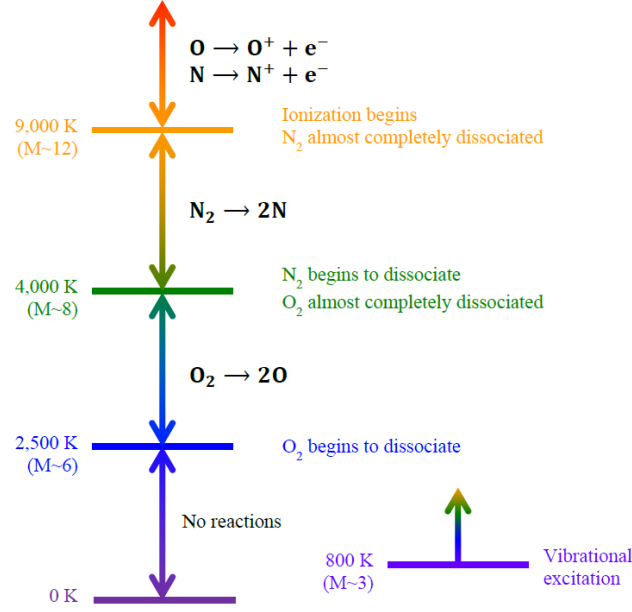


Figure 2.2: Temperature Effects on Air [2]

where τ_f is the characteristic time for the fluid element to cross the flow field in analysis. It is typically computed as L/V , where L is the characteristic dimension of the flow field and V the mean velocity of the fluid element. τ_c is the characteristic time for the chemical reaction to occur. Also, it can be considered as the time needed for internal energy to reach equilibrium.

$Da \rightarrow \infty, \tau_f \gg \tau_c$: the fluid element is moving slowly through the flow field compared to the speed of the reactions that happen almost instantly. At each point, the fluid element has sufficient time to reach the composition of equilibrium.

$Da \approx 1, \tau_f \approx \tau_c$: the reaction and fluid element have a similar velocity. At each point, the fluid element has not sufficient time to reach the composition of equilibrium, this is the non-equilibrium case.

$Da \approx 0, \tau_f \ll \tau_c$: the chemical reactions are so slow compared with the speed of the fluid element. In this case, the composition of the fluid element does not change through the field even if it is far away from the equilibrium condition, this is the frozen case.

2.5 Equilibrium

The chemical equilibrium condition occurs when the amount of collisions between the molecules per unit of time is so high that the time required by a reaction to occur is infinitesimal: the reactions happen almost instantly. The mixture composition is a unique function of p and T or any other pair of thermodynamics variables. The state of the system is uniquely defined by any two state variables. Species concentrations are not time-independent, they are only influenced by the composition of the free stream gas and by the thermodynamic state.

$$y_i = y_i(T, p) \quad (2.5.1)$$

where y_i is the mole fraction of i -th species. As it has been previously discussed, the concentrations of the different species deeply influence the characteristics of the fluid.

$$h = h(T, y_1, \dots, y_{N_{spe}})$$

$$e = e(T, y_1, \dots, y_{N_{spe}})$$

$$c_p = c_p(T, y_1, \dots, y_{N_{spe}})$$

$$c_v = c_v(T, y_1, \dots, y_{N_{spe}})$$

Because of the (2.5.1) in case of equilibrium the properties are no longer directly influenced by the composition:

$$h = h(T, p)$$

$$e = e(T, p)$$

$$c_p = c_p(T, p)$$

$$c_v = c_v(T, p)$$

2.5.1 Compute equilibrium composition

It is possible to compute the equilibrium composition if the free stream gas composition mixture and the thermodynamic state is known. For the sake of simplicity, the detailed procedure adopting the five species chemical model is presented and the assumption of pressure and temperature are provided. Formation matrix

The firsts N_{spe} relations are obtained by defining, for any chemical reaction, a pressure equilibrium constant:

$$K_p(T) = \prod_{is}^{N_{spe}} p_{is}^{\nu_{is}}$$

where p_{is} is the partial pressure of the is -th species and ν_{is} is the stoichiometric mole number for species is . ν_{is} is positive for products and negative for reactants. Every K_p for each model are known functions determined experimentally, [25].

Considering the model equation:

$$aA + bB \rightleftharpoons cC + dD$$

$$K_p(T) = \frac{(p_A)^a (p_B)^b}{(p_C)^c (p_D)^d} \quad (2.5.2)$$

For example considering the first reaction

$$O_2 + O \rightarrow 2O + O$$

$$K_p(T)_1 = \frac{p_O^2 p_O}{p_{O_2} p_O} = \frac{p_O^2}{p_{O_2}}$$

It is possible to notice that the K_p of the reaction is not influenced by the O that is merely a bullet that causes the dissociation. Considering the 17 reactions that occurs using a five species air model:

$$K_{p1} = K_{p2} = K_{p3} = K_{p4} = K_{p5} = K_{p_{O_2,diss}} = \frac{p_O^2}{p_{O_2}}$$

$$K_{p6} = K_{p7} = K_{p8} = K_{p9} = K_{p10} = K_{p_{N_2,diss}} = \frac{p_N^2}{p_{N_2}}$$

$$K_{p11} = K_{p12} = K_{p13} = K_{p14} = K_{p15} = K_{p_{NO,diss}} = \frac{p_N^2 p_O}{p_{NO}}$$

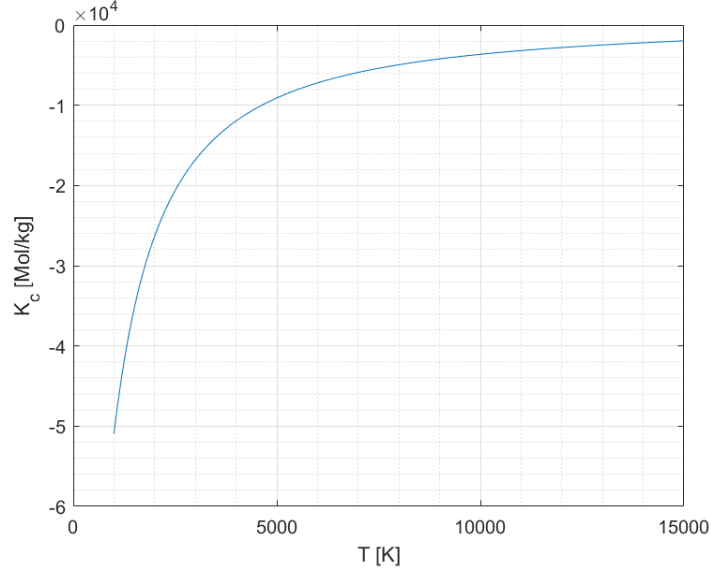
$$K_{p16} = \frac{p_N p_{O_2}}{p_{NO} p_O}$$

$$K_{p17} = \frac{p_N p_{NO}}{p_{N_2} p_O}$$

At this point, several considerations can be made. First, it is possible to plot the equilibrium constants of dissociation reactions as a function of the temperature, figure 2.3. The trend is exponential, and it grows with temperature, which means that at higher temperatures the equilibrium of the reaction is more shifted towards products. This is in perfect agreement with the appearance of molecular nitrogen and oxygen at high temperature.

Second, it must be pointed out that the five coefficients are not independent, only three of them are. The last two are a linear combination of the first three.

Consequently, we have only three linearly independent relations. The remaining two are obtained by imposing the conservation of atoms. In fact, there are no nuclear reactions that cause the change of atoms from one element to another.


 Figure 2.3: $K_{cO_2,diss}(T)$

Therefore, there is the conservation of the total number of atoms of each element and also the mass of gas is preserved:

$$\frac{N_{ie}}{m} = const = \sum_{is}^{N_{spe}} \frac{a_{ie,is} N_{is} N_A}{m} = N_A \sum_{is}^{N_{spe}} a_{ie,is} q_{is}$$

So the remaining N_{ie} relations are:

$$\sum_{is}^{N_{spe}} a_{ie,is} q_{is} = const$$

Where $a_{ie,is}$ is the coefficient in the formation matrix, it specifies how many atoms of each element are needed to create a molecule for each species.

In conclusion, the equilibrium composition of a gas mixture can be computed by $N_{spe} - N_{ele}$ equilibrium constant equations and N_{ele} mass conservation equations. Furthermore, a concentration equilibrium K_c constant is interchangeable with the pressure one K_p , this is explained in section 2.7.2.

$$K_{ir}^c(T) = \prod_{is}^{N_{spe}} (\rho q_{is})^{\Delta \nu_{is}} \quad (2.5.3)$$

$$\sum_{is}^{N_{spe}} a_{ie,is} q_{is} - \sum_{is}^{N_{spe}} a_{ie,is} q_{is,0} = 0 \quad (2.5.4)$$

2.6 Internal Energy

Previously it has been mentioned that, as the temperature increases, the degrees of freedom of the molecules increase and it is necessary to consider also the vibrational and electronic ones. The purpose of this section is to justify and provide the mathematical models that have been adopted for the study of internal energy distribution. The internal energy of a molecule consists of two contributions, the first translational and the second relates to the internal geometry of the molecule. According to the Bohr-Oppenheimer model, the internal energy of a molecule is composed of four different contributions:

$$\varepsilon' = \varepsilon'_t + \varepsilon'_r + \varepsilon'_v + \varepsilon'_e \quad (2.6.1)$$

where:

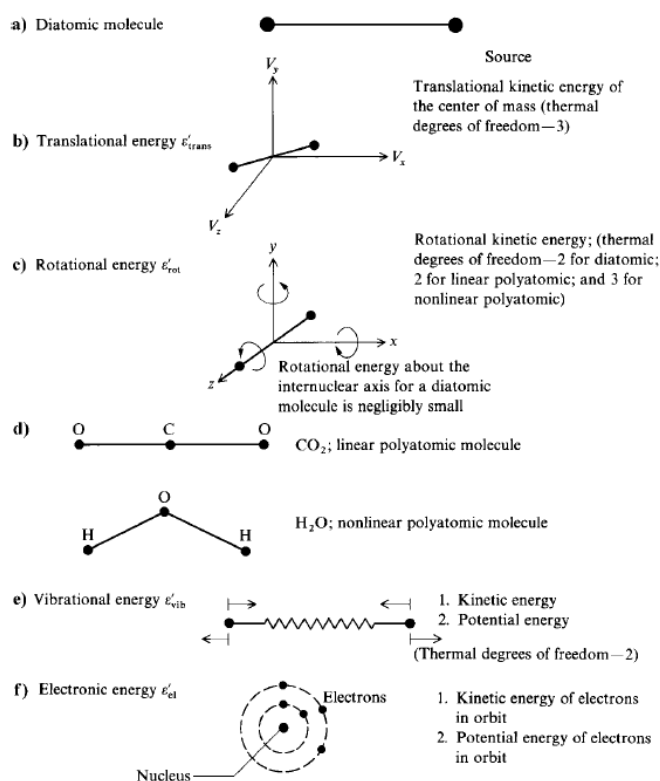


Figure 2.4: Modes of molecular energy [2]

ε'_t is the translational energy. The kinetic translational energy of the centre of mass of the molecule is the origin of this energy. The velocity is a vector in space and so it has three components and this implies that molecules have three translational degrees of freedom.

ε'_r is the rotational energy. The rotational kinetic energy associated with the molecule's rotational velocity and its moment of inertia are the origin of this energy. Molecules made of only one atom (e.g. O , N , e^-) do not have this energy contribution. It involves two degrees of freedom for linear polyatomic (e.g. CO_2) and diatomic molecules moment of inertia about the internuclear axis is small, and therefore the rotational kinetic energy about this axis is negligible. It involves three degrees of freedom for non-linear polyatomic molecules.

ε'_v is the vibrational energy and it is owned by molecules only. The atoms of the molecules vibrate around their equilibrium location. For a diatomic molecule, this vibration can be seen as a spring connecting the two atoms. In this case, there are two sources of vibrational energy: kinetic and potential energy and the diatomic molecule which has two thermal degrees of freedom. In general, for a diatomic or linear molecule, there are $2(3n - 5)$, with n the number of atoms. For polyatomic molecules, the vibrational motion is more complicated, and there are $2(3n - 6)$ degrees of freedom.

ε'_e is the electronic energy. The electrons have both potential energy, because of the presence of the atomic electromagnetic field, and kinetic energy. When interactions between molecules and electrons occur they can change orbitals and so the energy level change.

It is possible to compute the sensible energy level for a molecule. Classical thermodynamics can estimate with good accuracy the internal energy up to about $800K$, it turns out to be a very good model for the calculation of translational and rotational energy.

$$e_t = \frac{L_t}{2} R_i T \quad (2.6.2)$$

$$e_r = \frac{L_r}{2} R_i T \quad (2.6.3)$$

where e is the energy of a molecular species per unit mass and L the degrees of freedom.

However, this model is inaccurate in calculating the vibrational contribution and for this reason it is necessary to use quantum mechanics. Quantum mechanics states that energy can only be exchanged in discrete quantities. In particular, the different energy levels are separated by steps. The steps in the translational and rotational energy are so close that they can be seen as continuous, figure 2.5, and this is the reason why classical thermodynamics works properly at low temperatures. The steps in the vibrational and electronic energy are significant and this means that a great amount of energy is needed to reach the next vibrational or electronic level. The harmonic oscillator model is adopted to calculate the vibrational energy and this implies the hypothesis that all the steps are equal. For the considered range of

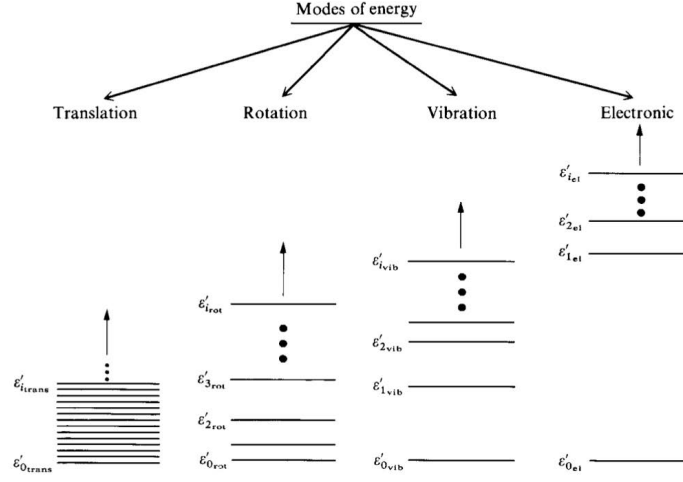


Figure 2.5: Schematic of energy levels for the different molecular energy modes [2]

temperature this is a properly approximation. The maximum number of vibrational energy levels corresponds to the highest vibrational energy level whose energy is lower than the dissociation energy. Quadratic and cubic models are more accurate but they match the result of the harmonic oscillator for our cases. It is possible to define the characteristic temperature of vibration θ_i

$$\theta_i = \frac{h\nu_i}{k_B} \quad (2.6.4)$$

where k_B and h are respectively the Boltzmann and Planck constant. ν_i is the fundamental vibration frequency of the molecule. θ_i depends on the species. The vibrational energy per unit of mass is:

$$e_i^v = \frac{R_i\theta_i}{\theta_i} \frac{1}{e^{\frac{T}{\theta_i}} - 1} \quad (2.6.5)$$

As it can be observed in the previous formula, vibrational energy is a function of temperature only. So it is possible to calculate the energy for:

molecule with a single atom $e = \frac{3}{2}RT + e_e$

molecule with a two atoms or linear $\frac{3}{2}RT + RT + \frac{R_i\theta_i}{\theta_i} \frac{1}{e^{\frac{T}{\theta_i}} - 1} + e_e$

polyatomic non linear molecule $\frac{3}{2}RT + \frac{3}{2}RT + \frac{R_i\theta_i}{\theta_i} \frac{1}{e^{\frac{T}{\theta_i}} - 1} + e_e$

Ground State : the lowest allowable energy level. In fact, when the temperature reaches $0K$ the molecules have some energy. ϵ' is the absolute energy level, ϵ is the sensible energy. ϵ'_0 is the zero-point energy.

$$\epsilon'_0 = \epsilon'_{0t} + \epsilon'_{0v} + \epsilon'_{0e} \quad (2.6.6)$$

From the equation can be noticed that $\epsilon'_{0r} = 0$. The value of ϵ'_0 depends on the chemical species. The ground state energy must be taken into account when the gas changes its composition because there is a significant variation of ϵ'_0 . However, it is not possible to evaluate directly the ground state of a chemical species, so it is necessary to introduce the heat of reaction and formation to overcome this problem.

2.6.1 Heat of Reaction and Formation

When a chemical reaction occurs energy can be absorbed or released. The heat of reaction is defined as the amount of heat that must be added or removed during a chemical reaction, in order to keep all of the substances at the same temperature. If the pressure of the system is kept constant, the heat of reaction also represents the change in enthalpy ΔH .

$\Delta H > 0$ the reaction is endothermic

$\Delta H < 0$ the reaction is exothermic

The standard conditions for a gas are a pressure of $101325 Pa$ and a temperature of $25.17C$. Standard heat of formation of a compound is the change of enthalpy during the formation of 1 mole of the substance from its constituent elements, with all substances in their standard states. All elements in their standard states (N_2 , O_2) have a standard enthalpy of formation of zero. In particular, the enthalpy of a gas mixture is:

$$h = \sum_{is}^{N_{spe}} q_{is}(H - \epsilon)_{is} + \sum_{is}^{N_{spe}} q_{is}\epsilon_{is} \quad (2.6.7)$$

where the first term is the sensible enthalpy. The equation (2.6.7) can be written using the heat of formation at $0K$:

$$h = \sum_{is}^{N_{spe}} q_{is}(H - \epsilon)_{is} + \sum_{is}^{N_{spe}} q_{is}(\Delta H_f)_{is}^0 \quad (2.6.8)$$

The last term is crucial in hypersonic and high temperature analysis because the formation of new species through dissociation reactions requires energy and this involves a reduction of the temperature. In conclusion, the relations to find thermodynamic properties of gas behind a shock wave for a calorically perfect gas give higher temperature values than those actually reached, because, it does not consider chemical reactions.

2.7 Non-Equilibrium

Behind a shock wave the thermodynamics conditions change rapidly and a certain amount of time is required by a fluid particle to adapt to the new conditions. Furthermore, at each point of the flow field, the conditions are different so also the asymptotic conditions of equilibrium continuously change.

2.7.1 Vibrational Non-equilibrium

The translational and rotational energy rebalance almost instantly and they are always supposed in equilibrium. The vibration and electronic energy require more collision to rebalance. One of the possible effects of collision is the exchange of energy between molecules. There are two main models that describe the exchange of energy

T-V transfer : vibrational-translational energy exchange. This is statistically the most expected exchange method.

$$A(v) + B(v') \rightleftharpoons A(v - 1) + B(v') + KE \quad (2.7.1)$$

where v and v' are the vibrational levels of the two molecules. In equation (2.7.1) the energy lost by a molecule results in an increase of the translational kinetic energy of the molecules. This model provides an energy exchange of only one quantum at a time. The vibrational energy levels are no more the same so a non-equilibrium condition occurs and the vibrational rate equation is given by:

$$\left(\frac{de_i^v}{dt} \right) = \frac{e_i^{v,eq} - e_i^v}{\tau_i^{V-T}} \quad (2.7.2)$$

where $e_i^{v,eq}$ is the vibrational energy in equilibrium condition, e_i^v the instant vibrational energy, τ_i^{V-T} is the relaxation time and it depends on thermodynamics conditions (p, T) and the composition of the mixture. In general, atoms are more effective in transferring energy so τ_i^{V-T} are smaller.

V-V transfer : vibrational-vibrational energy exchange. If an hanarmonic model is adopted kinetic energy excess occurs due to the different magnitude of steps in the vibrational levels.

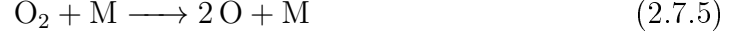
$$A(v) + B(v') \rightleftharpoons A(v - 1) + B(v' + 1) + KE \quad (2.7.3)$$

However, if the harmonic model is adopted there is no energy excess:

$$A(v) + B(v') \rightleftharpoons A(v - 1) + B(v' + 1) \quad (2.7.4)$$

2.7.2 Chemical Non-Equilibrium

In the non-equilibrium phase, the gas composition changes. For example, consider the reaction



the rate of reaction is

$$\left(\frac{d[\text{O}]}{dt} \right)_f = 2k_f[\text{O}_2][\text{M}] \quad (2.7.6)$$

where $[\text{M}]$ is the molar concentration of the species M . The f states that the (2.7.6) is the speed of the forward reaction. The reaction can also occur in the opposite direction



$$\left(\frac{d[\text{O}]}{dt} \right)_b = -2k_b[\text{O}]^2[\text{M}] \quad (2.7.8)$$

The net rate of formation of O in this case is

$$\left(\frac{d[\text{O}]}{dt} \right) = \left(\frac{d[\text{O}]}{dt} \right)_f + \left(\frac{d[\text{O}]}{dt} \right)_b \quad (2.7.9)$$

When the equilibrium condition is reached the composition does not change anymore.

$$2k_f[\text{O}_2]_{eq}[\text{M}]_{eq} - 2k_b[\text{O}]_{eq}^2[\text{M}]_{eq} = 0 \quad (2.7.10)$$

$$k_f = k_b \frac{[\text{O}]_{eq}^2}{[\text{O}_2]_{eq}} \quad (2.7.11)$$

From the definition of K_p 2.5.2. it is possible to define the constant of reaction K_c

$$K_c = \frac{k_f}{k_b} = \frac{1}{RT} K_p \quad (2.7.12)$$

Each chemical reaction can be written in the form

$$\sum_i^{N_{spe}} \nu'_i X_i \rightarrow \sum_i^{N_{spe}} \nu''_i X_i \quad (2.7.13)$$

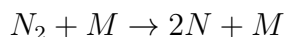
The general form of law mass action describes the variation of the X_i chemical species

$$\frac{d[X_i]}{dt} = (\nu''_i - \nu'_i) \left(k_f \prod_{j=1}^{N_{spe}} [X_j]^{\nu'_j} - k_b \prod_{j=1}^{N_{spe}} [X_j]^{\nu''_j} \right) \quad (2.7.14)$$

The chemical rates constants k_f, k_b can be measured experimentally but in some cases, they can be calculated. In this analysis the Arrhenius equation will be used:

$$k_f = c_1 T^\alpha e^{\frac{-\varepsilon_a}{KT}} \quad (2.7.15)$$

where c_1, α are constants which comes from experimental data, while ε_a is the energy activation. In case the reaction is a dissociation reaction, then the activation energy is the difference between the zero-point energies of the products and of the reactants and it is the dissociation energy. For instance the dissociation reaction of N_2



The dissociation energy is

$$\varepsilon_d = \Delta\varepsilon_0 = 2(\varepsilon_0)_N - (\varepsilon_0)_{N_2}$$

2.8 Governing Equation

The Navier–Stokes equations describe the evolution of a fluid stream. They mathematically express the conservation of mass, momentum and energy.

2.8.1 Non reacting gas

This section describes the equations are for an unsteady, compressible, viscous, three dimensional, chemically non-reacting, chemical and vibrational equilibrium flow. Several assumptions have to be made:

- Continuum fluid. This condition involves that the Knudsen number

$$Kn = \frac{\lambda}{L} < 0.01 \quad (2.8.1)$$

where λ is the free molecular path and L the characteristic dimension of the body or the flow field. This condition is respected only during the flight in the lower layers of the atmosphere. The continuum hypothesis means that the local thermodynamic properties of a fluid element can be defined as the average over its component molecules. When the $Kn \approx 0.1$ it is still possible to adopt the Navier-Stokes equations but the wall conditions must be changed accordingly. When the $Kn > 1$ the molecules are significantly apart and Monte Carlo simulations are implemented.

- There is the conservation of mass and energy. Relativistic and nuclear reactions do not occur.

- Stoke's hypothesis. The term of the bulk viscosity is zero so there is a linear relation between the first μ , and the second λ , coefficient of viscosity

$$\lambda = -\frac{2}{3}\mu \quad (2.8.2)$$

- Newtonian fluid. There is a linear relation between the stress and deformation tensor.

$$\tau_{ij} = \delta_{ij}\lambda\nabla \cdot \mathbf{v} + \mu\left(\frac{\partial u_i}{\partial x_j} + \frac{\partial u_j}{\partial x_i}\right) \quad (2.8.3)$$

- Fourier fluid. It implies a linear relation between the conduction heat flux and the temperature gradient.

$$\dot{\mathbf{q}} = -k\nabla T \quad (2.8.4)$$

where k is the thermal conductivity coefficient.

The set of the differential governing equations that represent the conservation of mass, momentum and energy in the conservative form are

$$\frac{\partial \rho}{\partial t} + \nabla \cdot (\rho \mathbf{v}) = 0 \quad (2.8.5)$$

$$\frac{\partial(\rho \mathbf{v})}{\partial t} + \nabla \cdot (\rho \mathbf{v} \mathbf{v}) = -\nabla p + \nabla \cdot \tau \quad (2.8.6)$$

$$\frac{\partial(\rho E)}{\partial t} + \nabla \cdot (\rho \mathbf{v} E) = -\nabla \cdot (p \mathbf{v}) + \nabla \cdot \tau \cdot \mathbf{v} + \nabla \cdot \dot{\mathbf{q}} \quad (2.8.7)$$

2.8.2 Reacting Non-Equilibrium Gas

This section presents the balance equations for chemically reacting non-equilibrium flow.

2.8.3 Mass balance

For chemically reacting viscous flows further balance equations for the mass of the single species must be added, because of the condition of chemical non-equilibrium. In a control volume fixed in space, the mass of the i -th species contained inside such a control volume can change in time only if:

1. there is a net flux of the species i -th through the surface surrounding the volume: $\int_S \rho_i \mathbf{v} \cdot \mathbf{n} dS$

2. there is production or extinction of the species i inside the volume due to chemical reactions. $\int_V \Omega_i^{ch} dV$ is the term of production of i -th species, where Ω_i^{ch} is the local rate of change of ρ_i because of chemical reactions

$$\rho_i = [X_i] \mathcal{M}_i$$

$$\begin{aligned} \Omega_i^{ch} &= \frac{d\rho_i}{dt} = \mathcal{M}_i \frac{d[X_i]}{dt} = \\ &= \mathcal{M}_i \sum_{r=1}^{N_r} \left(\frac{d[X_i]}{dt} \right)_r = \sum_{r=1}^{N_r} (v_i'' - v_i')_r \left\{ k_{fr} \prod_{j=1}^{N_s} [X_j]^{v_{jr}'} - k_{br} \prod_{j=1}^{N_s} [X_j]^{v_{jr}''} \right\} \end{aligned} \quad (2.8.8)$$

3. there is a net diffusive flux of the i -th species through the surface surrounding the volume due to the viscous effects: $\int_S \mathbf{J}_{mi} \cdot \mathbf{n} dS$. It is defined the average gas velocity:

$$\mathbf{v} = \frac{\rho \mathbf{v}}{\rho} \quad (2.8.9)$$

Different chemical species can have different velocities, \mathbf{v}_i is the velocity of the i -th chemical species.

$$\mathbf{w}_i = \mathbf{v}_i - \mathbf{v} \quad (2.8.10)$$

where \mathbf{w}_i is the diffusion velocity.

The species mass diffusive fluxes \mathbf{J}_{mi} are related to the corresponding diffusion velocities \mathbf{w}_i .

$$\mathbf{J}_{mi} = \rho_i \mathbf{w}_i \quad (2.8.11)$$

\mathbf{J}_{mi} depends on the concentrations, temperature and pressure gradients

$$\mathbf{J}_{mi} = -\rho \mathcal{D}_{im} \nabla y_i + \frac{1}{T} D_i^T \nabla T + \frac{1}{p} D_i^p \nabla p \quad (2.8.12)$$

where \mathcal{D}_{im} is the multi-component diffusion coefficient that is the diffusion coefficient and it expresses the capacity of the i -th species to diffuse in the mixture. \mathcal{D}_{im} is linked to the binary diffusion coefficients \mathcal{D}_{ij} that is the diffusion coefficient of the species i -th into j -th. The approximate relation between them

$$\mathcal{D}_{im} = \frac{1 - X_i}{\sum_j \frac{X_j}{\mathcal{D}_{ij}}} \quad (2.8.13)$$

In conclusion the additional equations of mass balance in conservative and integral are:

$$\frac{\partial}{\partial t} \int_V \rho_i dV + \int_S \rho_i \mathbf{v} \cdot \mathbf{n} dS + \int_S \mathbf{J}_{mi} \cdot \mathbf{n} dS = \int_V \Omega_i^{ch} dV \quad (2.8.14)$$

In differential form:

$$\frac{\partial \rho}{\partial t} + \nabla \cdot (\rho \mathbf{v}) + \sum_i^{N_s} \mathbf{J}_{mi} = \sum_i^{N_s} \Omega_i^{ch} \quad (2.8.15)$$

Furthermore, from the global mass balance

$$\frac{\partial \rho}{\partial t} + \nabla \cdot (\rho \mathbf{v}) = 0 \quad (2.8.16)$$

so

$$\sum_i^{N_s} \mathbf{J}_{mi} = \sum_i^{N_s} \Omega_i^{ch} \quad (2.8.17)$$

Two important conditions are found:

$$\sum_i^{N_s} \mathbf{J}_{mi} = 0 \quad (2.8.18)$$

that physically means the total mass cannot diffuse

$$\sum_i^{N_s} \Omega_i^{ch} = 0 \quad (2.8.19)$$

that implies the conservation of chemical elements.

2.8.4 Momentum

In a chemically reacting gas transport of momentum is modified because the gas viscosity depends on the composition. The mixture viscosity can be calculated from the viscosity of each species using the approximate Wilke's rule:

$$\mu = \sum_i \frac{X_i \mu_i}{\sum_j X_j \Phi_{ij}} \quad (2.8.20)$$

$$\Phi_{ij} = \frac{1}{\sqrt{8}} \left(1 + \frac{\mathcal{M}_i}{\mathcal{M}_j} \right)^{-\frac{1}{2}} \left[1 + \left(\frac{\mu_i}{\mu_j} \right)^{\frac{1}{2}} \left(\frac{\mathcal{M}_j}{\mathcal{M}_i} \right)^{\frac{1}{4}} \right]^2 \quad (2.8.21)$$

However, other models might be used.

2.8.5 Energy

Vibrational non-equilibrium

It is needed to add equations due to consider the vibrational non-equilibrium effect. For simplicity, only the T-V transfer model is taken into account.

$$\frac{De_i^v}{Dt} = \frac{\partial e_i^v}{\partial t} + \mathbf{v} \cdot \nabla e_i^v = \frac{e_i^{v,eq} - e_i^v}{\tau_i^{V-T}} \quad (2.8.22)$$

where e_i^v is the vibrational energy of the i -th species per unit mass of the i -th species. It is possible to find a new form of the previous equation adding the continuity equation multiplied for e_i^v to (2.8.22) multiplied for ρ_i

$$\rho \frac{De_i^v}{Dt} + e_i^v \left[\frac{\partial \rho}{\partial t} + \nabla \cdot (\rho \mathbf{v}) \right] = \frac{\partial \rho e_i^v}{\partial t} + \nabla \cdot (\rho e_i^v \mathbf{v}) = \rho \frac{e_i^{v,eq} - e_i^v}{\tau_i^{V-T}} \quad (2.8.23)$$

This equation is obtained due to avoid numerical problems. The conservative variable, in this case, is ρe_i^v . Using $\rho_i e_i^v$ as a conservative variable could lead to numerical issues when the i -th species is completely or almost completely dissociated.

Energy transport

For a chemically reacting gas, there is also an energy transport caused by the diffusion effect. While diffusing, the species i -th brings with itself the enthalpy of the species i -th.

$$(\mathbf{q}_D)_i = -h_i \rho \mathcal{D}_{im} \nabla y_i \quad (2.8.24)$$

Adding the contributions of all species

$$\mathbf{q}_D = - \sum_i^{N_s} h_i \rho \mathcal{D}_{im} \nabla y_i \quad (2.8.25)$$

the final form of the energy equation is

$$\frac{\partial E}{\partial t} + \nabla \cdot [(E + p)\mathbf{v}] - \nabla \cdot (\boldsymbol{\tau} \cdot \mathbf{v}) - \nabla \cdot \left(k \nabla T + \sum_{i=1}^{N_s} h_i \rho \mathcal{D}_{im} \nabla y_i \right) = 0 \quad (2.8.26)$$

2.9 Boundary conditions

2.9.1 Velocity

At the wall no-slip condition is applied if a viscous model is adopted, otherwise, a condition of tangency is applied. If there is no mass transfer at the wall, that means a solid wall with no ablation, then on the wall surface $u = v = 0$. Otherwise, if there is mass transfer the wall boundary condition becomes $u = 0$, $v = v_w$, where v_w is a known vertical velocity.

2.9.2 Temperature

For compressible viscous flows, the presence of the energy equation requires an additional boundary condition that is usually a boundary condition on the wall temperature or on the wall heat flux. For a chemically reacting gas, the enthalpy diffusion must be taken into account to compute the total heat flux at the wall.

- Prescribed wall temperature, without radiation cooling
- Adiabatic wall

$$\left(k \frac{\partial T}{\partial y} + \rho \sum_i \mathcal{D}_{im} h_i \frac{\partial y_i}{\partial n} \right)_w = 0 \quad (2.9.1)$$

- Radiation-adiabatic wall
- Prescribed wall temperature, with radiation cooling
- Prescribed wall heat flux

2.9.3 Concentrations

The mass fractions of species i – th are one of the variables in a chemically reacting flow. New boundary conditions are needed. The boundary conditions at the wall for y_i involve a chemical interaction between the surface and the gas. The wall may be made of a material that enhances chemical reactions, this is the case of a catalytic wall. Different situations can occur

1. Equilibrium catalytic wall. Chemical reactions are catalyzed at an infinite rate, mass fractions of the species at the wall are their local equilibrium values.
2. Fully catalytic wall. All atoms are recombined, the recombination reactions are exothermic reactions so the recombination process causes heat release to the gas near the wall. The heat released increases both the temperature of the gas near the wall and the heat flux.
3. Non-catalytic wall. No chemical reactions occur at the wall

$$\left(\frac{\partial y_i}{\partial n} \right)_w = 0 \quad (2.9.2)$$

4. Partially catalytic wall. Chemical reactions are catalyzed at a finite rate. Practically this is the real situation but it is complex to simulate because it is necessary to simulate each and every reactions. In general, fully catalytic and non-catalytic simulations are carried out and the real partially catalytic wall condition is in between.

Chapter 3

MATLAB Code

3.1 Introduction

This chapter shows the principal characteristics and features of the self-developed code in MATLAB. There are many advantages of having a self-developed code: there is complete control over the full thermochemical model adopted, numerical techniques of resolution and also intermediate results are available; it also provides access to every single line of the code and the possibility to modify it if necessary. The code has been entirely written in MATLAB and it is based on the code written in FORTRAN by prof. Domenic D'Ambrosio. It has not been a mere operation of translation, in fact, the original code has been simplified. Several numerical functions, such as the resolution of a linear system, have been removed and replaced with suitable embedded routines in MATLAB. The code has been developed in several steps. The chapter starts with a brief description of the code concerning the equilibrium calculation, the model implemented and its validation through different test cases. Afterwards, the code has been further improved, in particular with the computation of thermochemical relaxation and the creation of a user-friendly user interface (UI). Finally, results are presented and commented. In the following chapters, the results obtained from this code have been compared with data obtained by STAR-CCM+ by Siemens for a further validation.

3.2 Code Main Files

The first aim of the code is to compute the equilibrium condition for a gas mixture provided by the user. Several text files provide the basic numerical database:

- Elements Database.dat: it stores the molecular weight of each chemical element that may be present in the reacting mixture. For reasons of generality of use, the list may also contain elements that do not actually appear in the mixture.

- Species Database.dat: it stores information about enthalpy of formation at $0K$ and the vibrational degrees of freedom of each chemical species. For vibrationally excited species in non-equilibrium, the value of the characteristic vibration temperature $\theta_v[K]$ is indicated.
- Vibration Database.dat: it stores the coefficient to compute the relaxation time $\tau_{i,j}^{V-T}$. These coefficients are taken from [25].

The user provides the thermodynamic characteristics of the gas and its chemical composition. The code reads the input and it computes the remaining thermodynamic values. After that, the code executes several checks to control the validity of the input data. It controls that $\sum_1^{N_{spe}} y = 1$, this means that the initial composition is correctly settled on the mathematical and physical point of view. For reasons of numerical stability and convergence of the resolution method if the initial mass mole ratio q_i of a chemical species is zero, the code writes $q_i = 10^{-15} kg Mol^{-1}$.

3.2.1 Thermochemical Model

The choice of a suitable model to solve the problem strongly influences the results. It must be the outcome of a careful evaluation, based on preliminary considerations of a thermodynamic and chemical nature. A preliminary study of the expected results must be carried out. There are different thermochemical models available (2.3). The models that numerically describes the properties of Earth's atmosphere are taken from [25]. Each model has its own formation matrix (2.1). All the reactions are explicitly written and appropriately balanced. The Arrhenius coefficients and energy of activation are also provided. It is possible to calculate the reaction rates using the (2.7.15). It must be highlighted that the reaction rates are not computed for the calculation of the equilibrium conditions, but they are essential for the non-equilibrium case. The constant of equilibrium of each reaction K_c depends on the temperature and it has been fit with the following formula:

$$\ln(K_c) = \frac{a_{r,1}}{z} + a_{r,2} + a_{r,3}\ln(z) + a_{r,4}z + a_{r,5}z^2 \quad (3.2.1)$$

where $z = \frac{10000}{T[K]}$. The coefficients $a_{i,r}, i = 1..5, r = 1..N_{REA}$ have been experimentally determined by Park and presented in [25]. The presence or absence of a reaction in a non-equilibrium context is therefore much more critical than in the case of equilibrium models. In the latter case, it is only necessary to have an adequate number of independent reactions ($N_{spe} - N_{ele}$) to define the associated constants. By adding the condition of atom conservation, a determinate system is obtained. The unknowns are the fractions of the different species.

3.3 Compute Equilibrium Condition

The first task of the software is to compute the equilibrium thermochemical conditions. In particular, given an initial composition and the thermodynamic conditions (a couple of thermodynamic variables between pressure, temperature, density and enthalpy) the aim is to compute the equilibrium conditions. The procedure has been presented in 2.5.1, the equation (2.5.3) and (2.5.4) are used. The value of K_c can vary by many orders of magnitude, figure 2.3. For reasons of numerical stability and avoiding loss of significance at the equation (2.5.3) the logarithm operator is applied:

$$\ln(K_{ir}^c(T)) = \sum_{is}^{N_{spe}} \Delta \nu_{is} \ln(\rho q_{is}) \quad (3.3.1)$$

For equation (2.5.4) the determination of independent processes is needed and a simple but quite effective method has been implemented. Every reaction can be written as a line vector of N_{spe} elements where each element stands for the stoichiometric variation of each chemical species. The first reaction is taken as the first independent process and it creates a matrix of $1 \times N_{spe}$ elements. Iteratively, the following reactions are added as the last line of the matrix. If the matrix increments its rank, a new independent process is found. Otherwise, the reaction is discarded. The problem is not linear due to the effects of the reactions which constitute a highly non-linear problem.

	N2	O2	NO	N	O	NO+N+	N2+ O+	e-
O2+N=2O+N	0	1	0	0	2	0	0	0

(a) First reaction insert in the matrix

	N2	O2	NO	N	O	NO+N+	N2+ O+	e-
O2+N=2O+N	0	1	0	0	2	0	0	0
O2+N2=2O+N2	0	1	0	0	2	0	0	0

(b) Test reaction. First and second reaction are not linear independent

	N2	O2	NO	N	O	NO+N+	N2+ O+	e-
O2+N=2O+N	0	1	0	0	2	0	0	0
N2+N2=2N+N2	1	0	0	2	0	0	0	0

(c) Test reaction. First and second reaction are linear independent

	N2	O2	NO	N	O	NO+N+	N2+ O+	e-
O2+N=2O+N	0	1	0	0	2	0	0	0
N2+N2=2N+N2	1	0	0	2	0	0	0	0
N2+O=2N+O	1	0	0	2	0	0	0	0

(d) Test reaction. Reaction are not linear independent

Figure 3.1: Establishing independent processes

The system of non-linear equations has been presented in 2.5.1, it is solved by

adopting the MATLAB function *fsolve* which implements Newton-Rapson method. The default parameters of *fsolve* have been changed because in particular cases, specifically with the 10-species Earth atmosphere model, the default tolerance has been lowered to ensure better convergence:

MaxIter: 40 000

MaxFunEvals: 100 000

3.4 Thermochemical Relax

The characteristic time required for equilibrium thermodynamic state and equilibrium chemical composition can significantly influence the flow field behind a shock wave. The flow in the relaxation zone is in chemical and thermal non-equilibrium. The calculation of thermochemical relaxation behind the shock wave is far more complex than the calculation of the equilibrium conditions. This case requires an additional kinetic parameter which can be the velocity or the Mach number. The first step is to compute the *freeze flow* post-shock conditions. Immediately after the shock wave, the thermodynamics properties change but the composition remains unaltered. The shock wave is considered as a discontinuity without thickness and the chemical reactions have not enough time to occur. The Rankine-Hugoniot equations for the normal shock are used to compute the *freeze flow* post-shock conditions:

$$\frac{p_2}{p_1} = \frac{\frac{\gamma + 1}{\gamma - 1} \frac{\rho_2}{\rho_1} - 1}{\frac{\gamma + 1}{\gamma - 1} - \frac{\rho_2}{\rho_1}} \quad (3.4.1)$$

$$\frac{\rho_2}{\rho_1} = \frac{1 + \frac{\gamma + 1}{\gamma - 1} \frac{p_2}{p_1}}{\frac{p_2}{p_1} + \frac{\gamma + 1}{\gamma - 1}} \quad (3.4.2)$$

The gas mixture immediately after the shock wave is in chemical and thermal non-equilibrium. In the zone after the shock chemical reactions occur and the gas asymptotically, far from the shock, reaches equilibrium conditions. The set of differential equations describes the behaviour of the mixture behind the shock and it is a stiff problem:

$$F^1 = \rho_0 u_0 = \rho_N u_N \quad (3.4.3)$$

$$F^2 = p_0 + \rho_0 u_0^2 = p_N + \rho_N u_N^2 \quad (3.4.4)$$

$$F^3 = (E_0 + p_0) u_0 = (E_N + p_N) u_N \quad (3.4.5)$$

$$\left[\frac{\partial (\rho_i u)}{\partial x} \right]_N = (\Omega_i^{ch})_N \quad (3.4.6)$$

$$\left[u \frac{\partial (\rho e_i^v)}{\partial x} \right]_N = (\Omega_i^v)_N \quad (3.4.7)$$

3.4.3,3.4.4,3.4.5 equations express the conservation of mass, momentum and energy flows through the shock (they are the integral form of 1.2.4). The 3.4.6 expresses the chemical non-equilibrium and the 3.4.7 expresses the vibrational energy non-equilibrium and the physical nature of this term has been extensively discussed in 2.7. The resolution of the system is carried out adopting the MATLAB function *ode45s* which solves the problem using an adaptive resolution step.

3.5 Code Validation

The final step is the code validation and it is crucial to proceed in the analysis. The code correctly calculates frozen post-shock conditions using Rankine-Hugoniot relations. These results have been validated by the means of tables and online tools. The post-shock equilibrium conditions are more difficult to validate. It is necessary to point out a fundamental difference between equilibrium and non-equilibrium. For the calculation of equilibrium, the equilibrium constants have been calculated using (3.3.1) and $a_{i,r}$ coefficients, whereas, for the non-equilibrium calculation, these coefficients have not been used. For the latter calculation, the Arrhenius coefficients have been implemented. The consistency of the results has to be verified. Far from the shock, the mixture, initially in non-equilibrium, has to tend asymptotically to the previously calculated equilibrium conditions.

3.5.1 Mach 1.5, test case 1

No thermochemical effects occur through a weak shock wave. Therefore the gas composition and the properties calculated with the Rankine-Hugoniot relations must be very close to those at equilibrium. This has been verified for $M = 1.5$ and the output file is provided also by way of example.

```
*****
FREESTREAM CONDITIONS:
*****
Mach          = 1.500000
Speed         = 511.320467 m/s
Temperature= 288.000000 K
Pressure     = 101325.000000 Pa
Density      = 1.220790E+00 Kg/m^3
Composition MASS FRAC:
```

```

y(e-)=0.000000E+00
y(O+)=0.000000E+00
y(N+)=0.000000E+00
y(NO+)=0.000000E+00
y(O)=0.000000E+00
y(N)=0.000000E+00
y(NO)=0.000000E+00
y(N2+)=0.000000E+00
y(O2)=2.329175E-01
y(N2)=7.670825E-01
ev(NO+)=59.829324 J/Kg
ev(NO)=59.828231 J/Kg
ev(N2+)=8.258147 J/Kg
ev(O2)=232.401146 J/Kg
ev(N2)=8.257985 J/Kg
GAMMA          =1.400000
MOL. WEIGHT    =28.850334
cp(t-r)       =1008.675232 [J/kg/K]
T.-R. ENERGY =290498.466909 [J/kg/K]
FORM. ENTHALPY =0.000000 [J/Kg]
VIB. ENERGY  =60.464852 [J/Kg]
KIN. ENERGY  =130724.310109 [J/Kg]
*****
THERE ARE 7 EQUILIBRIUM INDEPENDENT PROCESSES:
reaction # 1: 1[O] + 1[NO] -> 2[O] + 1[N]
reaction # 2: 1[O] + 1[O2] -> 3[O]
reaction # 6: 1[N] + 1[N2] -> 3[N]
reaction # 19: 1[e-] + 1[O] -> 2[e-] + 1[O+]
reaction # 20: 1[e-] + 1[N] -> 2[e-] + 1[N+]
reaction # 21: 1[O] + 1[N] -> 1[e-] + 1[NO+]
reaction # 22: 2[N] -> 1[e-] + 1[N2+]
*****
*** EQUILIBRIUM POST-SHOCK CONDITIONS ***
*****
Mach          =0.699853
Velocity      = 274.024153 [m/s]
Temperature   = 379.973267 [K]
Pressure      = 249448.846464 [Pa]
Density       = 2.277955E+00 [Kg/m^3]
Composition MASS FRAC:
y(e-)=8.625643E-69
y(O+)=1.511442E-133

```

```

y(N+)=9.632075E-227
y(NO+)=1.167963E-12
y(O)=1.035271E-15
y(N)=7.702842E-124
y(NO)=1.856277E-109
y(N2+)=2.968759E-223
y(O2)=2.329175E-01
y(N2)=7.670825E-01
GAMMA          = 1.400000
MOL. WEIGHT    = 28.850334
cp(t-r)       = 1008.675232 [J/kg/K]
T.-R. ENERGY = 383269.623164 [J/kg/K]
FORM. ENTHALPY = 0.000039 [J/Kg]
VIB. ENERGY  = 469.000460 [J/Kg]
KIN. ENERGY  = 37544.618294 [J/Kg]
*****
*** FROZEN POST-SHOCK CONDITIONS ***
*****
Mach           =0.701089
Speed          =274.598029 [m/s]
Temperature=380.222222 K
Pressure       =249090.625000 Pa
Density        =2.273194E+00 kg/m^3
Composition MASS FRAC:
y(e-)=0.000000E+00
y(O+)=0.000000E+00
y(N+)=0.000000E+00
y(NO+)=0.000000E+00
y(O)=0.000000E+00
y(N)=0.000000E+00
y(NO)=0.000000E+00
y(N2+)=0.000000E+00
y(O2)=2.329175E-01
y(N2)=7.670825E-01
ev(NO+)= 59.829324 j/kg
ev(NO)= 59.828231 j/kg
ev(N2+)= 8.258147 j/kg
ev(O2)= 232.401146 j/kg
ev(N2)= 8.257985 j/kg
gamma        = 1.400000
mol. weight  = 28.850334
cp(t-r)     = 1008.675232 [j/kg/k]

```

```

t.-r. energy = 383520.738334 [j/kg/k]
t.-r. energy = 32.000000 [j/kg/k]
form. enthalpy = 0.000000 [j/kg]
vib. energy = 60.464852 [j/kg]
kin. energy = 37702.038684 [j/kg]
*****

```

The mass fractions of chemical species practically remain unchanged. No variations occur between freestream and equilibrium post-shock conditions.

3.5.2 Thermodynamic Properties Ratio, test case 2

The results obtained have been compared with those available in literature, in particular in [2].

flow property	Calorically perfect ($\gamma = 1.4$) [2]	Frozen Post Shock	Equilibrium chemically reacting, [2]	Equilibrium Post shock
p_2/p_1	1233	1300	1387	1448
ρ_2/ρ_1	5.972	5.973	15.19	14.13
T_2/T_1	206.35	217	41.64	46.1

Table 3.1: Test Case 2 $u_1 = 36\,000\text{m/s}$, $h = 170\,000\text{ft}$

There are some differences in the determination of the frozen post-shock condition. In computing the equilibrium post-shock values a 10 species model has been used (O_2^+ has not been taken into account). The model adopted in [2] for computing the equilibrium is unknown. Changing the model from 7 to 10 species leads to drastic variations in the results.

flow property	Equilibrium Post shock	Equilibrium Post shock
	7 species	10 species
p_2/p_1	1384	1448
ρ_2/ρ_1	8.92	14.13
T_2/T_1	77.54	46.1

Table 3.2: Comparison between the results of equilibrium post-shock 7 or 10 species model in Test Case 2

3.5.3 Influence of pressure, test case 3

For a final validation, it has been used the graph 3.2. Some points are computed and the results are very close to those reported in the graph.

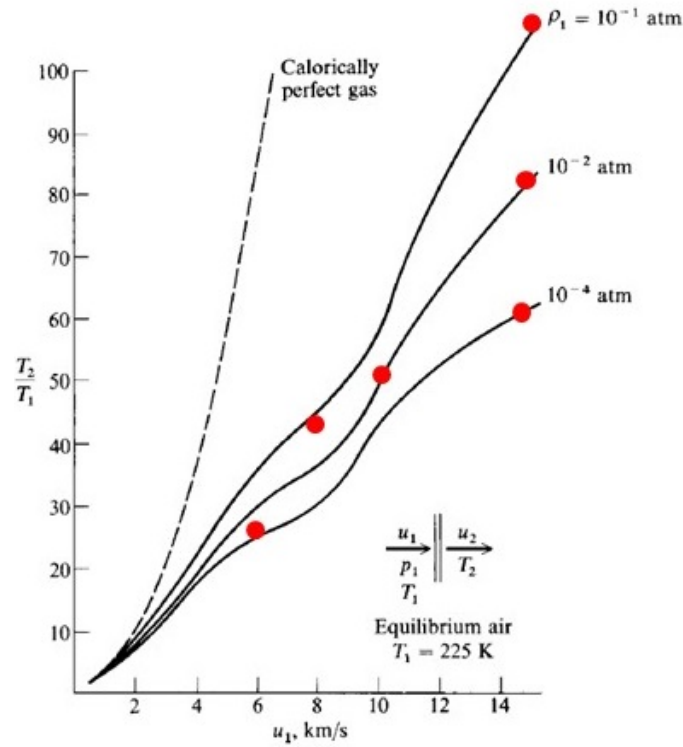


Figure 3.2: Influence of pressure on the normal shock temperature in equilibrium air, [2]

$p[Pa]$	$u_1[km/s]$	T_2/T_1
10132.5	14	102
10132.5	8	43
1013.25	14	85
1013.25	10	54
101.325	14	61.5
101.325	6	25

Table 3.3: Equilibrium Post Shock - 10 species model

3.5.4 Relaxation and equilibrium, test case 4

The results are consistent with the equilibrium conditions that have been previously computed. Away from the shock, both the thermodynamic characteristics (pressure, temperature, density) and the composition of the gaseous mixture reach equilibrium conditions.

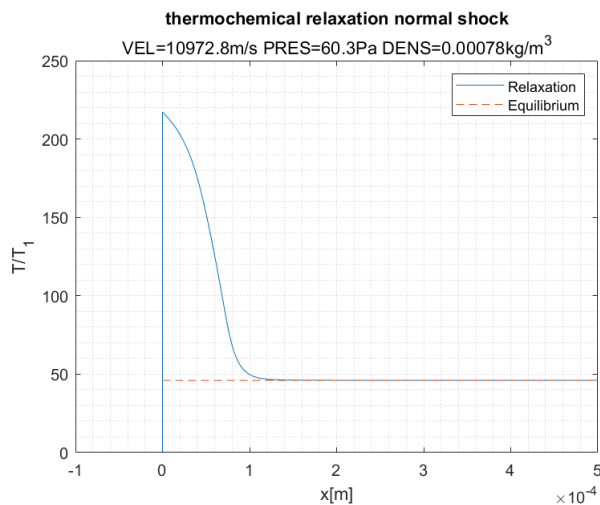


Figure 3.3: Temperature relaxation-10 species model

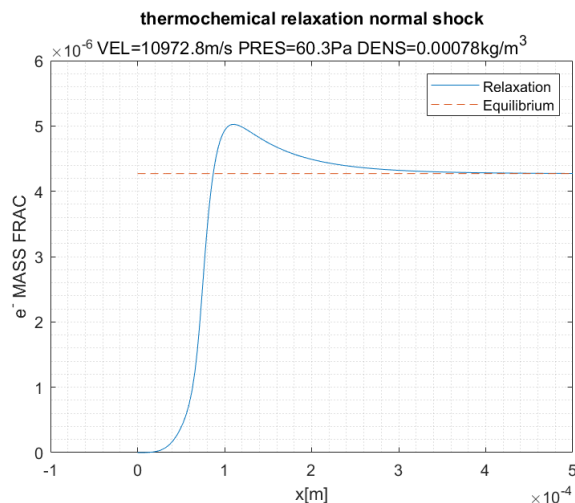


Figure 3.4: e^- mass frac relaxation-10 species model

In figure 3.3 the temperature suddenly increases after the shock. Behind the shock there is a gradual decrease in the temperature due to chemical reactions that are endothermic and they subtract energy from the system. Away from the shock, there is asymptotic attainment of a temperature that corresponds to the independently calculated equilibrium temperature. From figure 3.4 it is possible to notice the strict influence of high speed over the ionization of the gas. The presence of electrons in a hypersonic flowfield downstream of shock is no longer negligible. Furthermore, the growth of the mass fraction of the electrons is not monotone, it reaches a peak followed by a slight decrease.

3.5.5 Validation through CEARUN, test case 5

The last test case is the validation through CEARUN which is an online calculator developed by NASA and available at <https://cearun.grc.nasa.gov/>. It is a powerful and reliable tool that allows the calculation of chemical equilibrium behind a normal shock. The freestream conditions for this benchmark case have been set: $M = 20$, $T = 200K$, $p = 20\,265Pa$. In this comparison, for the MATLAB code, a 10-species model has been used to simulate the Earth's atmosphere.

	CEARUN (NASA)	MATLAB code
T[K]	7575	7558
$\rho[kg/m^3]$	3.73	3.653
$p[Pa]$	$1.03 \cdot 10^7$	$1.028 \cdot 10^7$
$u[m/s]$	536	546
$y(O_2)$	$3.58 \cdot 10^{-3}$	$3.66 \cdot 10^{-3}$
$y(N_2)$	0.648	0.655
$y(O)$	0.202	0.203
$y(N)$	$8.38 \cdot 10^{-2}$	$8.87 \cdot 10^{-2}$
$y(NO)$	$4.83 \cdot 10^{-2}$	$4.92 \cdot 10^{-2}$
$y(NO^+)$	$4.99 \cdot 10^{-4}$	$3.61 \cdot 10^{-4}$
$y(Ar)$	$1.29 \cdot 10^{-2}$	
$y(CO)$	$2.92 \cdot 10^{-4}$	
$y(NO_2)$	$1.70 \cdot 10^{-5}$	
$y(N_2O)$	$4.38 \cdot 10^{-5}$	
$y(O^-)$	$1.43 \cdot 10^{-5}$	
$y(N_2^+)$		$6.27 \cdot 10^{-6}$
$y(O^+)$		$5.19 \cdot 10^{-6}$
$y(N^+)$		$2.72 \cdot 10^{-6}$
$y(e^-)$		$7.00 \cdot 10^{-9}$

Table 3.4: Chemical Equilibrium CEARUN vs MATLAB code

There are some differences between the results provided by this two different tools. The justification lays in the fact that CEARUN adopts a different atmosphere model.

CEARUN (NASA)	MATLAB code
N_2	N_2
N	N
O_2	O_2
O	O
NO	NO
NO+	NO+
Ar	e^-
CO	N+
NO_2	O+
N_2O	N_2+
O^-	-

Table 3.5: Chemical species in CEARUN vs MATLAB code

Chapter 4

One-dimensional Analysis

This section presents the procedure and the results of a one-dimensional thermochemical relaxation CFD simulation. The purpose is to verify the proper setting of the physical model, chemical reactions, solver and all settings in STAR-CCM+. A thermochemical relaxation of a supersonic flow is simulated until equilibrium conditions are reached. The results obtained with the thermochemical model in MATLAB are compared with those obtained by CFD analysis to validate the procedure and eventually to highlight and justify any differences.

4.1 CFD set up

In these simulations, the aim is to simulate one-dimensional thermochemical relaxation of a supersonic flow and study the equilibrium condition reached at the end of the transient. It is not possible to simulate a 1D shock. In fact, after the shock, a subsonic region downstream the shock is formed. This causes the information to flow upstream and there is not enough information on how to set the boundary conditions. The easiest simulation involves a simple two-dimensional constant-section duct with a supersonic flow at both inlet and outlet. The duct must be long enough for the mixture to reach equilibrium. After several preliminary analyses, it has been decided to run each simulation 1000 times. This is a trade-off between the necessary calculation time and the accuracy of the solution.

4.1.1 Mesh

As can be seen in figure [4.1a](#) the duct is very long in one dimension: $50m \times 1m$. The mesh is created using the direct mesh command. The domain is divided into 4 cells in the y-direction and 1000 cells in the x-direction. Overall, there are 4000 cells.

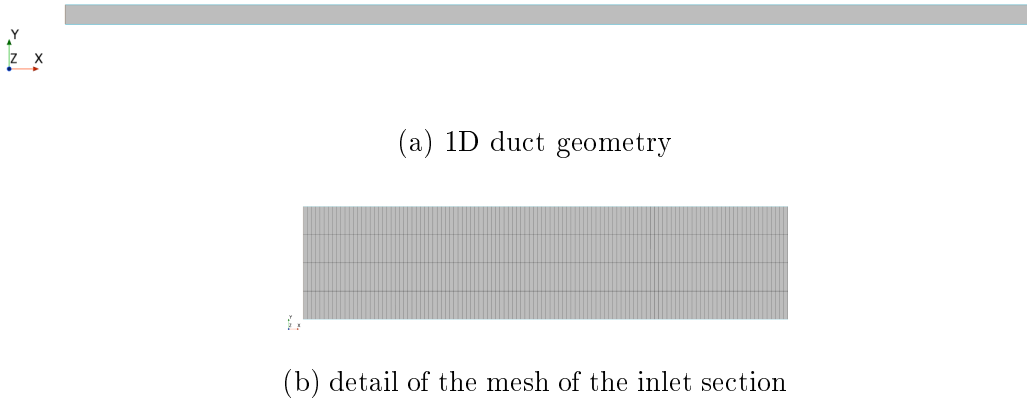


Figure 4.1: Geometry and Mesh 1D analysis

4.1.2 Physical model

STAR-CCM+ provides a large variety of physics models to choose from. The following section covers the physics models chosen for the purposes of this investigation:

- Complex Chemistry
 - Begin at 200 iteration
- Coupled Energy with Enthalpy Formulation option active
- Coupled Flow
- Coupled Species
- Gradients
- Ideal Gas
- Inviscid
- Laminar Flame Concept
- Multi-Component Gas
- Reacting
- Reacting Species Transport
- Steady
- Two-Dimensional

4.1.3 Chemical Species and Reactions

Data of the chemical species involved and the reactions have been implemented in the Complex Chemistry model. Thermodynamic data for individual species have been taken from [16]. Characteristics of gaseous chemical species for temperatures ranging from $200K$ to $20\,000K$ are expressed by NASA polynomials. The coefficients of the NASA polynomials for the different species are given in the appendix A. For each chemical species the equations are defined over three temperature ranges. A chemical model with 10 species and 30 chemical reactions is used. The chemical species involved are:

$$N_2, O_2, NO, N, O, NO^+, e^-, N_2^+, N^+, O^+$$

O_2^+ has not been taken into account because nearly all O_2 has already been dissociated when the ionization occurs. This choice is also shared by Park et al. in the paper [25] where he does not include O_2^+ in the thermochemical model.

The reference values and the default values have been changed:

- Minimum Allowable Absolute Pressure: $1.0 Pa$
- Maximum Allowable Absolute Pressure: $1E9 Pa$
- Minimum Allowable Absolute Temperature: $10 K$
- Maximum Allowable Absolute Temperature: $70\,000 K$
- Reference pressure: $101\,325 Pa$

4.1.4 Boundary, Initials conditions

The inlet and outlet sections are set as freestream with a flow in the x direction. The Mach number is set to 2.5, the pressure $2000 Pa$. The mixture composition changes in each test case. The temperature changes in every simulation in order to reach different equilibrium conditions. It should be noted that each reaction has been tested for a unique range of temperatures. In fact, for example, O_2 dissociation occurs at lower temperatures than ionisation. The external walls have been set as symmetry plane. Detailed information about solver settings can be found at appendix C.

4.2 Test cases and results

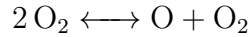
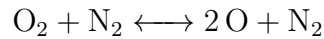
4.2.1 The procedure

Initially, single reactions have been tested. On the outlet section, equilibrium conditions are considered to have been reached. The equilibrium constant K_c is calculated using the molar concentrations of the species which have been obtained at the

end of the simulation. The temperature resulting in the outlet section is taken up as the equilibrium temperature and it is used to calculate K_c using the fitting 3.2.1 proposed by Park et al. [25] (henceforth simply *Park*). Not all reactions covered by the 10-species model have been tested. These simulations are very computationally demanding. Each selected reaction has been tested for about 10 different temperatures. The initial composition changes depending on the reaction.

4.2.2 O_2 dissociation

The following reactions of O_2 dissociation have been studied:

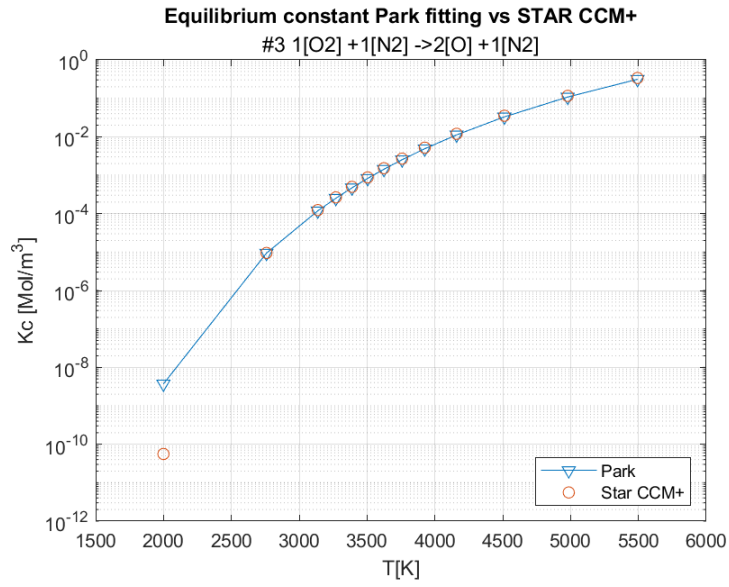


These particular reactions have been chosen because the reactants are the chemical species most present in the atmosphere. In this simulation, the initial condition and the freestream mixture composition are set as the atmospheric composition:

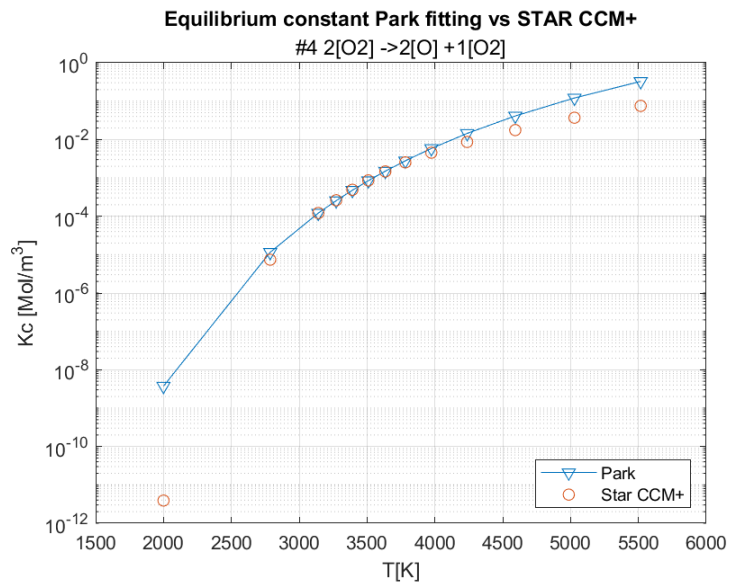
$$y(N_2) = 0.77$$

$$y(O_2) = 0.23$$

where y_i is the mass fraction. In figure 4.2 it is possible to notice that for the temperature range between $2000K$ and $5500K$ the constants of equilibrium have been computed using the output result of the CFD simulation in STAR-CCM+. The K_c resulting values are very close to the Park's fitting curve. It must be noticed that at low temperature ($2000K$), the value of the equilibrium constant proposed by Park and the value calculated numerically from the simulation differ by several orders of magnitude. This may be due to the fact that the empirical curves proposed by Park are correct in the temperature ranges where reactions are most likely to occur. In fact, at low temperatures ($2000K$) dissociations occur, but they are not relevant from the engineering point of view.

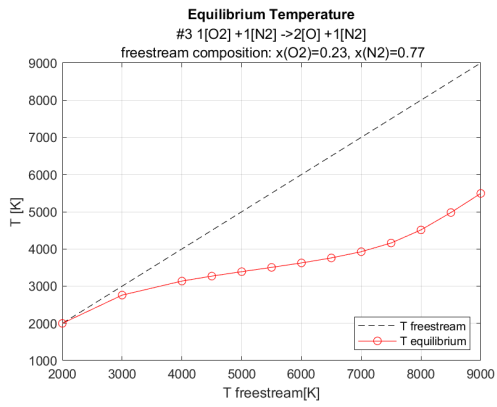


(a) K_c O_2 dissociation

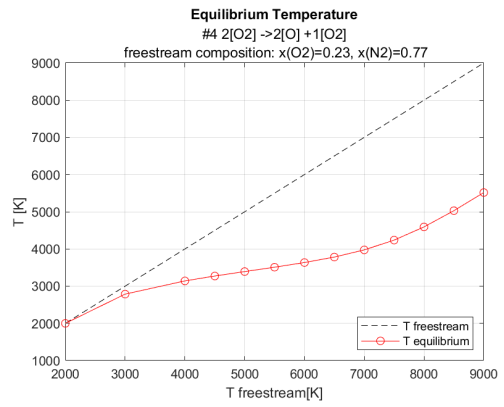


(b) K_c O_2 dissociation

Figure 4.2: Equilibrium Constant of O_2 dissociation comparison



(a) O₂ dissociation

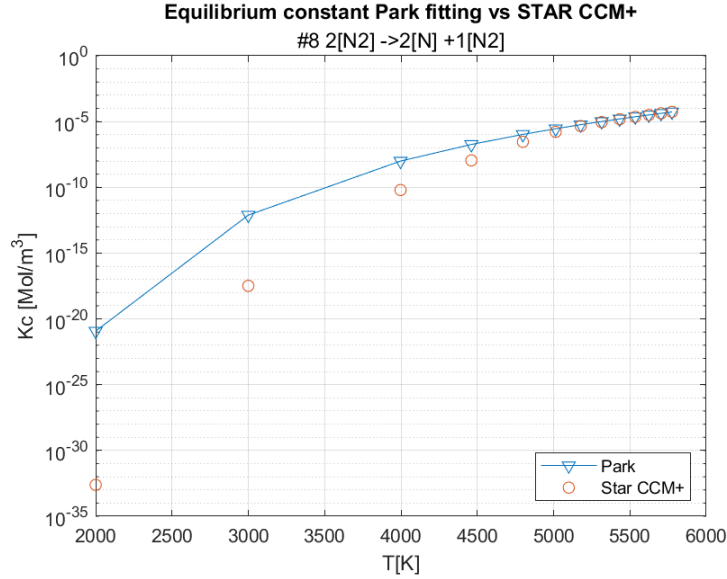
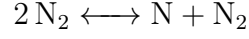


(b) O₂ dissociation

Figure 4.3: Equilibrium Temperature O₂ dissociation

4.2.3 N_2 dissociation

The following reactions of N_2 dissociation have been studied:



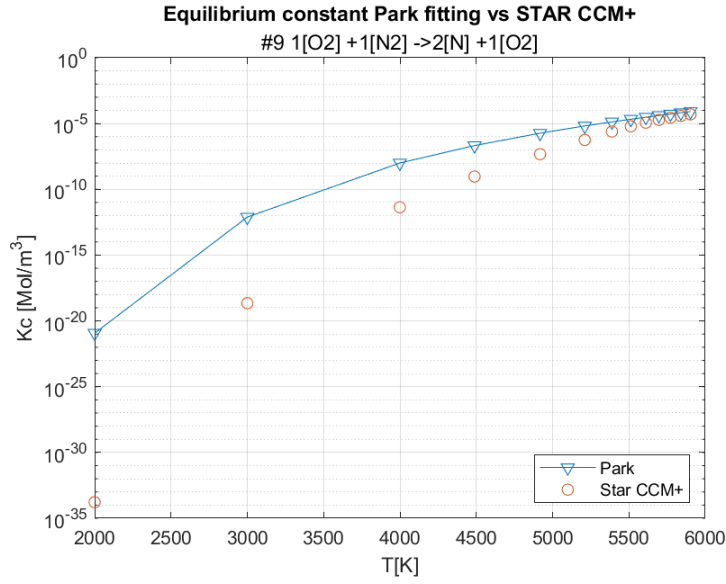
(a) K_c N_2 dissociation

These particular reactions have been chosen because the reactants are the most present chemical species in the atmosphere. In this simulation, the initial condition and the freestream mixture composition are set as the atmospheric composition:

$$y(N_2) = 0.77$$

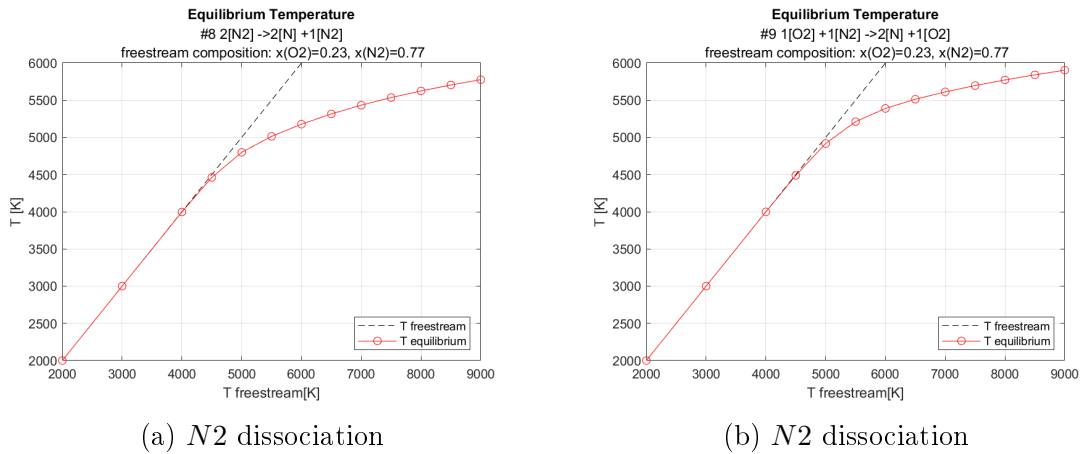
$$y(O_2) = 0.23$$

where y_i is the mass fraction. In figure 4.4 it is possible to notice that for the temperature range between $2000K$ and $5500K$ the constants of equilibrium have been computed using the output result of the CFD simulation in STAR-CCM+. The K_c resulting values are very close to the Park's fitting curve. It must be noticed that in the low-temperature sector ($T < 5000K$) the value of the equilibrium constant proposed by Park and the value calculated numerically from the simulation differ by several orders of magnitude. This may be due to the fact that the empirical curves proposed by Park are correct in the temperature ranges where the reactions are most likely to occur. In fact, at low temperatures dissociations occur, but they are not relevant from the engineering point of view.



(b) K_c N_2 dissociation

Figure 4.4: Equilibrium Constant of N_2 dissociation comparison



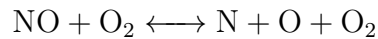
(a) N_2 dissociation

(b) N_2 dissociation

Figure 4.5: Equilibrium Temperature N_2 dissociation

4.2.4 NO dissociation

The following reaction of NO dissociation has been studied:

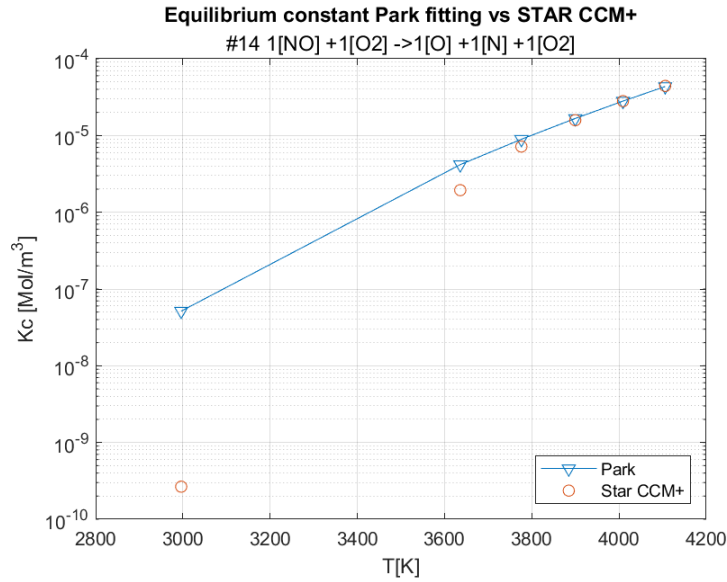


In this simulation, the initial condition and the freestream mixture composition are set as:

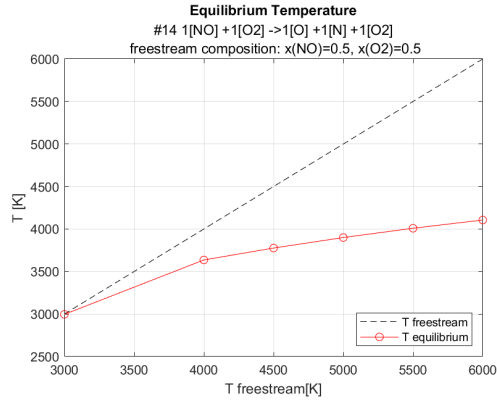
$$y(NO) = 0.5$$

$$y(O_2) = 0.5$$

where y_i is the mass fraction.



(a) *NO* dissociation equilibrium constant comparison

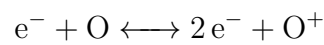


(b) *NO* dissociation equilibrium temperature

Figure 4.6: *NO* dissociation equilibrium constant and temperature

4.2.5 O ionization

The following reaction of *O* ionization has been studied:

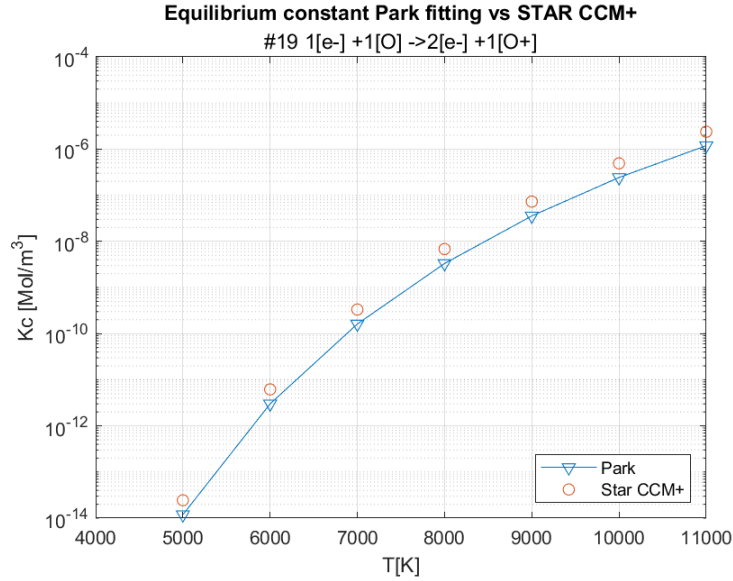


In this simulation, initial condition and the freestream mixture composition are set as:

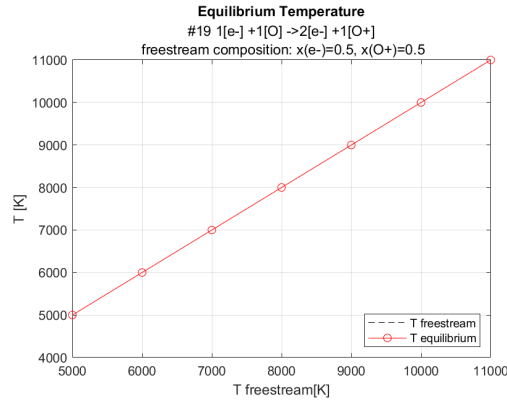
$$y(e^-) = 0.5$$

$$y(O^+) = 0.5$$

where y_i is the mass fraction.



(a) O ionization equilibrium constant comparison



(b) O ionization equilibrium temperature

Figure 4.7: O ionization equilibrium constant and temperature

Figure 4.7a shows that concerning the temperature range between 5000K and

11000K the constants of equilibrium have been computed using the output result of the CFD simulation in STAR-CCM+ and the Park's fitting curve are very close.

In figure 4.7b it can be seen that the equilibrium temperature is equal to the freestream temperature. The temperature does not seem to change. The reason is that the freestream composition is $y(O^+) = 0.5$, $y(e^-) = 0.5$. The electron, e^- , is 30 000 times lighter than the O^+ , so there are many more electrons than oxygen ions. If all the ions react, however, relatively few reactions would take place compared to the molecules in the mixture. The temperature variation is negligible.

4.2.6 Complete model: 30 reactions and 10 species

In this last case, the complete Earth atmosphere model has been implemented. The aim here is not to evaluate the equilibrium constants. CFD simulation has been carried out and the composition of the mixture at equilibrium has been found. The same case is also solved in MATLAB. This procedure allows to verify that the MATLAB code solves the system correctly and also that the model has been recreated and solved correctly in STAR-CCM+.

	STAR-CCM+	MATLAB
e^-	6.225E-12	4.291E-12
N	6.728E-05	6.875E-05
N^+	1.032E-17	4.877E-17
N_2	7.455E-01	7.449E-01
N_2^+	2.147E-14	1.607E-14
NO	5.227E-02	5.362E-02
NO^+	3.405E-07	2.348E-07
O	8.521E-02	8.321E-02
O^+	7.261E-15	2.925E-13
O_2	1.169E-01	1.181E-01

Table 4.1: Mass fractions of the species in the mixture at the equilibrium. $T_{eq} = 3374 K$ $p_{eq} = 62016 Pa$, atmospheric freestream composition $y(O_2) = 0.23$, $y(N_2) = 0.77$

Table 4.1 shows minimal differences in the mixture composition at the equilibrium calculated in MATLAB and in STAR-CCM+. Differences have been found only for species that in this case are almost negligible. For example for N^+ or O^+ where the mass fractions of species are close to machine epsilon.

4.3 Comments and considerations

All results are in line with expectations. The results obtained with STAR-CCM+ are very consistent with those obtained by MATLAB. The methods provide different values of equilibrium constant only at low temperatures. However, in practical terms, this does not invalidate the validity of the results obtained. In fact, these models are not used at low temperatures because no chemical reactions actually take place. Moreover, the differences may also arise from the difficulty of experimentally detecting chemical species that are only present in traces at low temperatures. This results in lower accuracy at lower temperature of the experimental curves proposed by Park. Another reason is the fact that CFD simulations have some limits. In fact the duct is limited and the number of iteration is not infinite. A new simulation of reaction 9 has been carried out. The conduit is 4 times longer than the previous simulation and the iterations are up to 10 000. In this case, at low temperatures, smaller difference between the two models have been observed, figure 4.8.

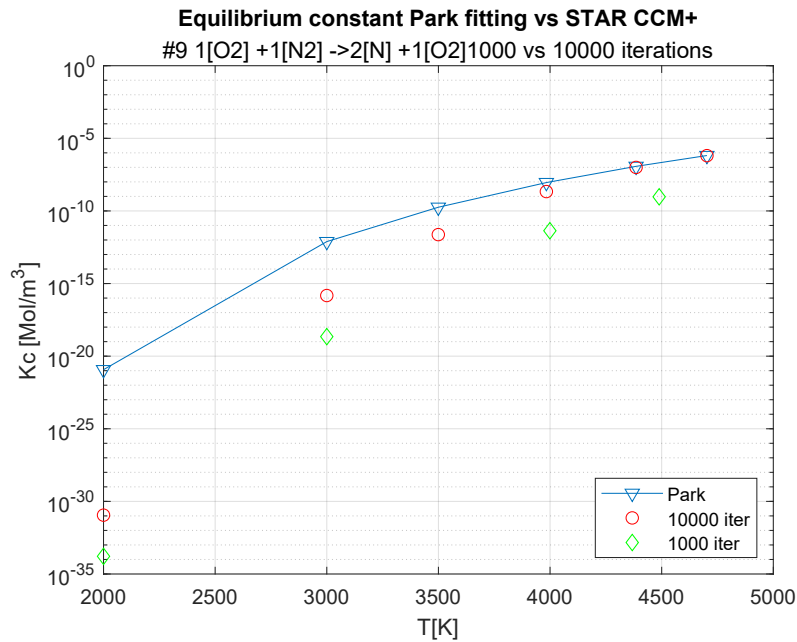


Figure 4.8: K_c NO dissociation, difference between 1000 and 10 000 iterations

The graphs 4.3, 4.5 and 4.6b show that at low temperatures there is minimal change between the freestream and equilibrium temperature. The reason is that no reactions occur. However, at higher freestream the equilibrium temperature is remarkably less than the freestream temperature. The reason is that endothermic reactions occur. They subtract energy to system in order to create new species. This last part of the chapter aims to understand how the commercial software

STAR-CCM+ calculates equilibrium conditions from the thermodynamic properties of chemical species. This procedure makes it possible to highlight any discrepancies between the curves of Park and the Gibbs free energy method for calculating equilibrium.

4.4 Gibbs Free Energy

It is possible to introduce a new, defined thermodynamic variable, the Gibbs free energy per mole of mixture, denoted by G .

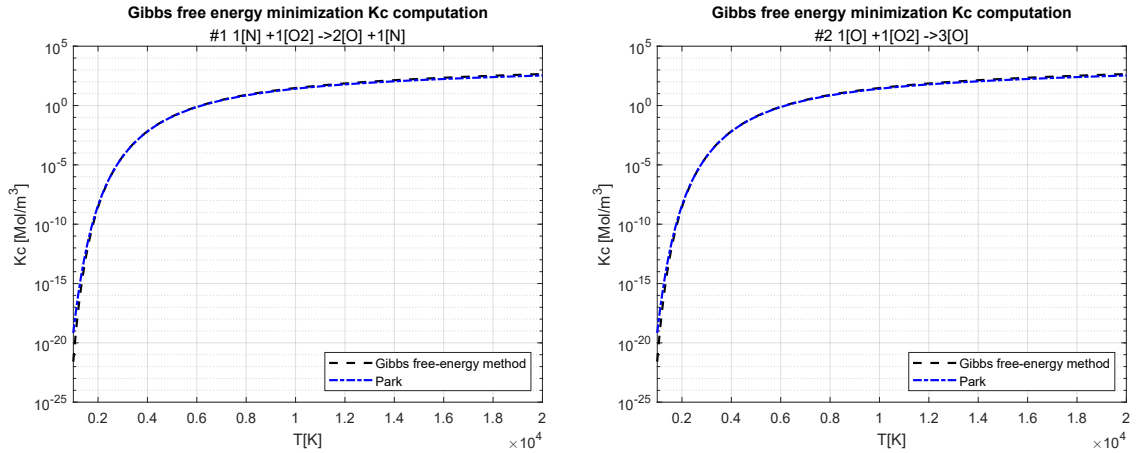
By definition:

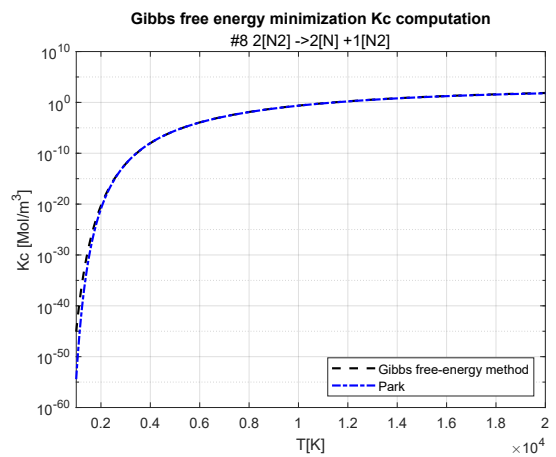
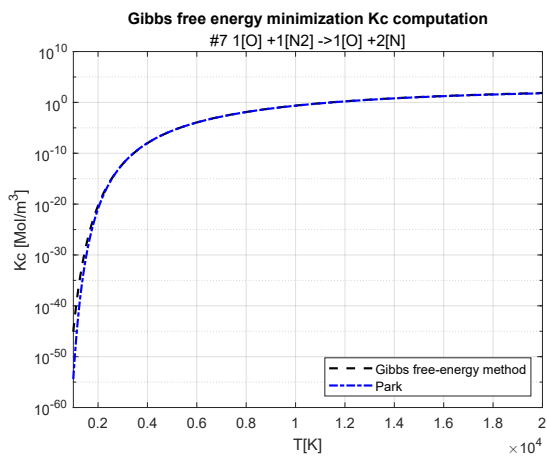
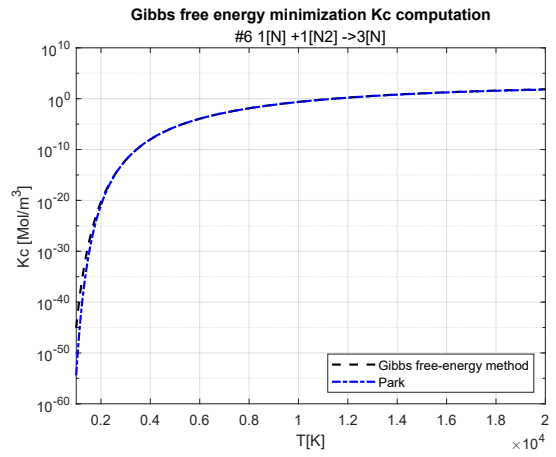
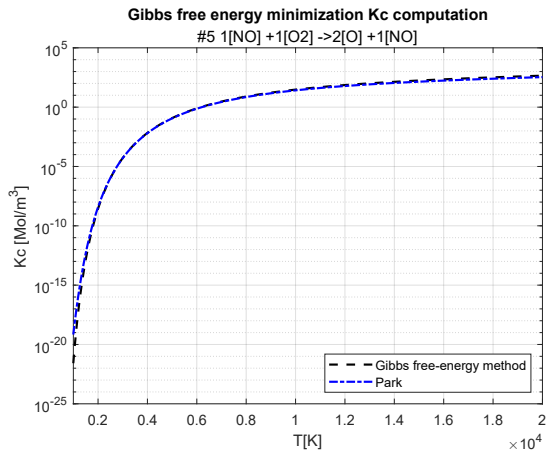
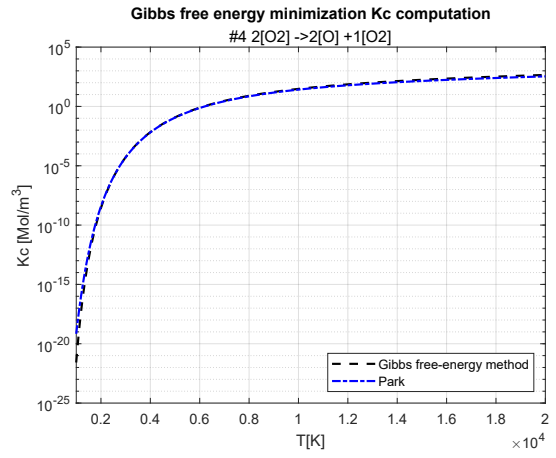
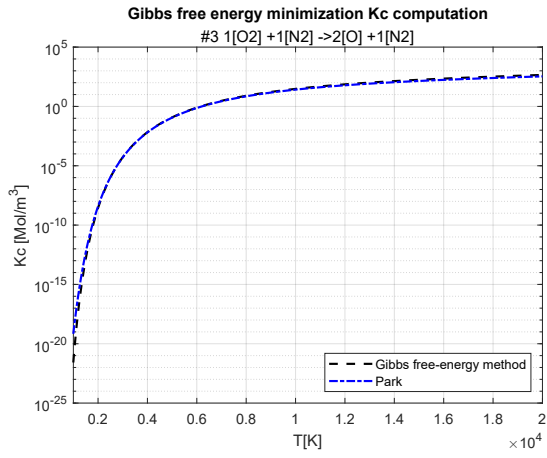
$$G = H - TS \quad (4.4.1)$$

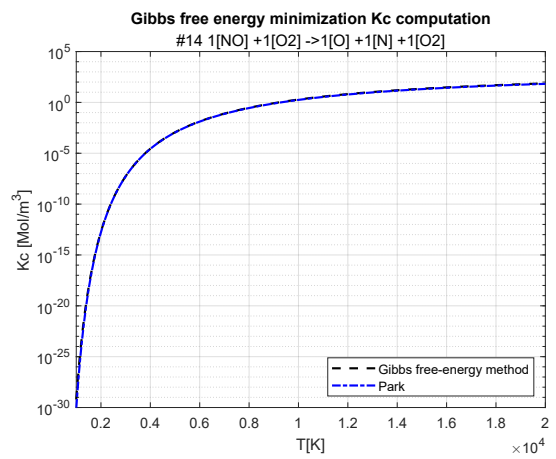
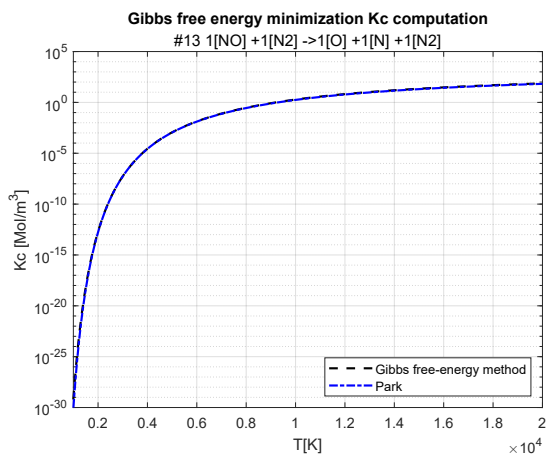
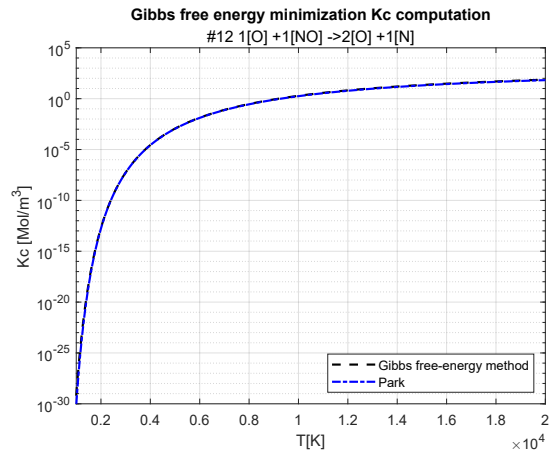
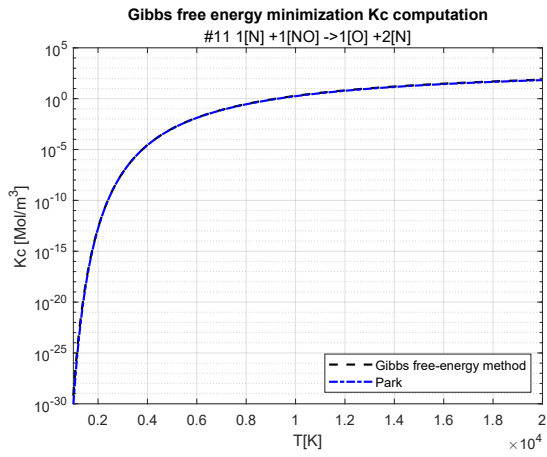
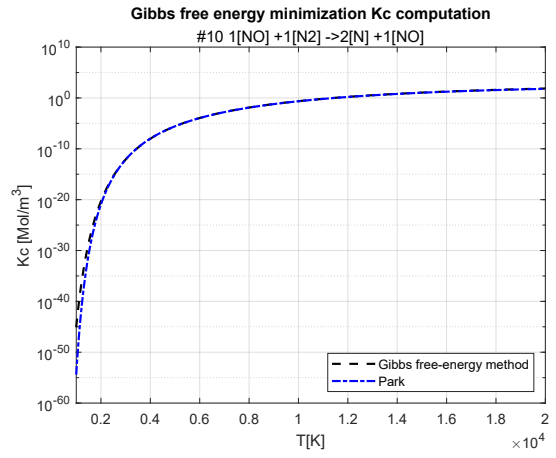
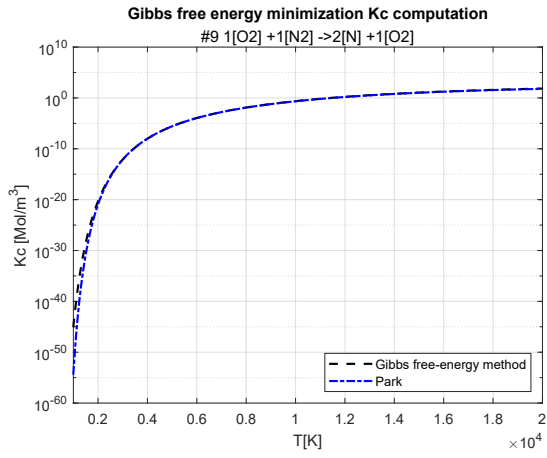
G has been introduced because STAR-CCM+ for computing equilibrium uses Gibbs free-energy minimization technique. It is possible to calculate the equilibrium constant from G , as demonstrated in the appendix B. The Gibbs free-energy has been computed using the thermochemical data in appendix A.

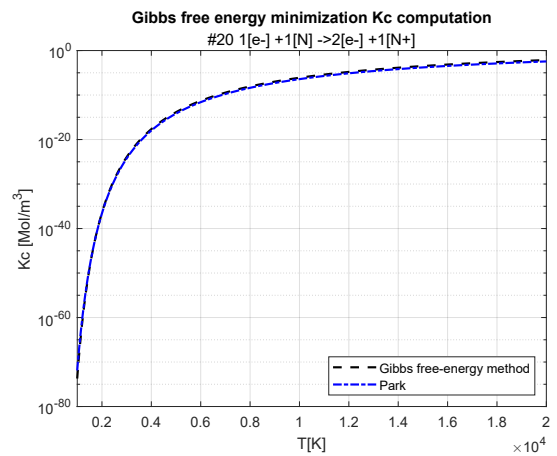
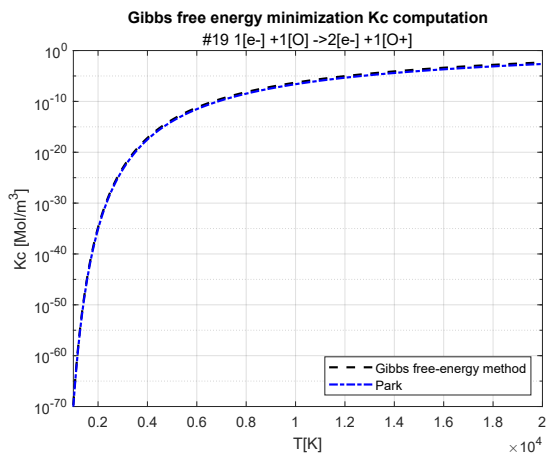
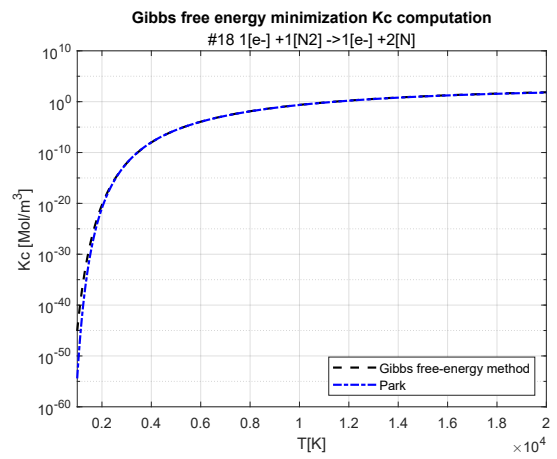
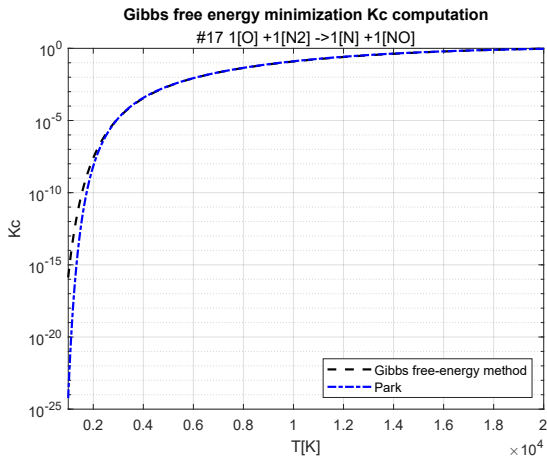
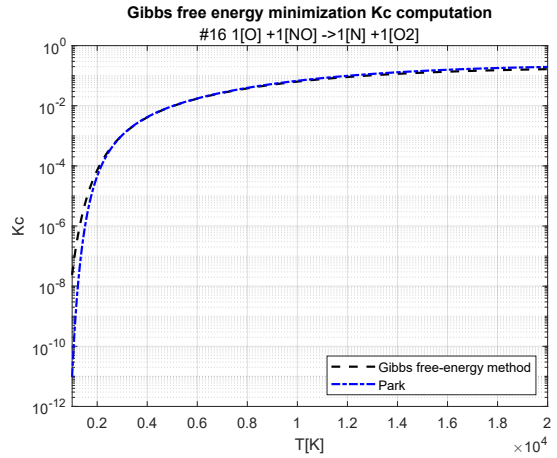
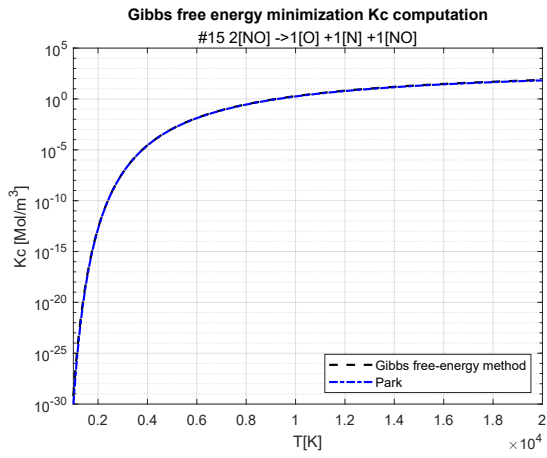
4.5 Park and Gibbs Free Energy comparison

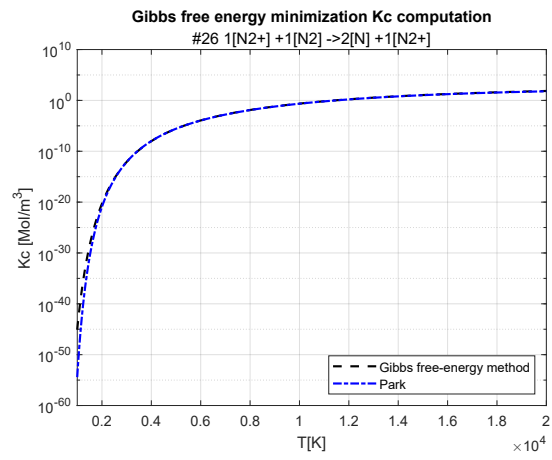
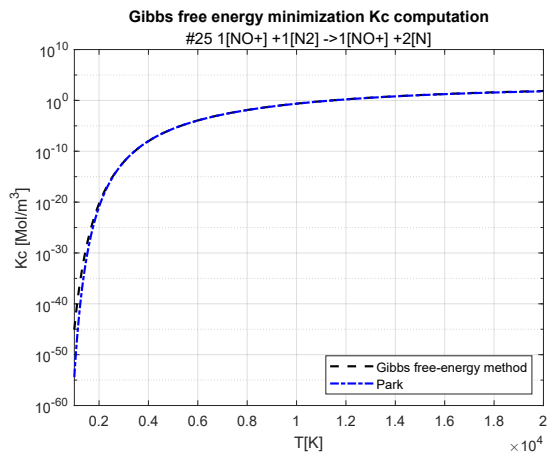
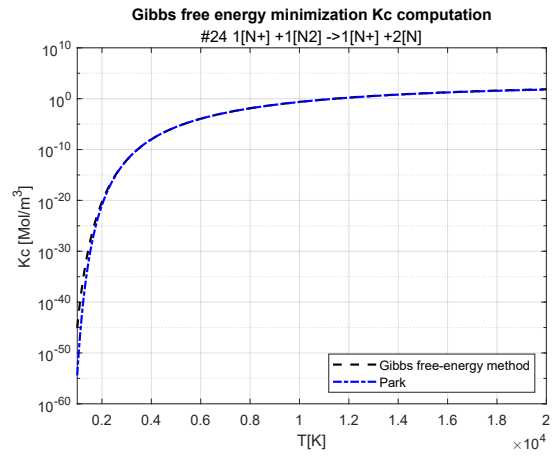
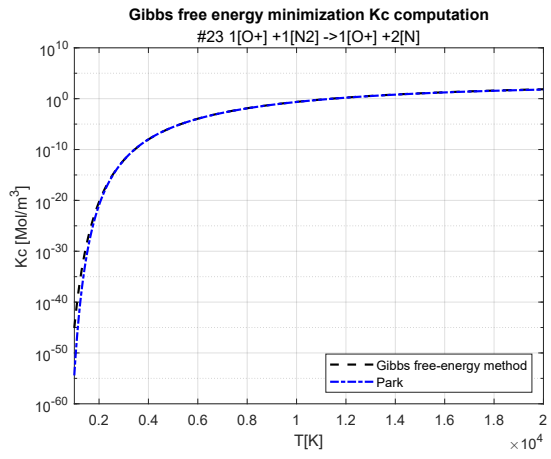
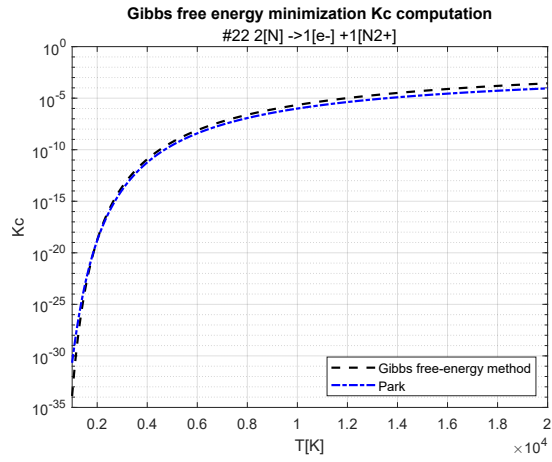
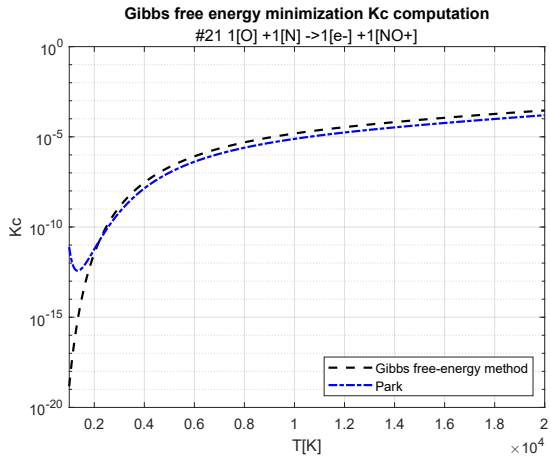
A comparison, between the K_c computed through the fitting suggested by Park and the Gibbs free-energy minimization has been carried out. In addition, the values of the constants obtained from the CFD simulations on STAR-CCM+ are also shown for several reactions. In general, the curves of $K_c(T)$ present the same trend.











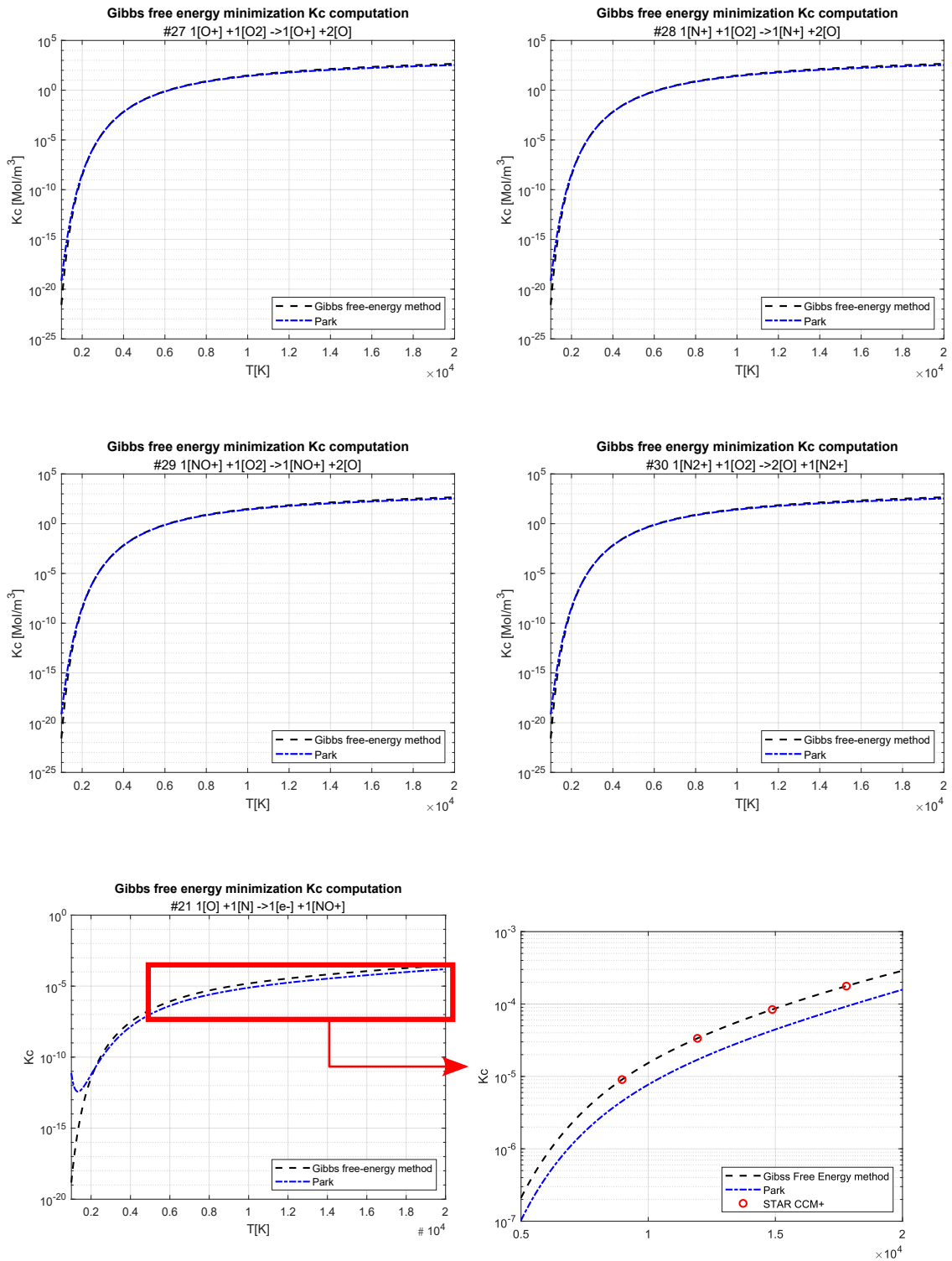


Figure 4.24: NO^+ ionization detailed comparison between Park and Gibbs method

4.5.1 Low Temperature

However, for several reactions at low temperatures ($T < 1000K$), the the curves do not show a matching trend. In STAR-CCM+ implementation the differences between the two models can be overcome. On the commercial software, it is possible to set a *Minimum Temperature for Reactions*. At low temperatures thermochemistry, in engineering cases, does not occur. Setting the *Minimum Temperature for Reactions* parameter at $1000K$ the problem is solved and there is no loss of accuracy in the results.

4.5.2 NO ionization

The ionization reaction of NO is the only one with relevant discrepancies. Between Park and Gibbs free-energy method at high and low temperature there are some differences, figure 4.24. At low temperatures, for Park model, the $K_c(T)$ curve is no longer monotonous. Such a trend is not in line with what is expected from the physics of the phenomenon. The curve obtained by the Gibbs free-energy method appears to be monotonic, with a monotonous trend even at low temperatures. The curves predicted by the two models are always overlapped, with the only exception of NO ionization. In this case, one of the limitations of Park's model becomes visible. Park's model uses a single function with 5 parameters to approximate the equilibrium constant K_c up to $32000K$. The advantage of this model is that it is computationally not expensive to apply. For each reaction, the 5 coefficients are known and the calculation of the equilibrium constant is straightforward. The Gibbs free energy model implemented in this case is more complex, as there are many more input parameters. As presented in appendix A, each chemical species is associated with 9 coefficients for each of the 3 temperature ranges considered. This means a total of 27 coefficients for each chemical species. Using the NASA polynomials (appendix A) the Gibbs free energy is calculated. From this the equilibrium constant is obtained through several steps (appendix B). The advantage of the Gibbs free energy method is greater accuracy. In fact, by dividing the temperature range into different intervals it is possible to change and adapt the coefficients to the experimental data in the best way. However, it is more complicated and expensive from a computational point of view. Park's model is still reliable when studying high-temperature phenomena. In fact, there are discrepancies limited to the ionisation of NO only, which decreases with increasing temperature.

Chapter 5

Two Temperatures Model

5.1 Introduction

This chapter represents the heart of this whole thesis. The purposes of this section are many. To begin, a two-temperature thermochemical model is briefly introduced and then it is explained why it is necessary. The chapter proceeds with a study aimed at validating the code and model developed up to this point. Two test cases of thermochemical relaxation over time are performed. These are the *N2 bath* and a *5 species air model*. These same test cases have been performed by Maier et al. [14] at Stanford University. Afterward, it is evaluated the ability of STAR-CCM+ to realise thermochemistry. In particular, the focus is on the capability to correctly calculate the transient, visualise the evolution of the two temperatures and the species in the mixture. At this stage, the limitations of the commercial code to correctly solve the thermochemistry are evident. The next step is to adapt the Matlab code to handle the vibrational and roto-translational temperatures separately. In the final part, the test cases have been carried out and the results have been compared with those presented in [14].

5.2 Two Temperature model and time relaxation

The 2 temperature model is more complicated than a single temperature model. In this case, the two temperatures are

- T: translational-rotational temperature [K]
- T^v : vibrational temperature [K]

translation and rotation are always assumed to be in equilibrium. In this chapter relaxation over time is studied:

$$\frac{\partial \rho_i}{\partial t} = \Omega_i^{ch} \tag{5.2.1}$$

$$\frac{\partial \rho e_i^v}{\partial t} = \Omega_i^{vib} \quad (5.2.2)$$

where the terms Ω^{ch} and Ω_{vib} have been discussed in 2. There is no variation of total energy and mass in time:

$$\frac{\partial E}{\partial t} = 0 \quad (5.2.3)$$

$$\frac{\partial \rho}{\partial t} = 0 \quad (5.2.4)$$

Considering E the total energy:

$$\begin{aligned} E = \rho e &= \rho(e_{tr} + e_v + e_e + h_{for}) = \rho \left(\sum x_i e_i^{tr} + \sum x_i e_i^v + \sum x_i h_i^f \right) = \\ &= \rho \left(\sum x_i \frac{L_i}{2} \frac{\mathcal{R}}{\mathcal{M}_i} T + \sum x_i e_i^v + \sum x_i h_i^f \right) \end{aligned}$$

The electronic energy e_e is considered negligible. It is possible to extract temperature as a function of vibrational energy, enthalpy of formation and composition:

$$T = \left(\frac{E}{\rho} - \sum x_i e_i^v - \sum x_i h_i^f \right) \frac{1}{\sum x_i \frac{L_i}{2} \frac{\mathcal{R}}{\mathcal{M}_i}} \quad (5.2.5)$$

In the code, normalised quantities are used. Here r indicates a reference quantity.

$$\begin{aligned} \bar{E} &= \frac{E}{\rho_r e_r} = \frac{\rho}{\rho_r} \frac{\sum x_i \frac{L_i}{2} \frac{\mathcal{R}}{\mathcal{M}_i} T + \sum x_i e_i^v + \sum x_i h_i^f}{e_r} \\ \bar{E} &= \bar{\rho} \left[\frac{\sum q_i \frac{L_i}{2} \mathcal{R} T}{\left(\sum q_i \frac{L_i}{2} \mathcal{R} T \right)_r} + \sum x_i \bar{e}_i^v + \sum x_i \bar{h}_i^f \right] \end{aligned}$$

where:

$$\begin{aligned} \bar{e}_i^v &= \frac{e_i^v}{e_r} \\ \bar{h}_i^f &= \frac{h_i^f}{e_r} \end{aligned}$$

$$\bar{E} = \bar{\rho} \left[\frac{\sum q_i \frac{L_i}{2}}{\left(\sum q_i \frac{L_i}{2} \right)_r} \bar{T} + \sum x_i \bar{e}_i^v + \sum x_i \bar{h}_i^f \right]$$

$$T = \left[\frac{\bar{E}}{\rho} - \sum x_i \bar{e}_i^v - \sum x_i \bar{h}_i^f \right] \frac{\left(\sum q_i \frac{L_i}{2} \right)_r}{\sum q_i \frac{L_i}{2}} \quad (5.2.6)$$

It is finally possible to compute the pressure:

$$\begin{aligned} p &= \rho \mathcal{R} T \sum q_i \\ p_r &= \rho_r \mathcal{R} T_r \sum q_{i,r} \\ \bar{p} &= \frac{p}{p_r} = \bar{T} \bar{\rho} \frac{\sum q_i}{\sum q_{i,r}} \end{aligned}$$

The Matlab code has been adapted to manage the two temperatures. In the calculation of the forward coefficient rate k_f using the Arrhenius law, the temperature has been changed. According to [26] the reaction control temperature is the geometric average of the vibrational and translational energy:

$$\begin{aligned} T_r &= \sqrt{TT^v} \\ k_f &= c_1 T_r^\alpha e^{\frac{-\varepsilon_a}{KT_r}} \end{aligned} \quad (5.2.7)$$

For the computation of Ω_i^{vib} changes have been made.

$$\Omega_i^{vib} = \rho \frac{e_i^{v,eq} - e_i^v}{\tau_i^{V-T}} \quad (5.2.8)$$

The relaxation time τ_i^{V-T} depends on temperature T . The vibrational energy in equilibrium condition $e_i^{v,eq}$ is computed using T .

Each polyatomic species has a different vibration temperature: $T_{v,is}$ during the relaxation process. So, the total vibrational internal energy can be computed as:

$$\sum_{i=1}^{N_{neq}} x_i \frac{\mathcal{R}}{\mathcal{M}_i} \frac{1}{e^{\frac{\theta_i^v}{T_i^v}} - 1} \quad (5.2.9)$$

The equation (5.2.9) involves only polyatomic species, which are the only ones with vibrational energy.

5.3 Test Cases

Here the two test cases are presented as they are performed in [14]. These are *Zero-Dimensional Thermal baths*. The zero-dimensional adiabatic thermal bath is a standard verification case, which isolates the impacts of thermal nonequilibrium and finite-rate chemistry.

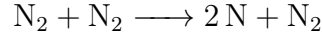
5.3.1 N2 Bath

This is the first and simplest case. It is a mixture of pure N2. The initial conditions are presented in table 5.1. The only reactions that occur in this case are the

$T_\infty[K]$	$T_\infty^v[K]$	$p_\infty[atm]$	$x[N_2]_\infty$	$x[N]_\infty$
20 000	300	27.25	1.0	0.0

Table 5.1: N_2 bath initial conditions

following nitrogen dissociation:



5.3.2 5 species air model

The second case simulates a standard 5 species air model, with initial conditions in table 5.2. This specific model and the reactions involved have been extensively discussed in 2.3.

$T_\infty[K]$	$T_\infty^v[K]$	$p_\infty[atm]$	$x[N_2]_\infty$	$x[O_2]_\infty$	$x[NO]_\infty$	$x[N]_\infty$	$x[O]_\infty$
15 000	300	20.24	0.767	0.2330	0.0	0.0	0.0

Table 5.2: 5 species air model bath initial conditions

5.4 STAR-CCM+ two temperature model

The first case, *N2 Bath*, has been simulated. This is a zero-dimensional adiabatic thermal bath. The domain is two-dimensional, a square. A 5×5 mesh with symmetry planes on each side is used, figure 5.1. Inviscid, thermal non-equilibrium and thermal non-equilibrium ideal gas models have been selected. Fully excited option as Specific Heat has been chosen for all species. The Gas Kinetics method has been selected for Vibrational-Electronic Specific Heat. An unsteady implicit time-stepping method is used for this simulation. The time step is $10^{-11}s$ with a 2nd-order temporal discretization. The time step adopted is very small and allows the thermochemical transient to be captured correctly. Subsequently, solutions with an increasingly high time step are also presented.

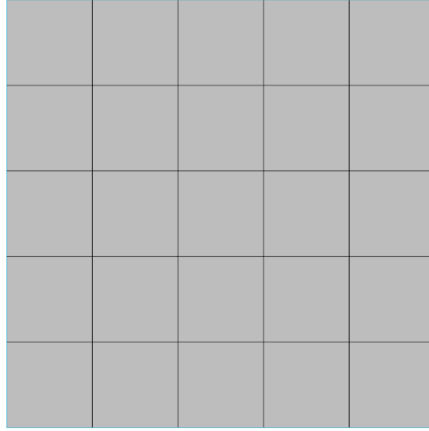
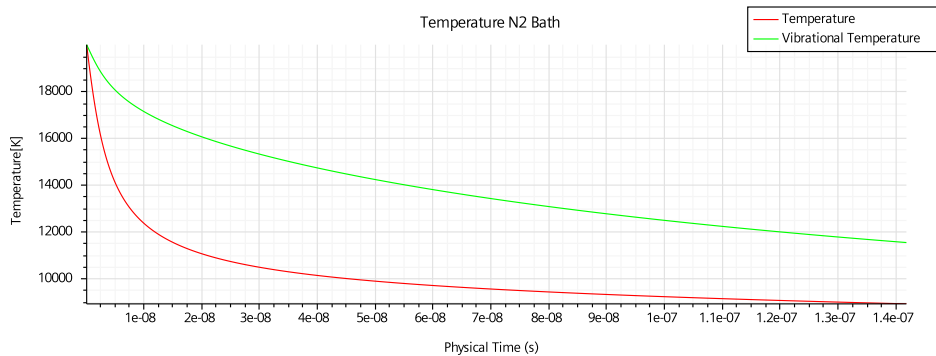


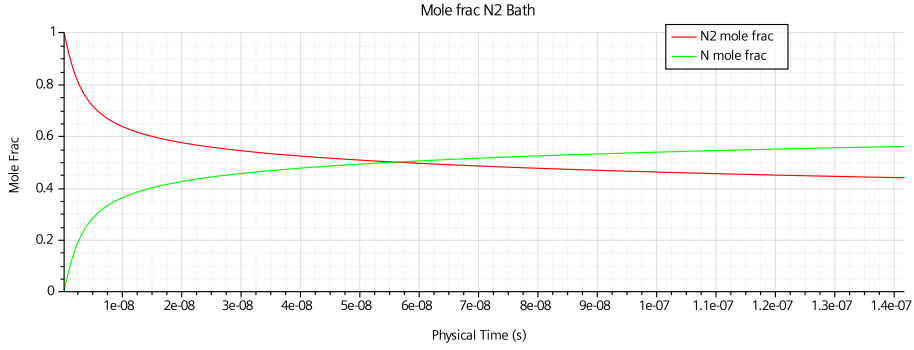
Figure 5.1: 5×5 mesh

5.4.1 N_2 Bath STAR-CCM+ results

In figure 5.2a the evolution over time of roto-translational and vibrational temperatures is shown. T decreases as expected, the dissociation of nitrogen in fact subtracts energy, it is endothermic. Also the T_v decreases, it follows the T in order to reach the equilibrium condition, figure 5.2a. Away from the collision, asymptotic conditions are reached. The temperatures, T and T_v are equivalent and the mole fractions of N and N_2 no longer change. One of the first limitations of the software is found. In this version it does not seem possible to set two different initial values for T and T^v . In figure 5.2b the evolution over time of Molar Fraction of N and N_2 is presented. Due to the effect of dissociation, the fraction of N_2 decreases and the fraction of N increases. A monotonic trend of the curves is seen. The values tend to the asymptote, the system is moving towards equilibrium conditions. The results



(a) $T(t)$ and $T^v(t)$ in N_2 bath



(b) Molar Fraction of N_2 and N in N_2 bath

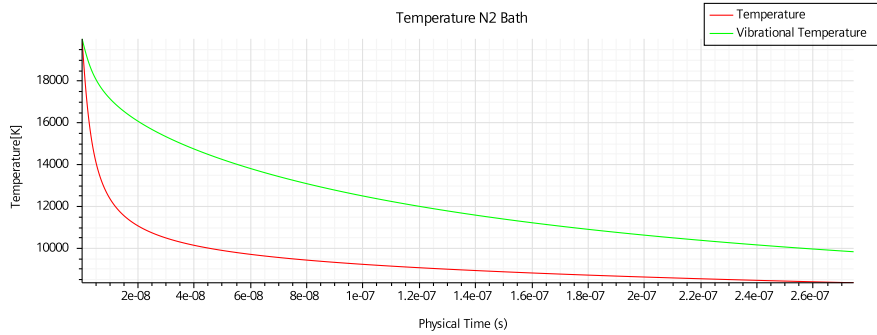
Figure 5.2: N_2 bath results, STAR-CCM+ simulation, $\Delta t = 10^{-11}s$

obtained in STAR-CCM+ are not in line with those found in [14]. However, the results obtained are consistent. The system reaches an equilibrium condition, with a greater presence of N than the one shown in [14]. In fact, there is a higher initial energy than in the test case presented by Maier et al. [14] $T_\infty = T_\infty^v = 15\,000K$.

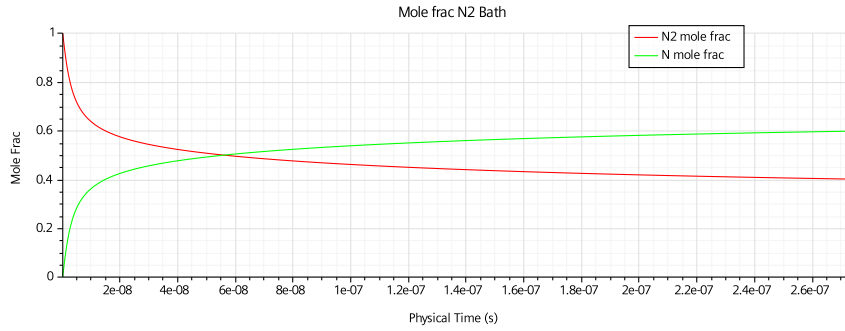
5.4.2 N_2 Bath STAR-CCM+ time step influence

It is interesting to see how the solution can be influenced by the time step adopted. In the previous analysis, an extremely small time step has been used in order to capture the transient correctly. However, many iterations are required to reach the equilibrium. Solutions with increasing time steps are presented below:

- $\Delta t = 10^{-10}s$: the transient is correctly and smoothly calculated



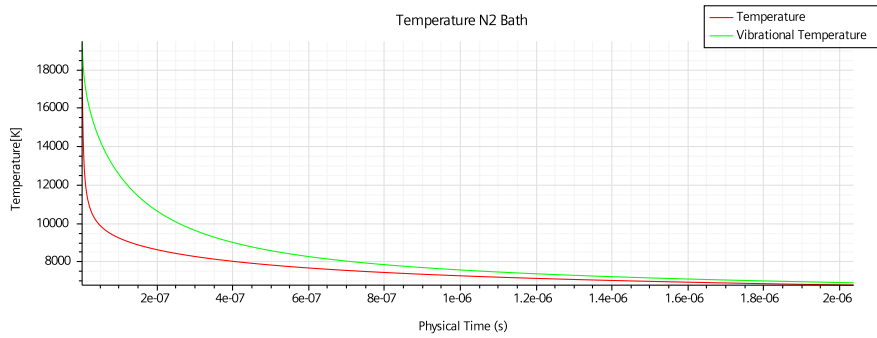
(a) $T(t)$ and $T^v(t)$ in N_2 bath



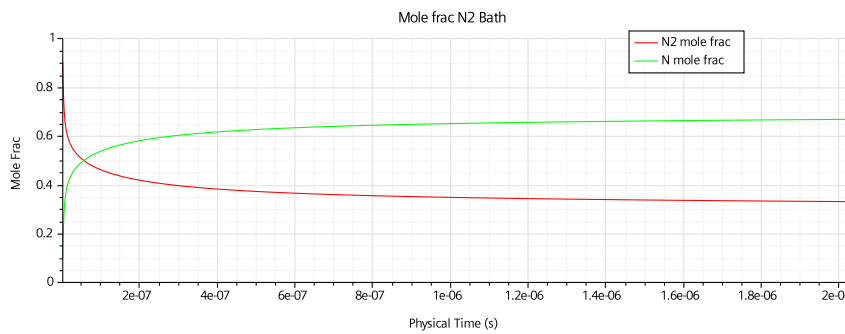
(b) Molar Fraction of N_2 and N in N_2 bath

Figure 5.3: N_2 bath results, STAR-CCM+ simulation, $\Delta t = 10^{-10}s$

- $\Delta t = 10^{-9}s$: the transient is correctly and smoothly calculated



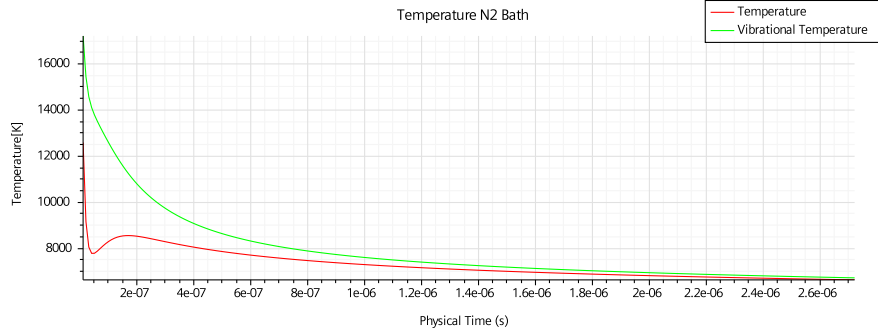
(a) $T(t)$ and $T^v(t)$ in N_2 bath



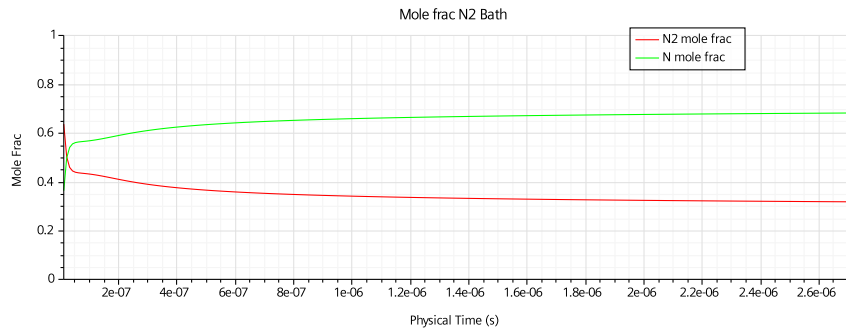
(b) Molar Fraction of N_2 and N in N_2 bath

Figure 5.4: N_2 bath results, STAR-CCM+ simulation, $\Delta t = 10^{-9}s$

- $\Delta t = 10^{-8}s$: the transient is no longer correctly calculated. The curve of T is not monotonic. The temperature drops too quickly, the calculated dissociation is greater than the actual one. The temperature then rises again to try to correct this numerical undershoot. However, this time step is still valid if the focus is only on the equilibrium conditions.



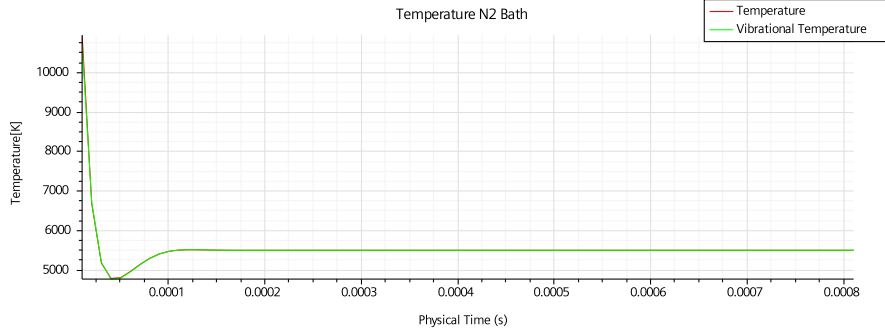
(a) $T(t)$ and $T^v(t)$ in N_2 bath



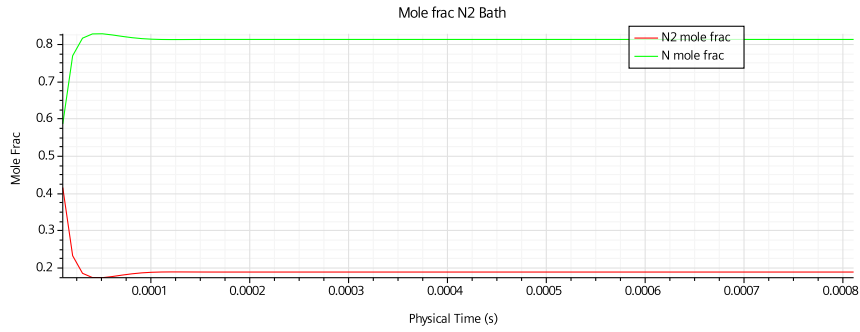
(b) Molar Fraction of N_2 and N in N_2 bath

Figure 5.5: N_2 bath results, STAR-CCM+ simulation, $\Delta t = 10^{-8}s$

- $\Delta t = 10^{-5}s$: the transient is no longer accurately calculated. The curve of T and also T_v is not monotonic.



(a) $T(t)$ and $T^v(t)$ in N_2 bath



(b) Molar Fraction of N_2 and N in N_2 bath

Figure 5.6: N_2 bath results, STAR-CCM+ simulation, $\Delta t = 10^{-5}s$

In this case the maximum time step to calculate the transient correctly is $10^{-9}s$. For larger time steps the transient is numerical and not physical. A kind of CFL condition based on reaction rates is violated.

5.5 Multiple vibration temperatures model

The forward rate for every dissociation reaction is computed using the specific T_{is}^v of the $is - th$ dissociating species. For dissociation reaction the control temperature is:

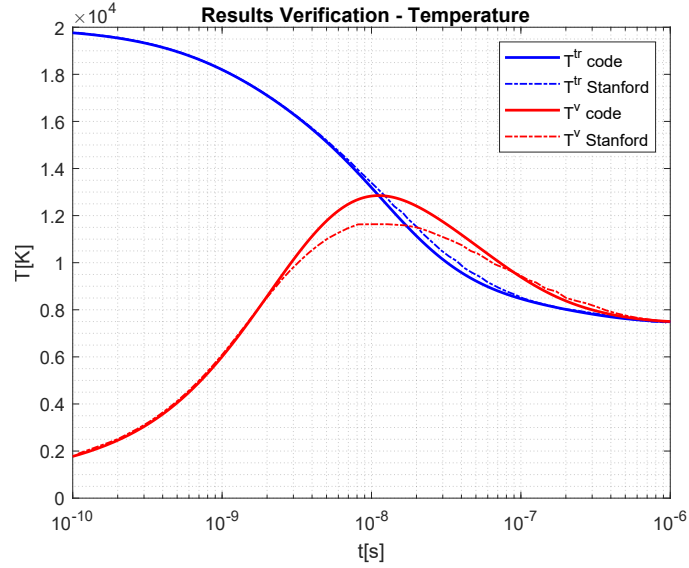
$$T_r = \sqrt{TT_{is}^v}$$

where is is the $is - th$ dissociating species. For exchange reactions the control temperature has been assumed equal to the translational-rotational temperature as prescribed in [25]

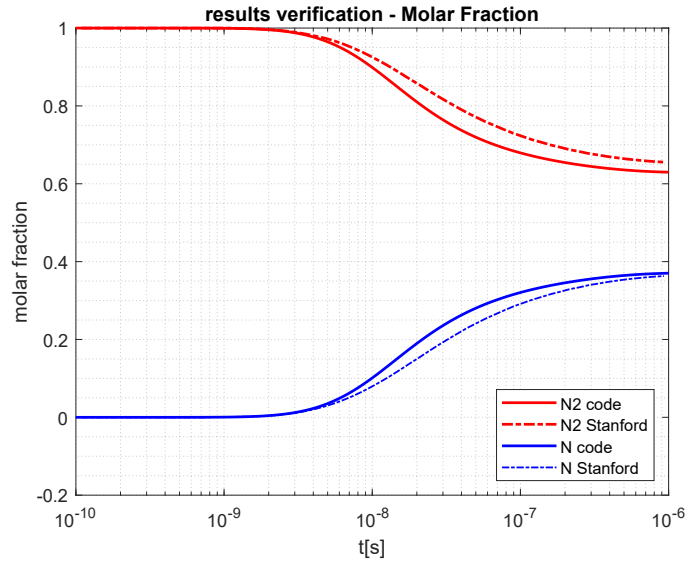
$$T_r = T$$

5.5.1 N_2 Bath results

In this first test, there is only one vibrational temperature T^v . There is only one species, N_2 , that has vibrational energy. The results of temperature relaxation and dissociation can be seen in Figure 5.7



(a) T and T^v comparison with [14] results, N_2 bath



(b) Molar fraction comparison with [14] results, N_2 bath

Figure 5.7: N_2 results and comparison with [14]

The results are in line with expectations. It can be seen that N_2 dissociates

at high temperatures to form monoatomic nitrogen. In addition, the vibrational energy at the beginning is strongly out of equilibrium. It can be seen that T^v increases rapidly while T decreases. At about 10^{-8} seconds, the T^v overtakes the T , an overshoot occurs. A final check on the consistency of the results is the fact that T and T^v tend towards a single equilibrium value of $7500K$. The results are very close to those obtained at Stanford. In particular, as far as T is concerned, the results are practically identical. There are differences in vibration temperature. The peak is reached at the same time ($10^{-8}s$) but has different values, table 5.3. There is a relative error of 6.2%. The differences found stem from the imperfect

	Stanford	Code
Peak T^v [K]	121 000	129 000

Table 5.3: Vibrational temperatures maximum values comparison, N_2 bath

extraction of data from the images on the paper. They may also be due to slightly different values of the parameters for the calculation of k_f with Arrhenius' law.

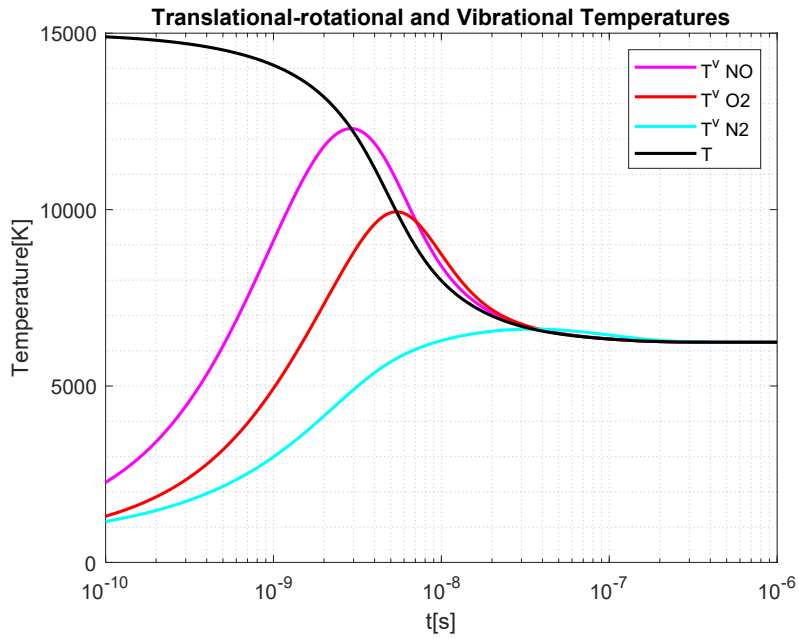
5.5.2 5 species air multiple vibration temperatures results

In figure 5.8 the results of thermochemical relaxation of the second test case are shown. In figure 5.8a the evolution of vibrational temperatures of NO , O_2 , N_2 over time is presented. The evolution of T is also shown. In this figure the results are not compared with [14]. As explained further Maier et al. [14] use a single vibrational temperature model. In figure 5.8b the variation of molar fractions of the species over time is shown. As in the previous case of the N_2 bath, the T falls and the T_i^v of each polyatomic species rises, figure 5.8a. Also in this case T and T_i^v reach the same equilibrium value of $6200K$.

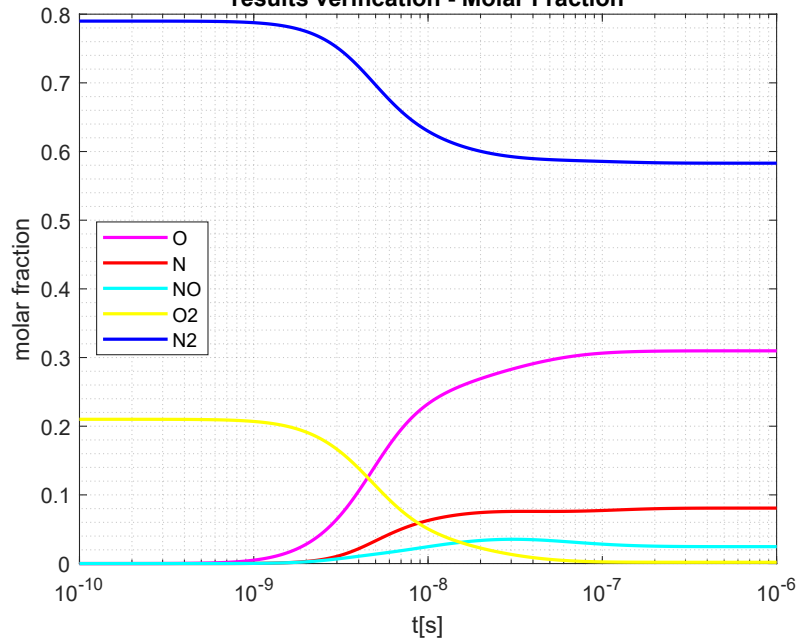
5.6 Single vibration temperature model

5.6.1 How to compute a single vibrational temperature

In Maier et al. [14] only one vibrational temperature has been used. In the equations only one vibrational temperature has been taken into account. Every species has the same T^{ve} , where ve stands for vibrational-electronic. In fact, in [14], vibrational and electronic energy are a function of the same temperature. In order to compare the results, it is therefore necessary to extract a vibration temperature from our model which is significant \hat{T}_v .



(a) T and T^v results, 5 species air
results verification - Molar Fraction



(b) Molar fraction comparison with [14] results, 5 species air

Figure 5.8: 5 species air relaxation results, multiple vibration temperatures

This value can be found by solving the following non-linear equation:

$$\sum_{i=1}^{N_{neq}} y_i \frac{\mathcal{R}}{\mathcal{M}_i} \frac{1}{\frac{\theta_i^v}{e^{\hat{T}^v} - 1}} = \sum_{i=1}^{N_{neq}} y_i \frac{\mathcal{R}}{\mathcal{M}_i} \frac{1}{\frac{\theta_i^v}{T_i^v - 1}} \quad (5.6.1)$$

To solve the equation, however, it is necessary to start from an initial guess of \hat{T}^v . For simplicity, the average of the vibrational temperatures of the species is used as the initial guess.

5.6.2 5 species air \hat{T}^v post-processing

It is possible to obtain \hat{T}^v from the multi-temperature vibrational model simply by a post-processing operation, as explained above. In the figure the trend of \hat{T}^v and T is compared with the results in [14]; there are noticeable differences. In fact, Maier et al. [14] use a simplified model, implemented in the following section. The results

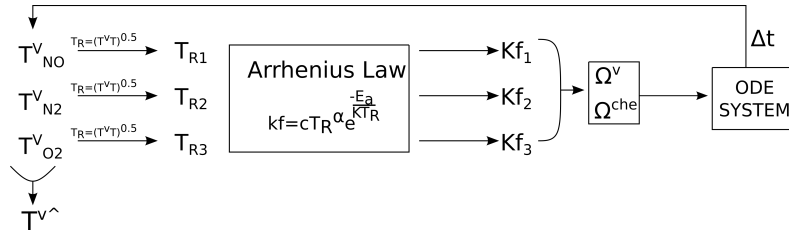


Figure 5.9: Compute \hat{T}^v as post-process

of the mole fractions do not change as the implemented thermochemical model is unchanged.

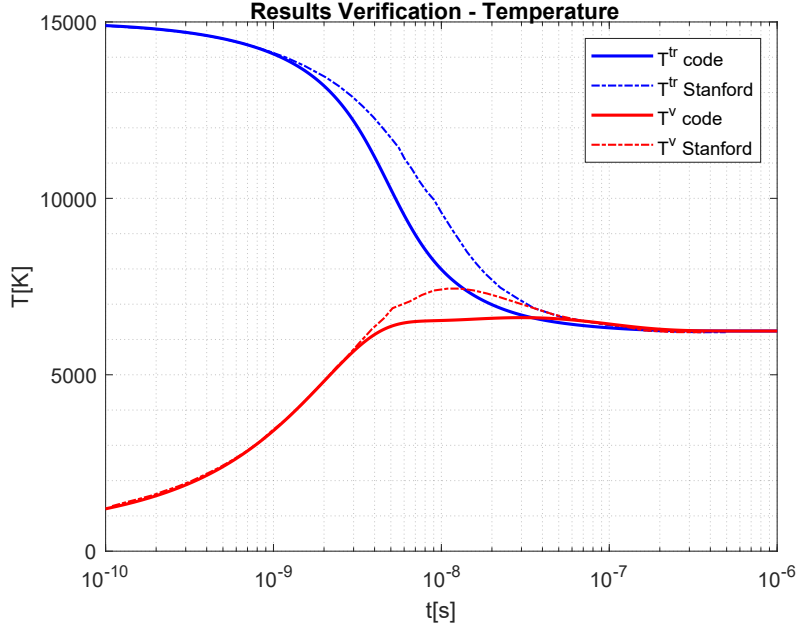


Figure 5.10: 5 species air relaxation results, \hat{T}^v as post-process

5.6.3 Approximations in the thermochemical model

In Maier et al. [14] only one vibrational temperature has been used and this leads to approximations in the thermochemical model and results. There is only one control temperature for every dissociation reactions:

$$T_r = \sqrt{T\hat{T}^v}$$

This procedure is not precise but approximate. It does not take into account the

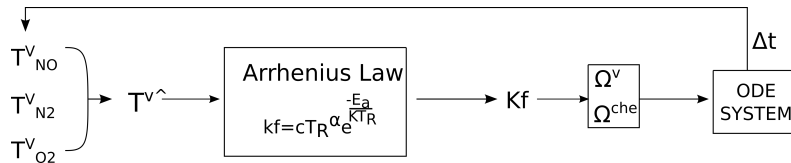
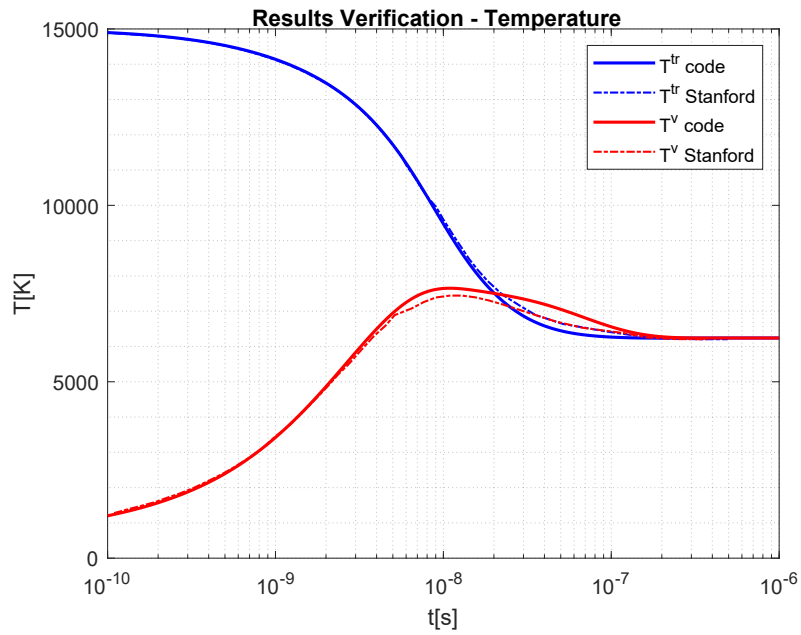
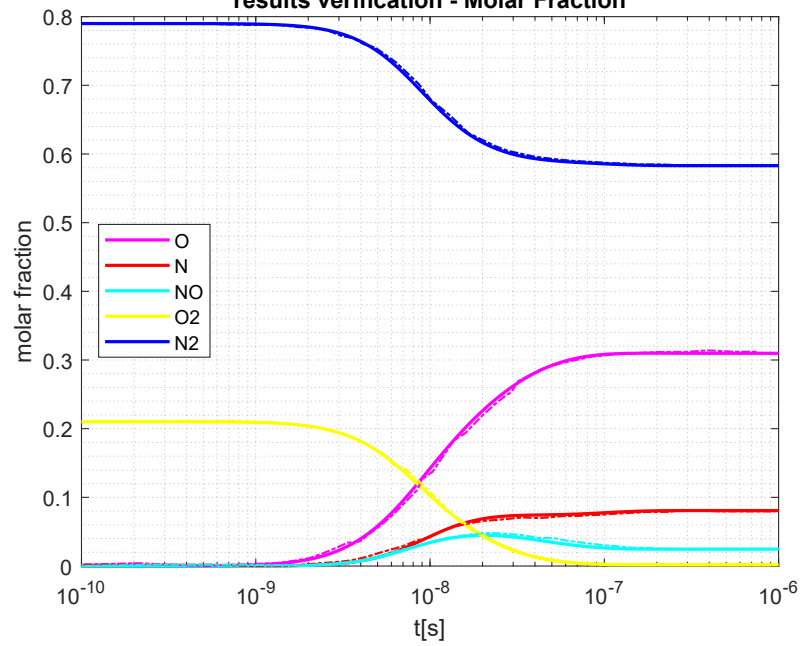


Figure 5.11: Compute \hat{T}^v and use it to compute T_r

fact that each species at a specific time has a different vibration temperature. By introducing this approximation into the model and solving the 5-species air test case the results are presented in figure 5.12. In figure 5.12 the error, despite inaccuracy in data extraction, is basically zero.



(a) T and T^v results, 5 species air
results verification - Molar Fraction



(b) Molar fraction comparison with [14] results, 5 species air

Figure 5.12: 5 species air relaxation results, Single vibration temperature model

5.7 Conclusion and considerations

The limitations of STAR-CCM+ in calculating the vibration temperature are made

evident. The results obtained with the MATLAB code are in line with what is expected and have a physically valid meaning. Thanks to the comparison with the values found by Maier et al. [14] it can be seen that they are correct and accurate. The code developed is more advanced than those adopted in [14]. It is in fact possible to use a different control temperature T_r for each reaction. This depends on the species involved in the reaction and on their vibrational energy.

Chapter 6

Non-Equilibrium in STAR-CCM+

6.1 Introduction

The purpose of this chapter is to test the different options and models available in STAR-CCM+ for thermochemistry. In particular how to handle vibrational relaxation. Along with this, there is a focus on how electronic energy is modelled. It is the first approach to the analysis of the non-equilibrium process in STAR-CCM+. The examination uses the N_2 Bath test case presented in the previous chapter. Then the flow-field around the experimental RAM-C aircraft is studied. This analysis is still inviscid and uses a simple ideal gas model. Finally, the most complex case studied is that of the HEG, where a laminar model is implemented.

6.2 STAR-CCM+ Models

6.2.1 Specific Heat

In STAR-CCM+ the global specific heat of each element consists of four different contributions: translational, rotational, vibrational and electronic.

$$C_{p,tot} = C_{p,t} + C_{v,r} + C_{v,v} + C_{v,e} \quad (6.2.1)$$

The value of each term is evaluated on the associated partition function Q_i

$$\frac{e_i}{\mathcal{R}} = T^2 \frac{\partial}{\partial T} \ln(Q_i) \quad (6.2.2)$$

$$\frac{C_{v,i}}{\mathcal{R}} = \frac{T^2}{Q_i} \left[\frac{\partial^2 Q_i}{\partial T^2} + \left(\frac{\partial Q_i}{\partial T} \right)^2 + \frac{2\partial Q_i}{T\partial T} \right] \quad (6.2.3)$$

The contribution of $C_{p,t}$ is effectively constant because of the small spacing between quantum energy levels. The rotational energy is assumed as fully excited. The gaps between quantum energy levels are negligible. These two contributions can be considered as a single constant value: $C_{p,tr}$. The partition function for vibrational and electronic energy is:

$$Q_v = \prod_i (1 - e^{-\theta_i/T})^{-g_i} \quad (6.2.4)$$

$$Q_e = \sum_i g_i e^{-\theta_i/T} \quad (6.2.5)$$

where θ_i is the characteristic temperature and g_i is degeneracy. Degeneracies and characteristic temperatures can be found for various molecules.

6.2.2 Reaction Coefficient

The forward reaction coefficient is computed using Arrhenius Law. The reverse reaction is computed using the equilibrium constant. This procedure is an approximation. In fact the relation $K_c = \frac{k_f}{k_b}$ is verified only at the equilibrium.

6.2.3 Mode Relaxation Time

This node is available only for polyatomic species.

Landau-Teller Relaxation Time

In the Landau-Teller the relaxation time is

$$\tau = \frac{A}{p} e^{\left(\frac{B}{T}\right)^{1/3}} \quad (6.2.6)$$

The default values proposed by the software are:

$$A = 7.21434 \cdot 10^{-4} \text{ Pa s}$$

$$B = 1910000 \text{ K}$$

The values are consistent with those in [15]

Multi-Component Relaxation Time

This model is more complex. The vibrational relaxation rates are more accurate at high temperatures. The rates are limited due to the finiteness of the elastic collision

cross-sections. This can be done by adding the time for the elastic collisions to the vibrational relaxation time. The τ_v is expressed in the form:

$$p\tau_v = e^{a(T^{-1/3}-b)} - 18.421 atm \quad (6.2.7)$$

where a, b are parameters that depend on the colliding couple of molecules. This is the Millikan-White model. It has been improved by Park. The correction involves time for the elastic collisions to the vibrational relaxation.

$$\tau = \tau_v + \left[n\sqrt{(8kT/\pi m)\sigma_v} \right]^{-1} \quad (6.2.8)$$

where n , and m are the total number of colliding particles and the average mass of the mixture.

$$\sigma_v = \sigma'_v(50.000/T)^2 \text{ cm}^2 \quad (6.2.9)$$

The value of σ'_v is estimated to be $3 \cdot 10^{-21} m^2$. The default value proposed by STAR-CCM+ is $10^{-20} m^2$;

6.3 N2 Bath Inviscid

The N2 bath inviscid simulation has been used as a test case, freestream conditions in table 6.1

$T_\infty[K]$	$T_\infty^v[K]$	$p_\infty[atm]$	$x[N_2]_\infty$	$x[N]_\infty$
20 000	20 000	27.25	1.0	0.0

Table 6.1: N_2 bath initial conditions STAR-CCM+

The aim is to highlight and justify differences between different relaxation time models. The different models that have been tested are:

Landau-Teller, in N_2 *material properties*

MWP1 (Millikan-White-Park): Multicomponent Relaxation Time, with Park correction Cross-Section: $10^{-20} m^2$ default value, in N_2 *material properties*

MWP2 (Millikan-White-Park): Multicomponent Relaxation Time, with Park correction Cross-Section: $3 \cdot 10^{-21} m^2$, in N_2 *material properties*

It is possible to set *Mode relaxation time* in *Gas components > Material Properties*. It has been set as *Inverse Mole-Fraction Average*. It can be set as *Landau-Teller* and the node of *Mode relaxation time* under N_2 disappears. In this case, the result is the same as selecting *Landau-Teller* under N_2 . Figure 6.1 shows the results of the three different models.

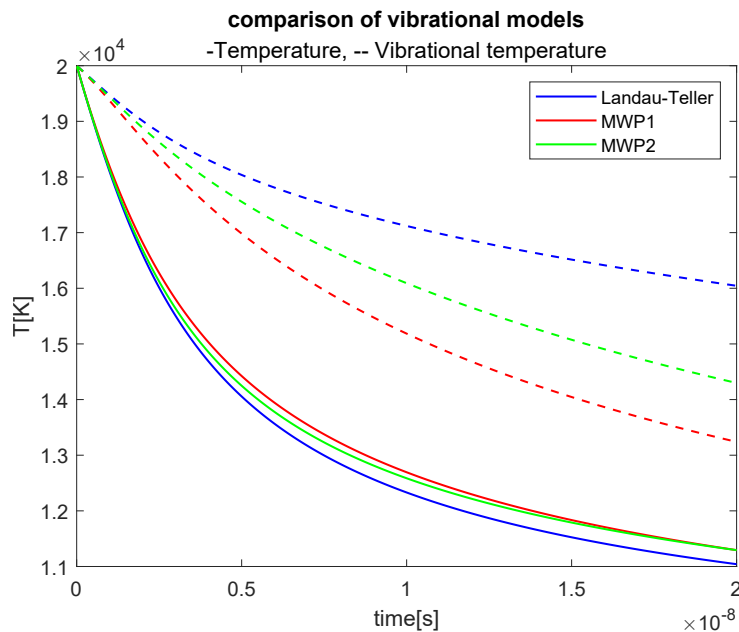


Figure 6.1: Comparison of Landau-Teller and Millikan-White-Park relaxation time correlation

In figure 6.1, the relaxation of the roto-translational temperature is similar in every model. The greatest difference lies in the relaxation of the vibrational temperatures. In the Landau-Teller model, the relaxation vibrational temperature is significantly slower than in the Millikan-White-Park.

6.3.1 STAR-CCM+ models comparison

STAR-CCM+ provides two different models for calculating the relaxation time. However, both models only cover vibrational relaxation. The software also provides the option of adjusting the electronic energy of the species. However, it is not possible to see how this evolves over time. In figure 6.1, it can be seen that the models give different values for the evolution of the vibrational temperature. The inequality lies in the different values of the relaxation times. For the Landau-Teller model, the relaxation is slower than for the Millikan-White-Park model. Two different values of σ'_v have been tested. The first one is the default value proposed by STAR, the second by Park et al. [24].

6.3.2 STAR-CCM+ and MATLAB code relaxation comparison

It is not possible to use Maier et al. [14] as a comparison case because the starting conditions are different. In fact, as mentioned in the previous chapter, STAR-CCM+ does not allow to set a different initial value for the roto-translational and vibrational energy. The MATLAB code, validated in the previous chapter, is used as a comparison to evaluate the results produced by STAR-CCM+. It is evident

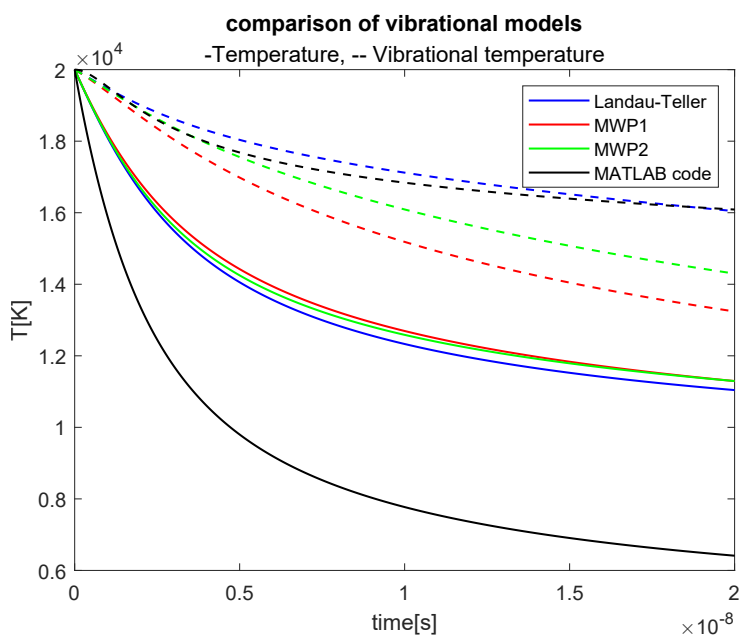


Figure 6.2: Comparison of STAR-CCM+ and the MATLAB code relaxation of N₂ Bath, temperatures

that temperature relaxation is significantly slower on STAR-CCM+, figure 6.2. By contrast, the vibrational temperature relaxation is in line with the results produced by the MATLAB code. The temperature drops faster in the MATLAB simulation. This is justified by the fact that N₂ dissociates faster than the STAR-CCM+ result, figure 6.3.

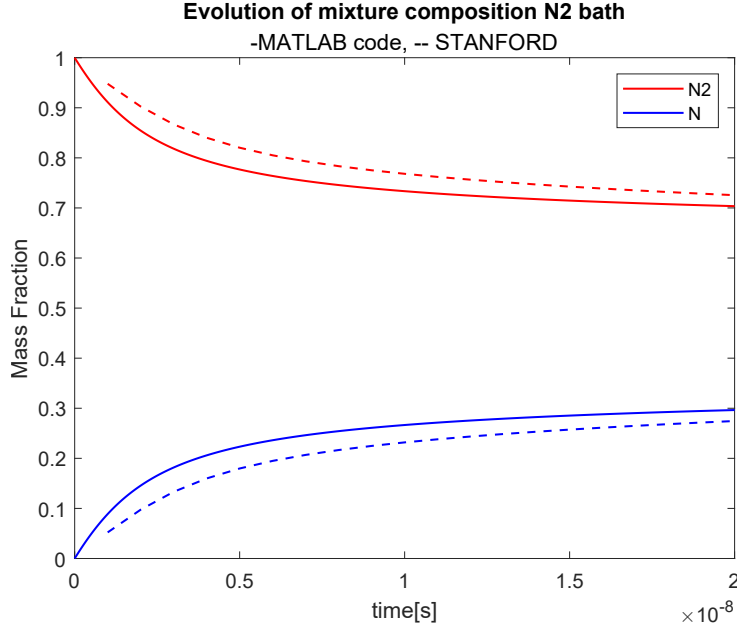


Figure 6.3: Comparison of STAR-CCM+ and the MATLAB code relaxation of N2 Bath, mass fraction

6.4 RAM-C II

The RAM-C II is a test vehicle. It has a blunted nose and is has been used to analyse the effect of the plasma formation on radio communication during the re-entry. It has a radius of 0.1524 m and a cone angle of 9° . For years it has been used as a common verification and validation test for weakly-ionized flows. A 7 species air model has been used. There are N_2 , O_2 , N , O , NO , NO^+ , e^- and viscous effects are not considered. The freestream conditions are those listed in the table 6.2. It has been used the *ideal gas* model. The reactions have been imported

M_∞	$p_\infty [Pa]$	$\rho_\infty [kg\ m^{-3}]$	$T_\infty [K]$	$y[N_2]_\infty$	$y[O_2]_\infty$
23.9	19.7	$2.7024 \cdot 10^{-4}$	254	0.767	0.233

Table 6.2: RAM-C freestream conditions

through CHEMKIN files and the properties of chemical species described through NASA polynomials, appendix A. It has been used a structured mesh with 15 000 elements, figure 6.4. A constant $CFL = 0.5$ has been used to avoid numerical instabilities. The analysis is in $2D$ and axisymmetric. The simulation was run for 20 000 iterations.

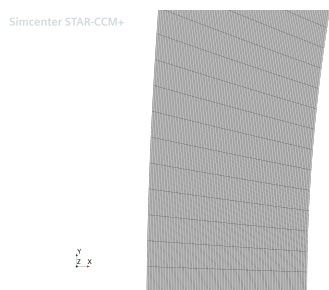
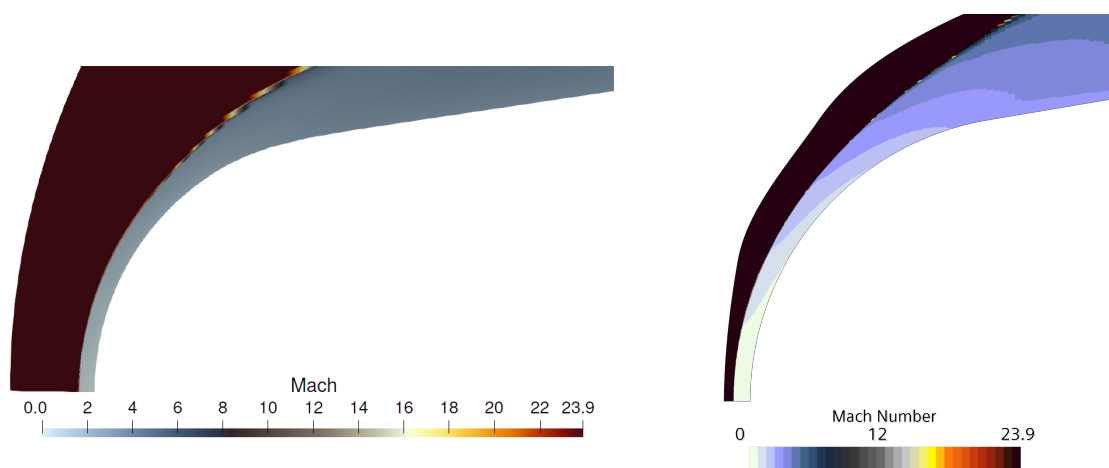


Figure 6.4: Mesh detail close to the nose

6.4.1 Mach and electron density



(a) Mach number, RAMC case, numeric results [14]

(b) Mach number, RAM-C case

Figure 6.5: Mach number, RAM-C case, comparison with numeric results [14]

Figure 6.5 shows the Mach number of the flow-field around the RAM-C. While, figure 6.6 shows the electron density of the flow-field around the RAM-C. Both, the Mach number and the electron density, are compared with the results computed by Maier et al. [14]. From the Mach number comparison it is clear that the speed ranges are coincident. The electronic density distribution is also almost equivalent. However, the maximum value found on STAR-CM+ is $14 \cdot 10^{-11} \text{ kg m}^{-3}$ versus $12 \cdot 10^{-11} \text{ kg m}^{-3}$ in [14]. The electron density is highest at the stagnation line, where the shock is strongest. Using a 7 species air model allows to predict the formation of plasma in the proximity of the vehicle. The model takes into account two ionized particle: NO^+ and e^- . To achieve better results, more complex chemistry models can be adopted. However, in this case of flight, 7 species are enough to reconstruct the mechanism of ion formation. NO^+ is produced due to

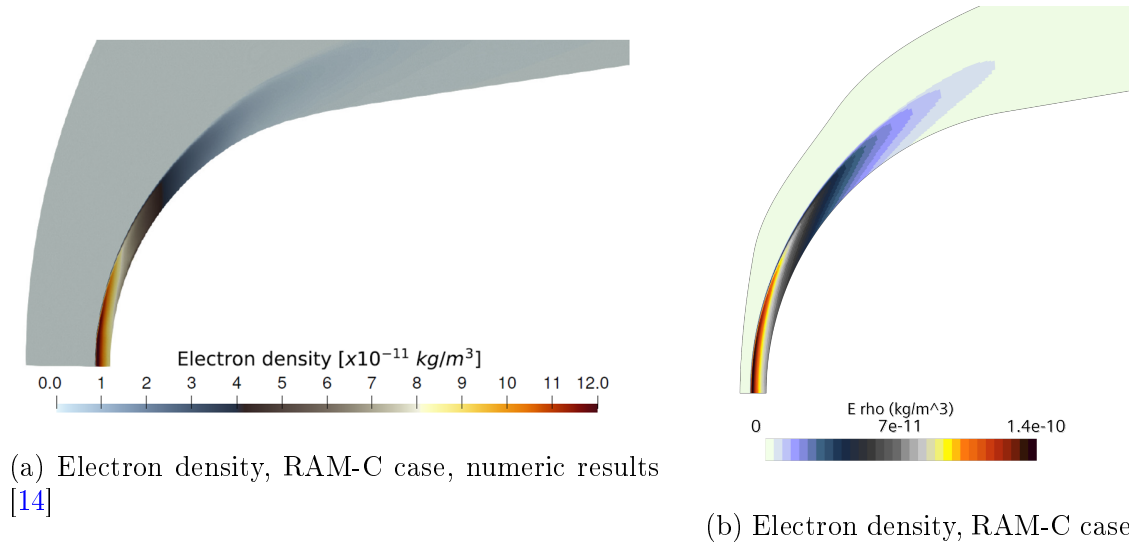
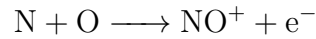


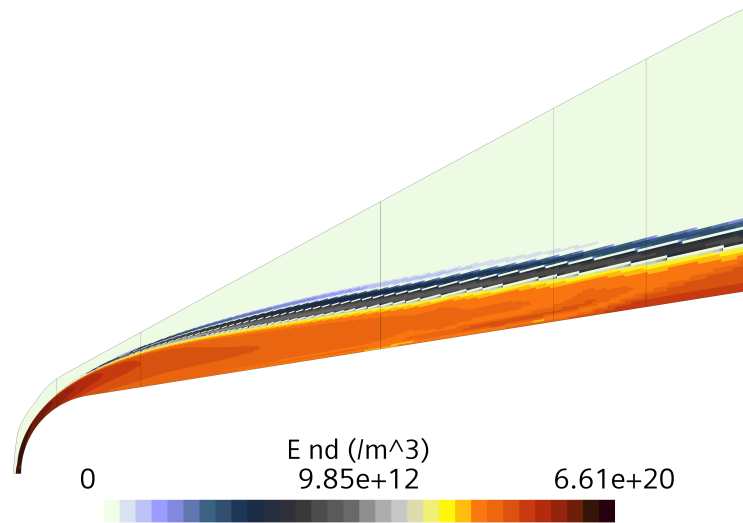
Figure 6.6: Electron density, RAM-C case, comparison with numeric results [14]

dissociative recombination of mono-atomic nitrogen and oxygen:

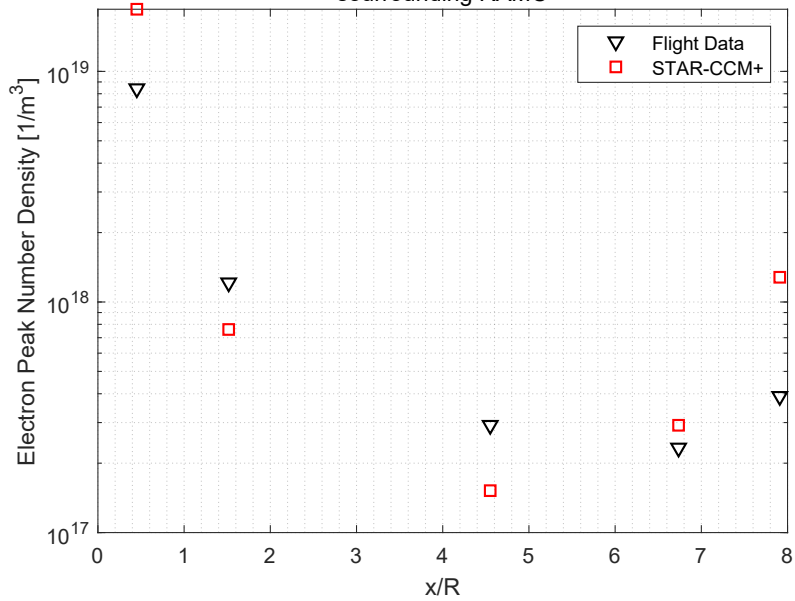


6.4.2 Electron number density

Figure 6.7 shows a plot of maximum electron number density in the axis-normal direction, compared to other numerical results as well as experimental measurements. The experimental measurements of electron density were collected along the axial length of the vehicle using reflectometers and an electrostatic rake. The CFD simulation results are in line with the experimental and numerical results proposed by [5]. Differences due to a lack of chemical-vibrational coupling in STAR-CM+ are evident.



(a) Electron number density, RAM-C
Electron Peak Number Density
 surrounding RAMC



(b) Electron peak number density, RAM-C, comparison with flight data

Figure 6.7: Electron number density, RAM-C

6.4.3 Mass Fraction along stagnation line

Figure 6.8 shows the species mass fraction along stagnation line through the normal shock. In figure 6.5b a strong bow shock that surround the vehicle is observed. High

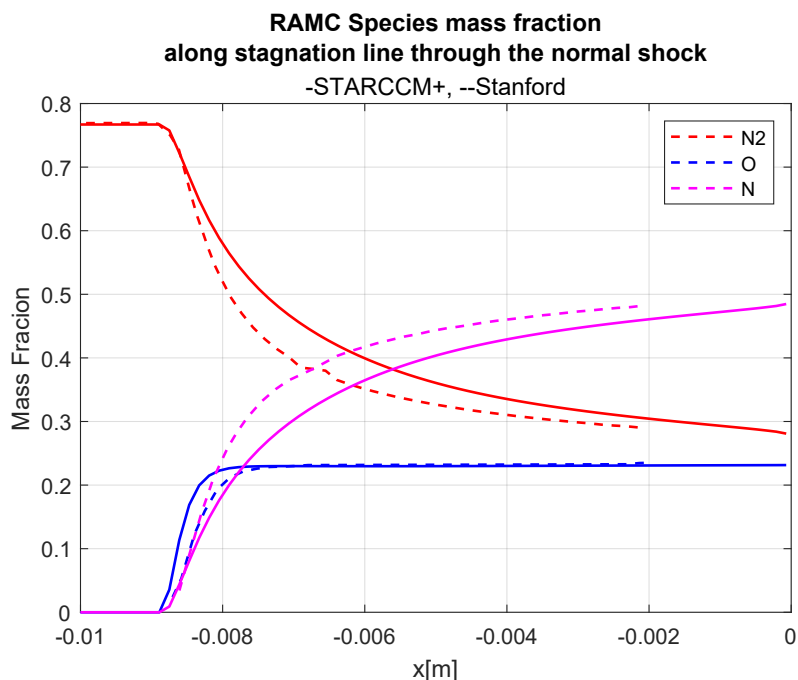


Figure 6.8: RAM-C species concentrations. Comparison with numerical [14]

temperatures across the shock lead to chemical reactions, resulting in significant variations in the flow chemistry along the stagnation line, as illustrated in figure 6.8. N_2 and O_2 mass fractions fall after the shock, while concentrations of N and O increase. The mass fraction of the other chemical species is negligible in comparison. Temperatures are sufficient to provoke ionization, even so, the resulting concentrations of NO^+ and e^- are orders of magnitude smaller than the neutral species. However, there are some differences in the evolution of species concentrations after the shock. This could be caused by the fact that the relaxation of the vibrational energy of O_2 and N_2 which is not considered. In this case STAR-CCM+ and Maier et al. [14] use two different models. In the Maier et al. model N_2 is visibly moving faster towards equilibrium conditions. This happens because translation and rotation are assumed to be in equilibrium immediately after the shock and vibrational energy is the only one that has to relax. On STAR-CCM+, on the other hand, there is a single temperature representing the internal energy.

6.5 HEG Cylinder

The experiments in the High-Enthalpy shock tunnel in Gottingen (HEG) are frequently used to validate thermochemical models in CFD analysis. The results are compared with the numeric result obtained by Maier et al. [14] and experimental results. The flow in analysis, develops around a cylinder with a radius of $45mm$

with the free-stream conditions set as in table 6.3. A 5 species air model has been used (N_2 , O_2 , N , O , NO). Viscous effects have been considered, the *laminar* model has been selected. The reactions have been imported through CHEMKIN files and the properties of chemical species described through NASA polynomials, appendix A. On the cylinder there is a fixed temperature of 300K.

M_∞	$p_\infty [Pa]$	$\rho_\infty [kg\ m^{-3}]$	$T_\infty [K]$	$y[N_2]_\infty$	$y[O_2]_\infty$	$y[NO]_\infty$	$y[N]_\infty$	$y[O]_\infty$
8.98	476	$1.547 \cdot 10^{-3}$	901	0.7543	0.00713	0.01026	$6.5 \cdot 10^{-7}$	0.2283

Table 6.3: HEG freestream conditions

6.5.1 Ideal Gas

In this first analysis the *ideal gas* model has been selected. This module does not activate the vibrational temperature field function. However, since the thermodynamic properties have been passed through the NASA polynomials, these depend on temperature. The model in this case does not use the vibrational temperature to calculate the energy of the molecules, but only the roto-translational temperature. The result should still be reliable, since it is the c_v that is responsible for absorbing the vibrational effects, as explained at the beginning of this chapter. The *Mathur-Saxena Averaging* method has been selected for both the dynamic viscosity and the thermal conductivity, as suggested in [7]. A structured mesh with 10 500 elements has been used.

Pressure

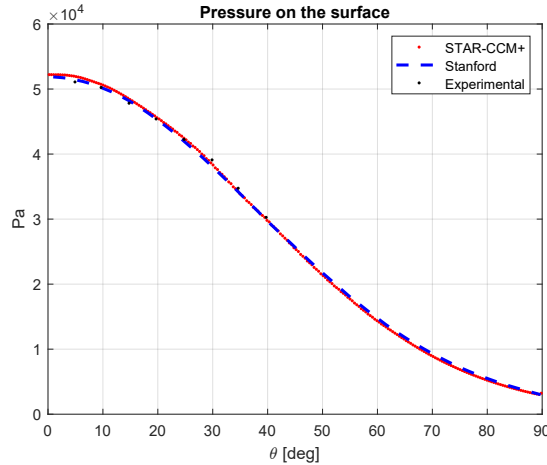


Figure 6.9: Pressure distribution, ideal gas, HEG case. Comparison with numerical and experimental results [14]

The pressure trend around the cylinder, in figure 6.9 is perfectly in line with the experimental and numerical results.

Heat Flux

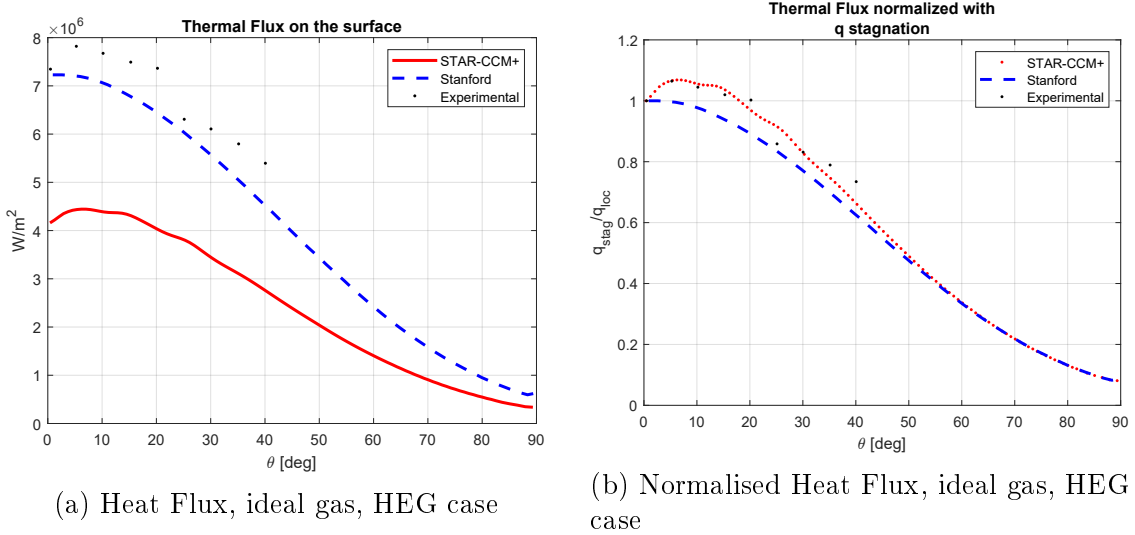


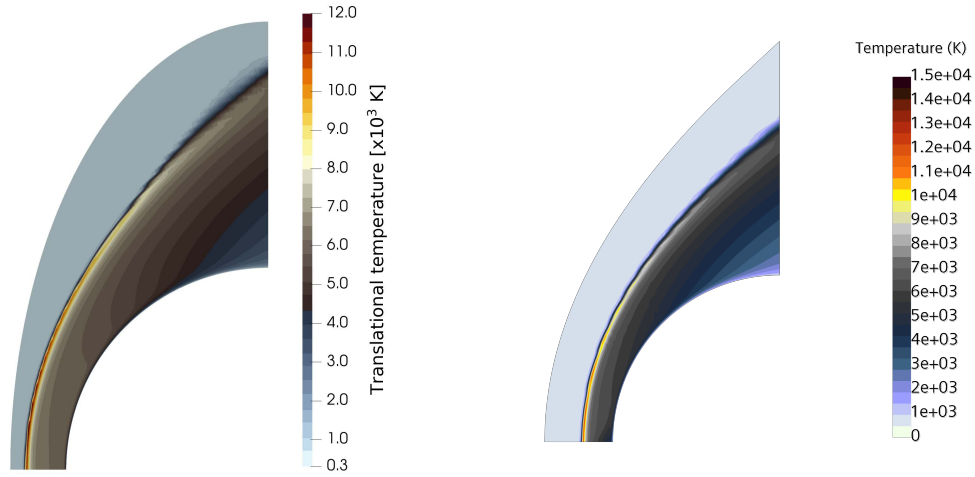
Figure 6.10: Heat Flux, ideal gas, HEG case. Comparison with numerical and experimental results [14]

Figure 6.10a reports the heat flux computed in STAR-CCM+ in comparison with experimental data and numerical results from [14]. As can be seen from 6.10a, the heat flow is not calculated correctly. The results are underestimated. The heat flux found is about half of the expected one. However, figure 6.10b shows that the heat flux normalised compared to the heat flux at the stagnation point. In this case, the results are in line with the numerical and experimental results. In conclusion, the found heat flux trend is perfect, but it needs to be rescaled.

6.5.2 Thermal Non-Equilibrium

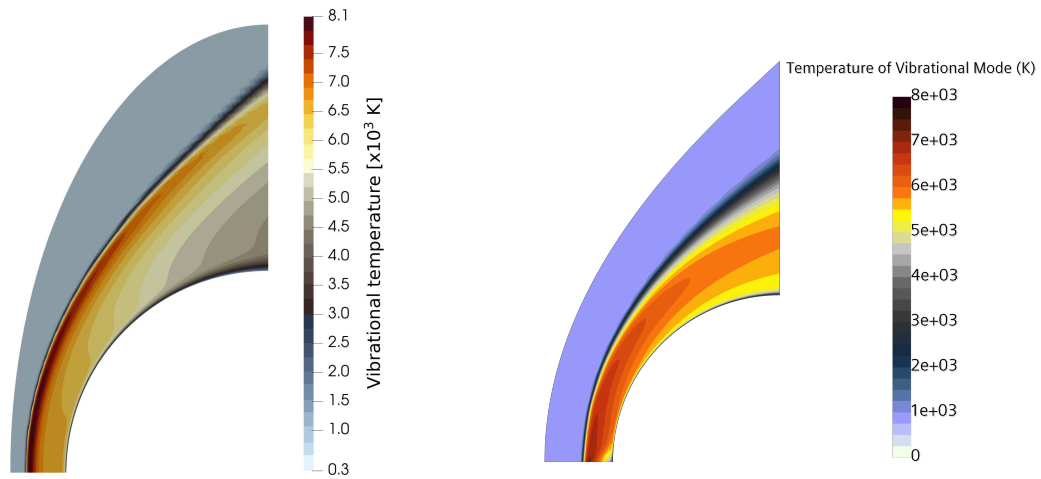
In this second analysis the *Thermal Non-Equilibrium* model has been selected. A structured mesh with 22 000 elements has been used. This module activates the vibrational temperature field function. The *Fully-Excited* option for specific heat has been selected. So, translational and rotational energy are considered to be fully excited, since the gap between quantum energy levels is negligible. The *Mathur-Saxena Averaging* method has been selected for both dynamic viscosity and thermal conductivity, as suggested in [7]. The pressure graph is the same as that found with the ideal gas model, figure 6.9.

Temperature



(a) Roto-translational temperature, Maier et al. results, HEG case (b) Roto-translational temperature, HEG case

Figure 6.11: Roto-translational temperature, Thermal Non-Equilibrium gas, comparison with Maier et al. results, HEG case



(a) Vibrational temperature, Maier et al. results, HEG case (b) Vibrational temperature, HEG case

Figure 6.12: Vibrational temperature, Thermal Non-Equilibrium gas, comparison with Maier et al. results, HEG case

The shape of the sock is correctly calculated by the simulation, as can be seen

in the figures 6.11 and 6.12. In picture 6.11, the temperature trend is shown and some differences can be seen. In particular, near the stagnation line. There is a lower temperature which then tends to increase locally at 10° . This also affects the heat flux which peaks at this point, figure 6.13. This is also evident in picture 6.12, where the vibrational temperature is reported. Its trend is very different from the numerical trend of Maier et al. [14]. Near the surface of the cylinder, the vibrational temperature is higher, and the peak is shifted further downstream. This is due to the slower vibrational relaxation time in STAR-CCM+. This has already been shown in the N2 bath.

Heat Flux

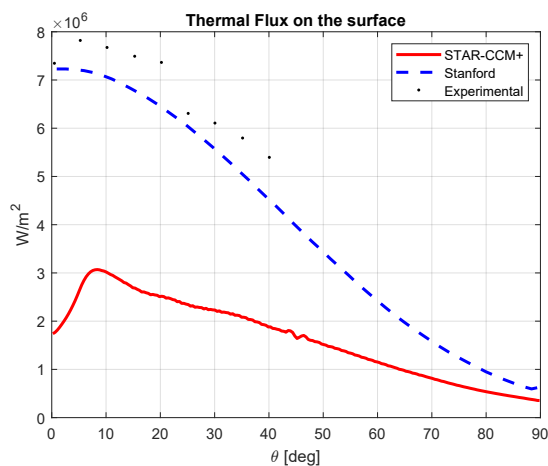


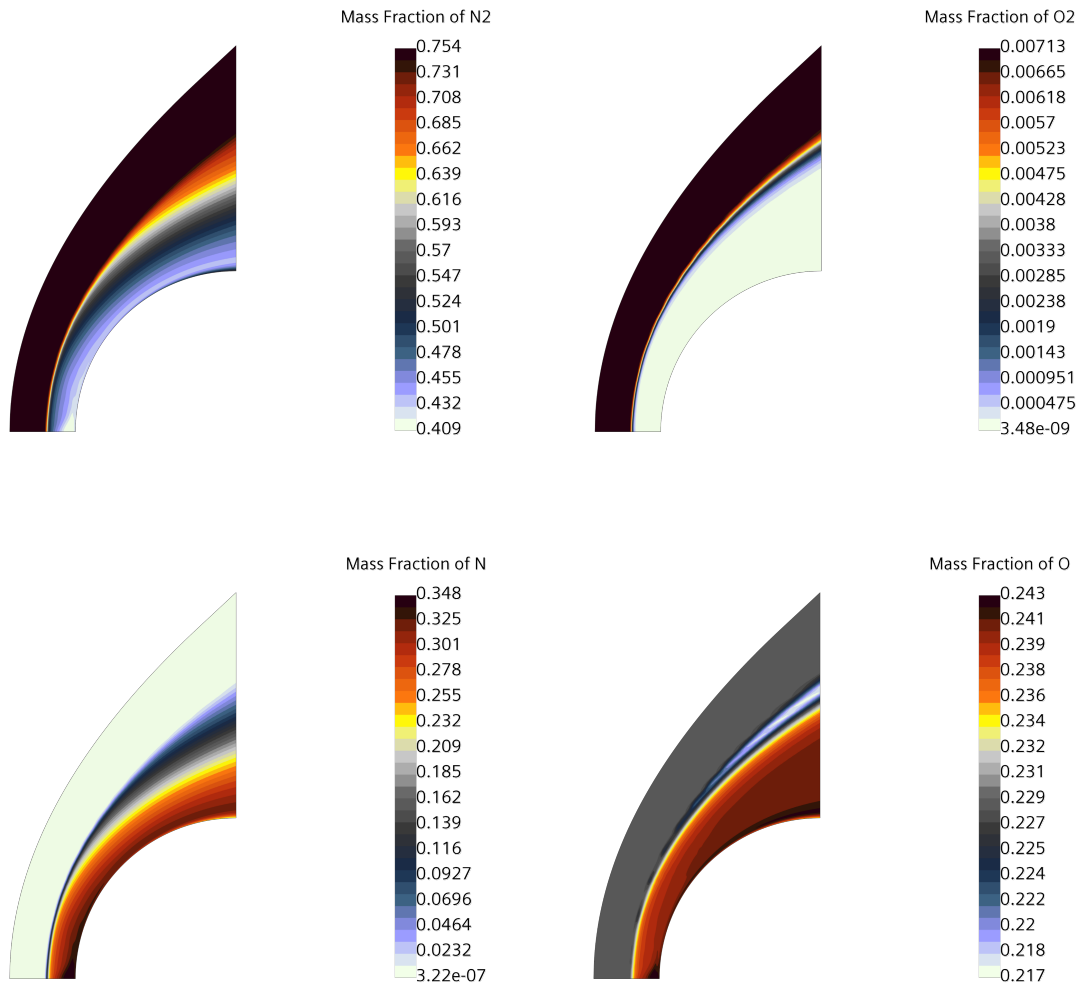
Figure 6.13: Heat Flux, HEG case. Comparison with numerical and experimental results [14]

The calculated heat flux, figure 6.13, is strongly underestimated. The trend is also not in line with the experimental and numerical trend. At least the order of magnitude is correct.

Finally, images of the mass fractions of the different species are shown, figures 6.14. Through the shock N_2 and O_2 dissociate, leading to the formation of the other chemical species. In the upper part of the cylinder, just after the shock, a peak of NO can be seen, formed by the exchange reactions. Beyond this region NO dissociates.

6.6 Comments and considerations

Differences between CFD simulations, numerical and experimental results are evident when considering vibrational temperature. In the inviscid cases, a temperature



relaxation slower than expected is observed. The simple ideal gas model, multi-component and reactant, seems to give more accurate results than the thermal non-equilibrium. There may be several reasons for this. The first is that the comparison has been made in a viscous case. It has not yet been investigated how the transport and diffusion of the species by the software is carried out. In addition, the differences found may be due to incorrect calculation of the reaction rates. The reaction control temperature T_R for dissociation reactions also depends on the vibration temperature of the dissociating species. From the manuals, it does not appear that the software adopts this measure but simply uses the rotational temperature.

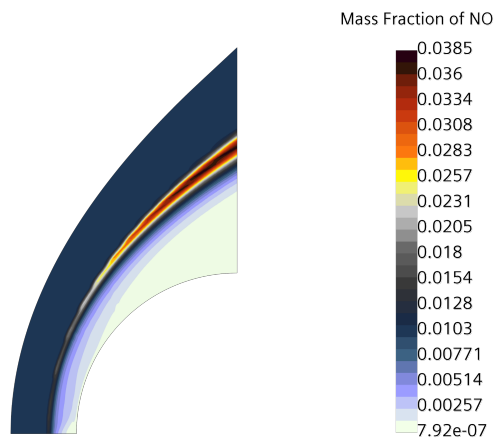


Figure 6.14: Mass fraction of the chemical species, Thermal Non-Equilibrium gas, HEG case

Chapter 7

Conclusion and Further Development

Nearly all the aims of this thesis have been fulfilled. The functionality of the code in MATLAB has been extended and the results obtained have been carefully verified. Knowledge of how STAR-CCM+ deals with thermochemistry, especially chemical and energy equilibrium and non-equilibrium, has been consolidated. However, some questions persist. The main issue is probably electronic energy. This contribution has always been neglected in MATLAB code. On the other hand, in STAR-CCM+, it is modelled but it is not easy to monitor and study its evolution over time. The implementation of electronic energy in MATLAB is one of the possible and natural future developments. This improvement is necessary if the interest is in studying motion fields with extremely high Mach numbers. In addition to this, more precise models can be used, even if they are more expensive to implement. For example, Coupling Vibration Dissociation Vibration (CVDV). This model permits a better calculation of relaxation. Sometimes, in the shown results, an overshoot of the vibrational temperature on the roto-translational temperature occurs. In such cases the result is deeply influenced by the thermochemical model used. It should be remembered that any subsequent improvements to the model must be significant and relevant from an engineering point of view.

On STAR-CCM+, a number of preliminary steps must be taken before starting with more complex simulations. First of all, a sensitivity analysis must be carried out for each problem. This operation must be conducted on the mesh, to identify the most suitable sort and avoid carbuncle numerical instability. In addition, it would be fascinating to evaluate how small variations in the initial values influence the results. The simulated flight conditions are inevitably affected by uncertainties. In conclusion, it should be noted that all the analyses carried out in this study are inviscid. Viscosity and transport by diffusion have not been considered. Any future study aimed, for example, at determining the radar trace of a hypersonic missile,

can not ignore this aspect.

Appendix A

Thermodynamic Properties

A.1 Chemical reactions data

CHEMKIN file has been used to import data about chemical reactions. CHEMKIN files have a rigorous structure:

ELEMENTS: list of all the elements which form the species

SPECIES: list of all the chemical species in the model

REACTIONS: list of all the chemical reaction with the respective rate parameters.

Every reaction has a different line. Every reaction has a different forward rate constant that is calculated by the Arrhenius equation:

$$k_f = AT^\beta e^{-\frac{E_a}{\mathcal{R}T}} \quad (\text{A.1.1})$$

STAR CCM+ computes the reverse backward rate coefficient, k_f , using the equilibrium constant. In every line there are:

- Balanced chemical equation
- Pre-exponent A . The unit of measure is $cm^3s^{-1}mol^{-1}$.
- Temperature exponent β .
- Activation energy E_a . The unit of E_a is specified in the top line of Reactions block ($J/KMOL$). The activation energy is computed from the activation temperature T_a : $E_a = \mathcal{R}T_a$. All data are provided by Park et al. [25].

```

ELEMENTS
N O E
END
SPECIES
N2 O2 NO N O NO+ N+ N2+ O2+ O+ E
END
REACTIONS J/KMOL
O2 + 1N = 2O + 1N 1.000000e+22 -1.500000 4.935190e+08
1O + 1O2 = 3O 1.000000e+22 -1.500000 4.935190e+08
1O2 + 1N2 = 2O + 1N2 2.000000e+21 -1.500000 4.935190e+08
2O2 = 2O + 1O2 2.000000e+21 -1.500000 4.935190e+08
1NO + 1O2 = 2O + 1NO 2.000000e+21 -1.500000 4.935190e+08
1N + 1N2 = 3N 3.000000e+22 -1.600000 9.411448e+08
1O + 1N2 = 1O + 2N 3.000000e+22 -1.600000 9.411448e+08
2N2 = 2N + 1N2 7.000000e+21 -1.600000 9.411448e+08
1O2 + 1N2 = 2N + 1O2 7.000000e+21 -1.600000 9.411448e+08
1NO + 1N2 = 2N + 1NO 7.000000e+21 -1.600000 9.411448e+08
1N + 1NO = 1O + 2N 1.100000e+17 0.000000 6.277070e+08
1O + 1NO = 2O + 1N 1.100000e+17 0.000000 6.277070e+08
1NO + 1N2 = 1O + 1N + 1N2 5.000000e+15 0.000000 6.277070e+08
1NO + 1O2 = 1O + 1N + 1O2 5.000000e+15 0.000000 6.277070e+08
2NO = 1O + 1N + 1NO 1.100000e+17 0.000000 6.277070e+08
1O + 1NO = 1N + 1O2 8.400000e+12 0.000000 1.612916e+08
1O + 1N2 = 1N + 1NO 5.700000e+12 0.420000 3.569865e+08
1E + 1N2 = 1E + 2N 3.000000e+24 -1.600000 9.411448e+08
1E + 1O = 2E + 1O+ 3.900000e+33 -3.780000 1.317769e+09
1E + 1N = 2E + 1N+ 2.500000e+34 -3.820000 1.398415e+09
1O + 1N = 1E + 1NO+ 5.300000e+12 0.000000 2.652166e+08
2N = 1E + 1N2+ 4.400000e+07 1.500000 5.611950e+08
1O+ + 1N2 = 1O+ + 2N 7.000000e+21 -1.600000 9.411448e+08
1N+ + 1N2 = 1N+ + 2N 7.000000e+21 -1.600000 9.411448e+08
1NO+ + 1N2 = 1NO+ + 2N 7.000000e+21 -1.600000 9.411448e+08
1N2+ + 1N2 = 2N + 1N2+ 7.000000e+21 -1.600000 9.411448e+08
1O+ + 1O2 = 1O+ + 2O 2.000000e+21 -1.500000 4.935190e+08
1N+ + 1O2 = 1N+ + 2O 2.000000e+21 -1.500000 4.935190e+08
1NO+ + 1O2 = 1NO+ + 2O 2.000000e+21 -1.500000 4.935190e+08
1N2+ + 1O2 = 2O + 1N2+ 2.000000e+21 -1.500000 4.935190e+08
END

```

Figure A.1: CHEMKIN file, information about reactions

A.2 Thermodynamic data

Thermodynamic data of each chemical species involved are represented with NASA polynomials. STAR CCM+ can manage NASA polynomials with both 7 and 9 coefficients. Furthermore, STAR CCM+ can handle an arbitrary number of temperature ranges. On the opposite, the CHEMKIN format does not support more than two temperature ranges. A macro function has been created to import all the characteristic coefficients of each species. Thermodynamic data for individual species have been taken from [16]. Characteristics of gaseous chemical species for temperatures ranging from 200K to 20 000K are expressed by NASA polynomials:

$$C_p^o(T)/R = a_1T^{-2} + a_2T^{-1} + a_3 + a_4T + a_5T^2 + a_6T^3 + a_7T^4 \quad (\text{A.2.1})$$

$$H^o(T)/RT = -a_1T^{-2} + a_2 \ln T/T + a_3 + a_4T/2 + a_5T^2/3 + a_6T^3/4 + a_7T^4/5 + b_1/T \quad (\text{A.2.2})$$

$$S^o(T)/R = -a_1T^{-2}/2 - a_2T^{-1} + a_3 \ln T + a_4T + a_5T^2/2 + a_6T^3/3 + a_7T^4/4 + b_2 \quad (\text{A.2.3})$$

For each chemical species the equations are defined over three temperature ranges.

T range [K]	a1	a2	a3	a4	a5	a6	a7	b1	b2
E	298.15-1000	0	0	2.5	0	0	0	-745.375	-11.7208122
	1000-6000	0	0	2.5	0	0	0	-745.375	-11.7208122
	6000-20000	0	0	2.5	0	0	0	-745.375	-11.7208122
N	200-1000	0	0	2.5	0	0	0	56104.6378	4.193905036
	1000-6000	88765.0138	-107.12315	2.362188287	0.000291672	-1.72952E-07	-2.67723E-15	56973.5133	4.865231506
	6000-20000	547518105	-310757.498	69.1678274	-0.006847988	3.82757E-07	1.27799E-16	2550585.618	-584.876975
N+	298.15-1000	5237.07921	2.299958315	2.487488821	2.73749E-05	-3.13445E-08	-4.44735E-15	225628.4738	5.0768830786
	1000-6000	290497.0374	-855.790861	3.47738929	-0.000528827	1.35233E-07	5.04617E-16	231080.9984	-1.99414655
	6000-20000	16460921.48	-11131.6522	4.97698664	-0.000200539	1.02248E-08	3.53993E-18	313628.4696	-17.0664638
N2	200-1000	22103.71497	-381.846182	6.08273836	-0.008530914	1.38465E-05	-9.62579E-09	710.846086	-10.76000374
	1000-6000	587712.406	-2239.24907	6.06694922	-0.000613969	1.49181E-07	-1.92311E-11	12832.10415	-15.8664003
	6000-20000	831013916	-642073.354	202.0264635	-0.03065092	2.4869E-06	1.43754E-15	4938707.04	-1672.09974
N2+	298.15-1000	-34740.4747	269.6222703	3.16491637	-0.00213224	6.73048E-06	1.62176E-12	179000.4424	6.832974166
	1000-6000	-2845599.002	7058.89303	-2.88488639	0.003068677	-4.36163E-07	5.412E-16	134038.8483	50.90897022
	6000-20000	-371282977	313928.7234	-96.0351805	0.015711933	-1.17507E-06	-5.62189E-16	-2217361.867	843.6270947
NO	200-1000	-11439.16503	153.6467592	3.43146873	-0.002668592	8.4814E-06	-7.68511E-09	9098.21441	6.72872549
	1000-6000	223901.8716	-1289.65162	5.43393603	-0.000365603	9.88097E-08	-1.41608E-11	17503.17656	-8.50166909
	6000-20000	-957530354	591243.448	-138.456683	0.016943394	-1.00735E-06	-3.29511E-16	-4677501.24	1242.081216
NO+	298.15-1000	1398.106635	-159.044694	5.1228954	-0.006394389	1.12392E-05	2.10738E-12	118749.5132	-4.39843381
	1000-6000	606987.69	-2278.39543	6.08032467	-0.000606685	1.432E-07	-1.74799E-11	132270.9615	-15.1988004
	6000-20000	2676400347	-1832948.69	509.924939	-0.071138193	5.31766E-06	-1.96321E-10	14433089.39	-4324.04446
O	200-1000	-7953.6113	160.717787	1.966226438	0.00101367	-1.11042E-06	6.51751E-10	28403.62437	8.40424182
	1000-6000	261902.0262	-729.872203	3.31717727	-0.000428133	1.0361E-07	-9.4383E-12	33924.2806	-0.66795854
	6000-20000	177900426.4	-108232.826	28.10778365	-0.002975232	1.855E-07	7.19172E-17	889094.263	-218.172815
O+	298.15-1000	0	0	2.5	0	0	0	187935.2842	4.39337676
	1000-6000	-216651.3208	666.545615	1.702064364	0.000471499	-1.42713E-07	-2.0166E-11	183719.1966	10.05690382
	6000-20000	-214383538.3	146951.8523	-36.8086454	0.005036165	-3.0878E-07	-1.07416E-16	-961420.896	342.619308
O2	200-1000	-34255.6342	484.700097	1.119010961	0.004293889	-6.8363E-07	-2.02337E-09	1.03904E-12	-3391.45487
	1000-6000	-1037939.022	2344.830282	1.819732036	-0.001267848	-2.18807E-07	2.05372E-11	-16890.10929	17.38716506
	6000-20000	497529430	-286610.687	66.9035225	-0.006169959	3.0164E-07	-7.42142E-12	2293554.027	-553.062161

Table A.1: Coefficients NASA polynomials

Appendix B

Gibbs Free Energy

B.1 Gibbs Free Energy and Concentrations Equilibrium Constant

The following steps are the key steps, taken from Anderson [2], through which the link between G and K_c can be seen:

$$dG = dH - dTS - TdS \quad (\text{B.1.1})$$

Recalling the first law of thermodynamics

$$\delta Q = dH - \mathcal{V}dp \quad (\text{B.1.2})$$

where Q is the heat absorbed or released by the system, \mathcal{V} is the volume. Recalling the second law of thermodynamics

$$dS = \frac{\delta Q}{T} + dS_{irr} \quad (\text{B.1.3})$$

where dS_{irr} is the entropy change caused by irreversibilities which can be caused by chemical non-equilibrium during the process.

$$TdS = dG + TdS + SdT - \mathcal{V}dp + TdS_{irr} \quad (\text{B.1.4})$$

$$dG = -SdT + \mathcal{V}dp - TdS_{irr} \quad (\text{B.1.5})$$

G is a state variable. However, because we are treating a chemical non-equilibrium process here, where the number of particles of species i per mole of mixture N_i is a function of the thermodynamic state and the history of the process:

$$G = G(p, T, N_1, \dots, N_{spe}) \quad (\text{B.1.6})$$

The total differential of equation (B.1.6):

$$dG = \left(\frac{\partial G}{\partial T} \right)_p dT + \left(\frac{\partial G}{\partial p} \right)_T dp + \sum \frac{\partial G}{\partial N_i} dN_i \quad (\text{B.1.7})$$

Comparing equation (B.1.7) and (B.1.5)

$$S = - \left(\frac{\partial G}{\partial T} \right)_p \quad (\text{B.1.8})$$

$$V = - \left(\frac{\partial G}{\partial p} \right)_T \quad (\text{B.1.9})$$

$$- T dS_{irr} = \sum \frac{\partial G}{\partial N_i} dN_i \quad (\text{B.1.10})$$

It is possible to define g'_i : Gibbs free energy of species i per particle:

$$G = \sum N_i g'_i \quad (\text{B.1.11})$$

$$G = N_1 g'_1 + N_2 g'_2 + \dots + N_n g'_n$$

so,

$$\frac{\partial G}{\partial N_i} = g'_i \quad (\text{B.1.12})$$

Substituting (B.1.12) in equation (B.1.10)

$$dS_{irrev} = - \frac{1}{T} \sum_i g'_i dN_i \quad (\text{B.1.13})$$

Letting N_A the Avogadro's number

$$dS_{irrev} = - \frac{1}{T} \sum_i (N_A g'_i) \left(\frac{dN_i}{N_A} \right) \quad (\text{B.1.14})$$

It is possible to define:

$$\begin{array}{ll} N_A g'_i = G_i & \text{Gibbs free energy of species } i \text{ per mole} \\ \frac{dN_i}{N_A} = d\mathcal{N}_i & \text{Change in the number of moles of } i \end{array} \quad \text{Then,}$$

$$dS_{irrev} = - \frac{1}{T} \sum_i G_i d\mathcal{N}_i \quad (\text{B.1.15})$$

If the variation in thermodynamic state happens through an infinite number of local equilibrium states, the process is reversible and $dS_{irr} = 0$. From equation (B.1.15) this implies that at the equilibrium, the following condition must be true:

$$\sum_i G_i d\mathcal{N}_i = 0 \quad (\text{B.1.16})$$

Any change in the number of moles of species i , $d\mathcal{N}_i$, as a result of a specific chemical reaction must be proportional to the stoichiometric mole number ν_i :

$$d\mathcal{N}_1 : d\mathcal{N}_2 : \dots : d\mathcal{N}_j = \nu_1 : \nu_2 \dots \nu_j \quad (\text{B.1.17})$$

The common proportional constant is defined as $d\xi$

$$\frac{d\mathcal{N}_1}{\nu_1} = \frac{d\mathcal{N}_2}{\nu_2} = \dots = \frac{d \cdot \mathcal{N}_j}{\nu_j} = d\xi \quad (\text{B.1.18})$$

or,

$$\begin{aligned} d\mathcal{N}_1 &= \nu_1 d\xi \\ d\mathcal{N}_2 &= \nu_2 d\xi \\ &\vdots \\ d\mathcal{N}_j &= \nu_j d\xi \end{aligned} \quad (\text{B.1.19})$$

ξ can be physically interpreted as the degree of advancement of reaction. Considering a reference condition where $\xi = 0$ and $\mathcal{N}_i = \mathcal{N}_{i,ref}$:

$$\int_{\mathcal{N}_{i,ref}}^{\mathcal{N}_i} d\mathcal{N}_i = \int_0^\xi \nu_i d\xi \quad (\text{B.1.20})$$

$$\mathcal{N}_i - \mathcal{N}_{i,ref} = \nu_i \xi \quad (\text{B.1.21})$$

For any species i it is possible to write:

$$d\mathcal{N}_i = \nu_i d\xi \quad (\text{B.1.22})$$

Substituting equation (B.1.22) into (B.1.16):

$$\sum_i G_i \nu_i d\xi = 0 \quad (\text{B.1.23})$$

$d\xi$ is the same for all species:

$$d\xi \left(\sum_i G_i \nu_i \right) = 0 \quad (\text{B.1.24})$$

$$\sum_i G_i \nu_i = 0 \quad (\text{B.1.25})$$

Equation (B.1.25) is a condition equilibrium. From the definition (4.4.1), for i species

$$G_i = H_i - TS_i \quad (\text{B.1.26})$$

Using the entropy definition (B.1.3):

$$G_i = H_i - T \left[\int_{T_{\text{ref}}}^T C_{p_i} \frac{dT}{T} - \mathcal{R} \ell_n \frac{p_i}{p_{\text{ref}}} + S_{i, \text{ref}} \right] \quad (\text{B.1.27})$$

Assume that $p_i = 101325 \text{ Pa}$ (1 atm), and $G_i^{p_i=1}$ value of G_i at $p_i = 1 \text{ atm}$:

$$G_i^{p_i=1} = H_i - T \left[\int_{T_{\text{ref}}}^T C_{p_i} \frac{dT}{T} + \mathcal{R} \ln p_{\text{ref}} + S_{i, \text{ref}} \right] \quad (\text{B.1.28})$$

$$G_i = G_i^{p_i=1} + \mathcal{R}T \ln p_i \quad (\text{B.1.29})$$

Substituting (B.1.29) in the equilibrium condition (B.1.25)

$$\begin{aligned} \sum_i v_i G_i &= \sum_i v_i (G_i^{p_i=1} + \mathcal{R}T \ln p_i) = 0 \\ \sum_i v_i G_i^{p_i=1} + \mathcal{R}T \sum_i v_i \ln p_i &= \sum_i v_i G_i^{p_i=1} + \mathcal{R}T \sum_i \ln p_i^{v_i} = 0 \end{aligned} \quad (\text{B.1.30})$$

$$\sum_i \ell_n p_i^{v_i} = - \sum_i v_i \frac{G_i^{p_i=1}}{\mathcal{R}T} \quad (\text{B.1.31})$$

$$\prod_i p_i^{v_i} = \exp \left(- \sum_i v_i \frac{G_i^{p_i=1}}{\mathcal{R}T} \right) \quad (\text{B.1.32})$$

$v_i < 0$ for the reactants and $v_i > 0$ for the products. $G_i^{p_i=1}$ is the difference between the Gibbs free energy of the product and the reactants for a specific chemical reaction, with all species at 1 atm. This difference is written as:

$$\Delta G^{p=1} \equiv \sum_i v_i G_i^{p_i=1} = (G^{p=1} \text{ for products}) - (G^{p=1} \text{ for reactants}) \quad (\text{B.1.33})$$

Using the definition (B.1.33) and substituting in (B.1.32):

$$\prod_i p_i^{v_i} = e^{-\Delta G^{p=1}/\mathcal{R}T} \quad (\text{B.1.34})$$

At the end, from definition:

$$e^{\frac{-\Delta G^{p=1}}{\mathcal{R}T}} = K_p(T) \quad (\text{B.1.35})$$

It is possible to compute K_c from (2.7.12)

$$K_c = \frac{K_p(T)}{\mathcal{R}T} \quad (\text{B.1.36})$$

Appendix C

Solver Settings

High-speed flows are characterized by strong shock waves and shear layers and it is therefore necessary to choose the best numerical methods to be used.

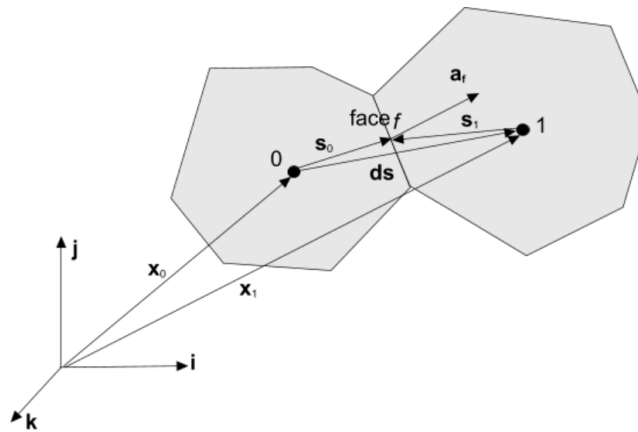


Figure C.1: Example of a 2D finite volume discretization

C.1 Finite Volume Discretization

The finite-volume is a numerical method that allows obtaining a system of algebraic equations derived from a mathematical model. In fluid dynamic, the transformation involves discretizing the governing equations both in space and time. In unsteady cases, the physical time to be analyzed is split into smaller intervals called time-steps. The generalized form of the governing equation in integral form is

$$\frac{d}{dt} \int_V \rho \phi \, dV + \int_S \rho \mathbf{v} \cdot \mathbf{n} \, dS = \int_S \Gamma \nabla \phi \cdot \mathbf{n} \, dS + \int_V S_\phi \, dV \quad (\text{C.1.1})$$

where ϕ is the general scalar, S is the surface of the control volume. There are four different terms:

- time rate of change of ϕ inside the control volume
- convective flux, which expresses the net rate of variation of ϕ across the control volume surface due to convection.
- diffusive flux, which corresponds to the net rate of variation of ϕ across the control volume surface due to diffusion
- source term, which expresses the creation/destruction of fluid property ϕ inside the control volume. The physical nature and modelization of the source term has been extensively discussed in 2.7

It is possible to notice that the equation (2.8.14) presents the same form and terms of the generalised equation.

The integration over the volume is approximated by the product of the mean value of the source term at the centre of the cell and its volume. This approximation is second-order accurate.

The surface integrals are evaluated in terms of variable values at one location on the cell face. The integral is evaluated as the product between the value at the cell face centre and the cell face area:

$$\int_S \mathbf{J}_\phi \cdot \mathbf{n} dS \approx \sum_f J_{\phi,f} S_f \quad (\text{C.1.2})$$

where J_ϕ can be the convective or the diffusive flux of ϕ . However, the values at the cell face centre remain unknown. They can be interpolated with different schemes.

C.1.1 MUSCL 3rd-order scheme

MUSCL (*Monotonic Upstream-centered Scheme for Conservation Laws*) is a finite volume method originally presented by van Leer. It is used to compute the convective term at a face. It provides third-order spatial accuracy, except in the proximity of strong shocks where the spatial accuracy is reduced to second-order, due to limit instability. The convective term at a face can be rearranged as $(\rho \mathbf{v} \cdot \mathbf{n} S)_f = \dot{m}_f \phi_f$, where \dot{m}_f is the mass flow rate at the face f . In each cell the reconstruction is no longer constant and it is obtained from the previous time step.

Normalized-Variable Diagram The scheme adopted a Normalized-Variable Diagram (NVD) value to guarantee the boundedness of the scheme by switching to a lower order of accuracy near shocks or strong gradients. In figure $\alpha_D, \alpha_C, \alpha_U$,

are the downwind, central, and upwind nodal values, while α_f is the value on the face of the cell. The variable ξ is introduced:

$$\xi(f, t) = \xi_f = \frac{\alpha_f - \alpha_U}{\alpha_D - \alpha_U} \quad (\text{C.1.3})$$

α_f can be computed adopting any scheme that uses only nodal values of at points U, C, and D, so $\xi_f = \xi_f(\xi_C)$

Non-physical oscillations in the solution are avoided if α_C is locally bounded:

$$\alpha_U \leq \alpha_C \leq \alpha_D \text{ or } \alpha_D \leq \alpha_C \leq \alpha_U \quad (\text{C.1.4})$$

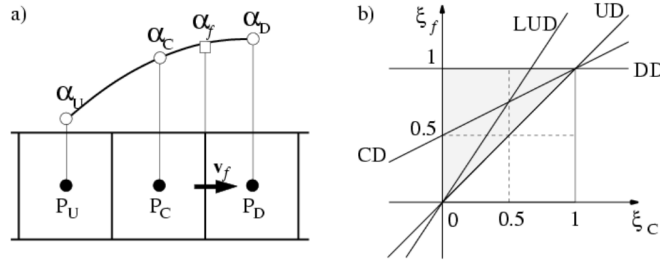


Figure C.2: NVD diagram

In the NVD diagram can be studied the boundedness criterion for convection; figure C.2, it can be expressed with the conditions:

- $0 \leq \xi_C \leq 1$ the region of stability lies between $\xi_f = \xi_C$ and $\xi_f = 1$
- $\xi_C < 0$ and $\xi_C > 1$, the condition is $\xi_f = \xi_C$

It must be highlighted that NVD concerns only convective transport. The importance of the boundedness criteria is vital in the case of variables that have physical bounds; for instance, the mass fraction of a species can not become negative, or larger than unity.

The scheme is adopted for steady and unsteady analysis, and there is one parameter σ_{MUSCL3} , which is used to control the numerical dissipation in the scheme. The convective flux is computed as:

$$(\dot{m}\phi)_f = \begin{cases} \dot{m}\phi_{FOU} & \xi < 0 \text{ or } \xi > 1 \\ \dot{m}(\sigma_{MUSCL3}\phi_{MUSCL3}(1 - \sigma_{MUSCL3})\phi_{CD3}) & 0 \leq \xi \leq 1 \end{cases} \quad (\text{C.1.5})$$

where ϕ_{FOU} is the cell-face center value obtained through first-order upwind interpolation, and ϕ_{CD3} is the cell-face center value obtained through third-order central-differencing interpolation. The ϕ_{MUSCL3} is limited at high speeds as not reduce the order of accuracy and preventing spurious oscillations. The ϕ_{MUSCL3} accuracy is reduced to second order in the regions next to the strong shocks and gradients. The high-speed limitation uses WENO (Weighted Essentially Non-Oscillatory) principles and it is applied to the quadratic part of the reconstruction.

C.1.2 Diffusive Flux

The diffusive flux is discretised as:

$$D_f = (\Gamma \nabla \phi \cdot \mathbf{ndS})_f \quad (\text{C.1.6})$$

The following expression is used due to obtain a second-order accuracy for $\nabla \phi$; it involves the cell values ϕ_0 and ϕ_1 :

$$\nabla \phi_f = (\phi_1 - \phi_0)\alpha + \overline{\nabla \phi} - (\overline{\nabla \phi} \cdot ds)\alpha \quad (\text{C.1.7})$$

where $\alpha = \frac{\mathbf{ndS}}{\mathbf{ndS}(x_1 - x_0)}$, $ds = x_1 - x_0$, $\overline{\nabla \phi} = \frac{\nabla \phi_0 + \nabla \phi_1}{2}$

The second and third terms in (C.1.7) are the secondary gradient contribution and they are vital for the accuracy of non-orthogonal meshes. Using the diagnostic tool that computes the skewness angle for each cell is possible to assure that a valid mesh is being used. Skewness is defined as the difference between the shape of a cell and the shape of an equilateral cell having the same volume. Cells that are highly skewed can reduce accuracy and destabilize the solution. Optimal quadrilateral meshes have vertex angles close to 90° , and triangular meshes should present angles close to 60° and have all angles below 90° .

C.2 Discretization: AUSM+

AUSM stands for Advection Upstream Splitting Method. Here, the flux is considered as being composed of a convective part and a pressure part. The first is evaluated on the basis of a strong interaction between contiguous cells, whereas, for the second, no interaction occurs. The scheme is simple and in several cases surpasses the Roe's solver. The scheme is robust and converges as fast as the Roe splitting. It is also less sensitive to the numerical instability called *carbuncle phenomenon* that, in some cases, afflicts the numerical capturing of shock waves. Around a blunt body, this type of instability originates inside the computational region, where a normal shock is numerically captured, but only when it is aligned with one family of grid coordinates. The mesh geometry is very significant in the creation of the carbuncle phenomenon, in fact, instabilities are encouraged by very elongated elements in the direction normal to the shock. The carbuncle phenomenon occurs in the upwind methods that solve the Riemann problem. In conclusion, it is strongly recommended that the AUSM+ method is used for any STAR-CCM+ simulations of supersonic or hypersonic flows, [C.3](#).

C.3 Courant-Friedrichs-Lewy (CFL) number

The Courant-Friedrichs-Lewy (CFL) number is usually set to 1.0. A higher value for the CFL number causes the solution to converge faster, but the solution could

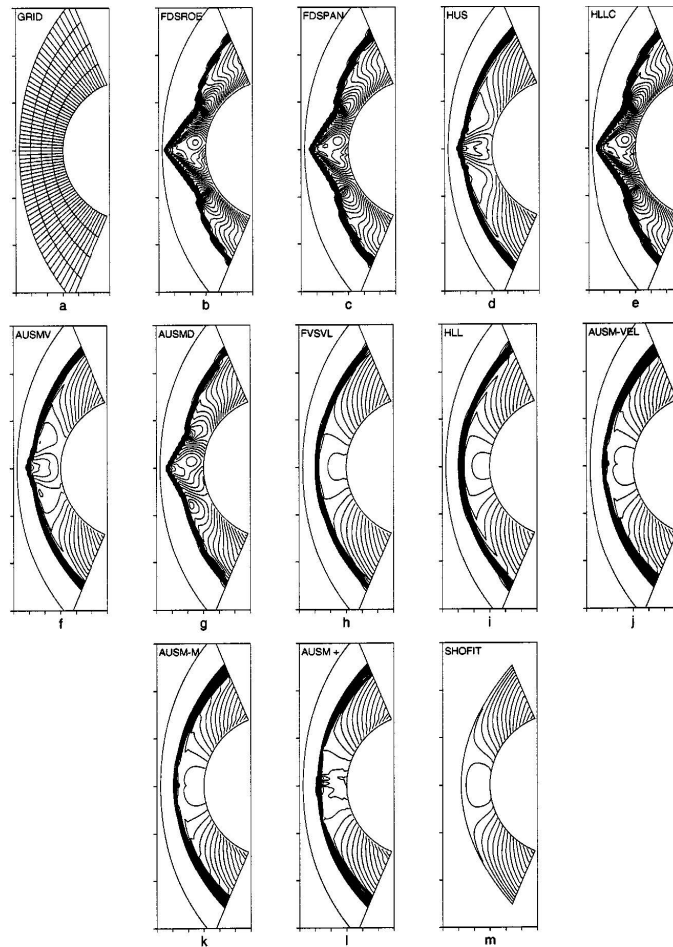


Figure C.3: Carbuncle phenomenon on different solver, [23]

be affected by numerical oscillations that make it unstable. Lower values of the CFL number stabilize the solution but in this case, more iterations are required due to reach convergence. A simulation can fail also with a CFL number of 1.0 or less. In these cases, the cause for the failure is usually associated with some aspect of the problem setup, e.g. mesh quality or a boundary condition.

C.4 Algebraic Multigrid Method

Multigrid methods are algorithms for solving differential equations using a hierarchy of discretizations. Iterative solution algorithms such as Jacobi or Gauss-Seidel converge significantly slower with the increasing of mesh sizes; there is a quadratic relation between time and problem size. Algebraic Multigrid (AMG) method is adopted due to accelerate convergence. This approach has an advantage over other methods, because it scales linearly with the number of nodes used. The number of

operations for solving the problem is proportional to the number of unknowns.

Multigrid methods achieve optimality by adopting two complementary processes that are smoothing and coarse-grid correction:

- Smoothing or relaxation is generally the application of a simple iterative method like Gauss-Seidel or Jacobi. Smoothing eliminates (oscillatory) high-frequency error.
- Coarse-grid correction transfers information from a fine grid to a coarser one through restriction, then solving a coarse-grid system of equations and finally through interpolation, carrying the solution back to the fine grid. It provides a global correction of the fine grid solution approximation, it eliminates low-frequency errors.

After several iterations, a multigrid algorithm transfers the computation from a fine linear system to a coarse linear system. Multigrid algorithms apply the following steps:

- merge cells together to form coarse grid levels
- restriction: transfer the residual from a fine level to a coarser level
- prolongation: move the correction from a coarse level back to a finer level

Simcenter STAR-CCM+ also has two methods for accelerating the convergence: the preconditioned conjugate-gradient method for incompressible flows and the bi-conjugate gradient stabilized method for compressible.

The strategy for moving to coarse levels can have a critical effect on the efficiency of the algorithm. Two cycling strategies are available in the AMG solver used in Simcenter STAR-CCM+. The fixed cycle strategy has been chosen because the problem is stiff and a flexible cycle is not suitable. A complete multigrid cycle is the recursive execution of a single cycle that is composed of the following steps:

1. Pre-smooth
2. Restrict
3. Cycle anew
4. Prolongate
5. Post-smooth

Smooth implies the application of iterative relaxation process to the equations on the current fine level, to compute a new correction. Restrict is to shift the residuals to the next coarsest level where a new cycle is executed. After that, the corrections are transferred back up to the current fine level (prolongated) where smoothing

is applied. There are different types of multigrid methods with many trade-offs between the speed of solving a single iteration and the rate of convergence of a single iteration. In Simcenter STAR-CCM+ there are 3 types: V-Cycle, F-Cycle, and W-Cycle. In a 2D analysis, F-Cycle requires 83% more time to be executed than a V-Cycle iteration and a W-Cycle iteration needs 125% more. In a 3D domain, a F-Cycle iteration and a W-Cycle iteration require about 64% and 75% more time respectively than a V-Cycle iteration. Generally, W-Cycle produces similar convergence to F-Cycle and they are more stable than V-Cycle especially in problems with high Péclet numbers. In particular, the F fixed cycle is adopted as a result of a trade-off between speed and stability.

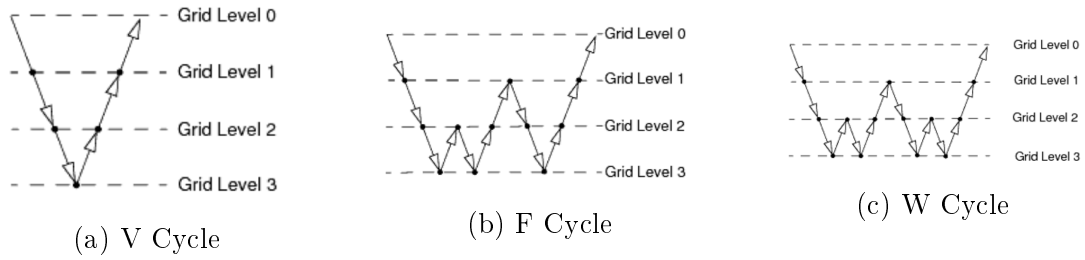


Figure C.4: Cycle strategies available in STAR CCM+

C.4.1 AMG solver

The linear system $Ax = b$ can be iteratively solved using the Jacobi or Gauss-Seidel method. At each step k the approximate solution x_k is better than the previous one x_{k-1} . The matrix A is split in 3 matrix:

$$A = E + D + F \tag{C.4.1}$$

where E is the part below the diagonal, D is the diagonal and F is the part above the diagonal. Then $M = D$, $N = E + F$, so $A = M + N$.

$$\begin{aligned} Ax &= b \\ (M + N)x &= b \\ Mx &= b - Nx \\ Mx_k &= b - Nx_{k-1} \end{aligned} \tag{C.4.2}$$

It is easy to obtain x_k from the expression (C.4.2), in fact M is a diagonal matrix and the inversion process requires a small effort.

$$x_k = M^{-1}(b - Nx_{k-1}) \tag{C.4.3}$$

$$x_k = Bx_{k-1} + c \tag{C.4.4}$$

Where B is called matrix of interaction. The algorithm continues until the residual is driven to a small value. The residual at the k - *step* is $r_k = b - Ax_k$. These methods need an initial solution to start x_0 that must be provided by the user. Each cell is analysed in sequence, and the value of x_i in each cell is updated using the coefficients of its neighbouring cells. Jacobi uses the values of $x_i, k - 1$, while Gauss-Seidel uses the most update available values resulting in faster convergence.

C.4.2 Acceleration methods

The preconditioned conjugate-gradient (PCG) method can not be used because it is suitable only for incompressible flows and at high Mach the variation of density is remarkable. Nevertheless, for compressible flows, the Bi-Conjugate Gradient Stabilized (BiCGStab) method can be adopted. The algorithm has been developed to improve the robustness and the speed of convergence of the solution.

Bibliography

- [1] Anderson Jhon D. Jr., *Modern compressible flow*, Tata McGraw-Hill Education, 2003
- [2] Anderson Jhon D. Jr., *Hypersonic and High Temperature Gas Dynamics*, American Institute of Aeronautics and Astronautics, 2006
- [3] Ben-Dor G. and Igra O. *The relaxation zone behind normal shock waves in a reacting dusty gas.*, Department of Mechanical Engineering, Ben-Gurion University of the Negev, Beer-Sheva, Israel, 1981
- [4] Brandt Achi *Algebraic multigrid theory: The symmetric case*, Department of Applied Mathematics Weizmann Institute of Science, 1986
- [5] Candler Graham V. and MacCormack Robert W. *Computation of Weakly Ionized Hypersonic Flows in Thermochemical Nonequilibrium*, Journal of Thermophysics, 1991
- [6] Comstock Robert Jin *Hypersonic Heat Transfer Load Analysis in STAR-CCM+*, Faculty of California Polytechnic State University, December 2020
- [7] Cross Peter G. and West Michael R., *Simulation of Hypersonic Flowfields Using STAR-CCM+*, Aeromechanics and Thermal Analysis Branch Weapons Airframe Division, 2019
- [8] Falgout R. D. *An Introduction to Algebraic Multigrid*, Lawrence Livermore National Laboratory, 2006
- [9] Gnoffo Peter A., Gupta Roop N., Shinn Judy L. *Conservation Equations and Physical Models for Hypersonic Air Flows in Thermal and Chemical Nonequilibrium*, NASA, 1989
- [10] Gupta R. N. and Yos J. M. and Thompson R. A. Lee K. *A Review of Reaction Rates and Thermodynamic and Transport Properties for an 11-Species Air Model for Chemical and Thermal Nonequilibrium Calculations to 30000K*, NASA, 1990
- [11] Leibowitz Lewis P. and Kuo Ta-Jin *Ionizational Nonequilibrium Heating During Outer Planetary Entries*, Jet Propulsion Laboratory, Pasadena, 1967
- [12] Lockwood Brian and Mavriplis Dimitri *Gradient-based methods for uncertainty quantification in hypersonic flows*, University of Wyoming, 2012
- [13] Kee R. J. and Rupley F. M. and Miller J. A. *The Chemkin Thermodynamic Data Base*, Computational Mechanics Division Sandia National Laboratories,

March 1990

- [14] Maier Walter T., Needels Jacob T., Garbacz Catarina, Morgado Fábio, Alonso Juan J. and Fossati Marco *SU2-NEMO: An Open-Source Framework for High-Mach Nonequilibrium Multi-Species Flows*, Aerospace 2021,8, 193. <https://doi.org/10.3390/aerospace8070193>
- [15] Mallinger F. *Numerical Analysis of Different Vibrational Relaxation Models for Master Equations*, Institut National De Recherche En Informatique Et En Automatique, Sept 1997
- [16] McBride J. B. and Gordon S. and Martin A. R. *NASA Glenn Coefficient for Calculating Thermodynamical and Transport Properties of Individual Species*, Nasa, 2002
- [17] McBride J. B. and Gordon S. and Martin A. R. *Coefficient for Calculating Thermodynamical and Transport Properties of Individual Species*, Nasa, 1993
- [18] Liou Meng-Sing and Steffen Christopher J. Jr., *A New Flux Splitting Scheme*, Journal Of Computational Physics, May 1991
- [19] Millikan Roger C. and White Donald R. *Systematics of Vibrational Relaxation*, General Electric Research Laboratory, Schenectady, New York, 1963
- [20] Moretti Gino and Abbett Michael, *A Time-Dependent Computational Method for Blunt Body Flows*, AIAA Journal, December 1966
- [21] Moore Charlotte E., *Atomic Energy Levels*, Circular National Bureau of Standards, 1958
- [22] Nerem R. M. and Carlson L. A. and Hartsel J. E. *Chemical Relaxation Phenomena behind Normal Shock Waves in a Dissociated Freestream*, The Ohio State University, Columbus, Ohio, May 1967
- [23] Pandolfi Maurizio and D'Ambrosio Domenic *Numerical Instabilities in Upwind Methods: Analysis and Cures for the "Carbuncle" Phenomenon*, Journal of Computational Physics, 2001
- [24] Park Chul *Convergence of Computation of Chemical Reacting Flows*, NASA Ames Research Center, 1985
- [25] Park Chul and Jaffe Richard L. and Partridge Harry, *Chemical-Kinetic Parameters of Hyperbolic Earth Entry*, in Journal of Thermophysics and Heat Transfer, vol. 15, 2001
- [26] Park Chul *Review of Chemical-Kinetic Problems of Future NASA Missions, I: Earth Entries*, in Journal of Thermophysics and Heat Transfer, vol. 7, 1993
- [27] Pimentel Carlos Alberto Rocha and Hetem Annibal Jr., *Computation of air chemical equilibrium composition until 30000K*, Federal University of Santo André Brazil, 2011
- [28] Sockalingam Subramani and Tabiei Ala *Fluid-thermal-chemical non-equilibrium simulation of hypersonic reentry vehicless*, Department of Aerospace Engineering and Engineering Mechanics University of Cincinnati, Cincinnati, 2009

- [29] Stupochenko Yeo V. and Losev S. A. and Osipov A. I., *Relaxation in Shock Waves*, Springer, 1967
- [30] Sung-Ik Sohn *A New TVD-MUSCL Scheme for Hyperbolic Conservation Laws*, Elsevier Ltd, 2005
- [31] Surzhikov S. T. *Ionization of air in flow around a blunt wedge at relatively low hypersonic speeds*, Journal of Physics: Conference Series, 2018
- [32] Phongthanapanich Sutthisak, *Healing of the Carbuncle Phenomenon for AUS-MDV Scheme on Triangular Grids*, International Journal of Nonlinear Sciences and Numerical Simulation, vol. 17, no. 1, 2016, pp. 15-28
- [33] Treanor Charles E. and Marrone Paul V. *Effect of Dissociation on the Rate of Vibrational Relaxation*, The Physics of Fluid, 1962
- [34] Treanor Charles E. and Marrone Paul V. *Chemical Relaxation with Preferential Dissociation from Excited Vibrational Levels*, The Physics of Fluid, 1963
- [35] Viviani Antonio and Pezzella Giuseppe, *Aerodynamic and Aerothermodynamic Analysis of Space Mission Vehicles*, Springer, 2015
- [36] Wada Yasuhiro and Liou, Meng-Sing, *An accurate and robust flux splitting scheme for shock and contact discontinuities*, Society for Industrial and Applied Mathematics, Vol. 18, No. 3, pp. 633-657, May 1997